DYNAMICS AND CONTROL OF SPACECRAFT RENDEZVOUS BY NONLINEAR MODEL PREDICTIVE CONTROL

PENG LI

A DISSERTATION SUBMITTED TO
THE FACULTY OF GRADUATE STUDIES
IN PARTIAL FULFILLMENT OF THE REQUIREMENTS
FOR THE DEGREE OF

DOCTOR OF PHILOSOPHY

GRADUATE PROGRAM IN
EARTH AND SPACE SCIENCE AND ENGINEERING
YORK UNIVERSITY
TORONTO, ONTARIO
SEPTEMBER 2018

Abstract

This doctoral research investigates the fundamental problems in the dynamics and control of spacecraft rendezvous with a non-cooperative tumbling target. New control schemes based on nonlinear model predictive control method have been developed and validated experimentally by ground-based air-bearing satellite simulators. It is focused on the autonomous rendezvous for a chaser spacecraft to approach the target in the final rendezvous stage. Two challenges have been identified and investigated in this stage: the mathematical modeling of the target's tumbling motion and the constrained control scheme that is solvable in an on-line manner. First, the mathematical description of the tumbling motion of the target spacecraft is proposed for the chaser spacecraft to rendezvous with the target. In the meantime, the practical constraints are formulated to ensure the safety and avoid collision during the final approaching stage. This set of constraints are integrated into the trajectory planning problem as a constrained optimization problem. Second, the nonlinear model predictive control is proposed to generate the feedback control commands by iteratively solving an open-loop discrete-time nonlinear optimal control problem at each sampling instant. The proposed control scheme is

validated both theoretically and experimentally by a custom-built spacecraft simulator floating on a high-accuracy granite table. Computer software for electronic hardware for the spacecraft simulator and for the controller is designed and developed in house. The experimental results demonstrate the effectiveness and advantages of the proposed nonlinear model predictive control scheme in a hardware-in-the-loop environment. Furthermore, a preliminary outlook is given for future extension of the spacecraft simulator with consideration of the robotic arms.

Dedication

To the memory of my grandfather and dad.

Acknowledgements

I would like to extend my sincere appreciation to many people for their supports and encouragements, without which this dissertation would never have been possible.

First of all, I want to express my heartfelt gratitude to my supervisor, Prof. George Z. H. Zhu, for his consistent supports and constructive suggestions throughout the PhD program. His life experience, unremitting efforts and rigorous academic attitude greatly motivate me to take new challenges and explore my potential in and out of the academia.

I am grateful to my supervisory committee for research evaluation, which inspired me to keep improving the quality of my research, Prof. Regina Lee and late Prof. George Vukovich, for many valuable comments and encouragements in the annual meetings of this doctoral research. Thanks to Prof. Dan Zhang to accept the invitation to fill the position left by George Vukovich.

I also would like to give many thanks to my friends and colleagues, Dr. Gangqi Dong, Dr. Latheepan Murugathasan, Gangqiang Li, Udai Bindra,

Junjie Kang, Chonggang Du, Dr. Shi Lyu, Haichao Gui, and many others for companionship, rewarding academic exchanges and many interesting conversations. In particular, I would like to express my great thanks to visiting Prof. Ning Chen who made great contributions to the experiment and shared a lot practical industrial experiences. The time we worked together in the basement around the air-bearing table is a great unforgettable memory.

Finally, my deepest gratitude goes to my families for the unconditional love, understanding and encouragement. Thanks to my grandma and my mother for the everlasting love which is always the warmest support for me to get through the hardship in the past four years. Thanks to my uncles and aunts, brothers and sisters, for the numerous supports while I was far away from home for such a long time. Also, thanks to my girlfriend Wei Hao who firmly believes and supports me all along this way. Without your support I can barely concentrate on the completion of this PhD program.

Thank you everyone for your support during my PhD study, I wish you all the best.

Table of Contents

List of Tables

List of Figures

List of Abbreviations

3D	=	3-Dimensional
ARPO	=	Autonomous Rendezvous and Proximity Operations
CAD	=	Computer Aided Design
CM	=	Center of Mass
CNOC	=	Continuous-Time Nonlinear Optimal Control
CW	=	Clohessy-Wiltshire
DAQ	=	Data Acquisition
DART	=	Demonstration for Autonomous Rendezvous Technology
DNOC	=	Discrete-Time Nonlinear Optimal Control
DoF	=	Degree-of-Freedom
GEO	=	Geostationary Earth Orbit
LEO	=	Low Earth Orbit
LOS	=	Line-of-Sight
LVLH	=	Local-Vertical Local-Horizontal
NOC	=	Nonlinear Optimal Control
NMPC	=	Nonlinear Model Predictive Control

OE	=	Orbital Express
PWPF	=	Pulse-Width-Pulse-Frequency
QP	=	Quadratic Programming
RSO	=	Resident Space Object
RLS	=	Recursive Least Squares
RHS	=	Receding Horizon Strategy
SDRE	=	State Dependent Riccati Equation
SUMO	=	Spacecraft for the Universal Modification of Orbit
TH	=	Tschauner-Hempel
XSS	=	Experimental Satellite System

Chapter 1 INTRODUCTION AND JUSTIFICATION

Summary: In this chapter, we survey the application of autonomous rendezvous with a tumbling target, justify the research activities, define the research objectives, and outline the method of approach. At the end, we outline the layout of this dissertation and provide a full list of publications out of the doctoral study.

1.1 Background

Over the past decades, more and more satellites have been sent into space for a variety of purposes [1]. Proximity operations of on-orbit servicing spacecraft have attracted extensive attentions with rapid development of autonomous navigation and control technologies [2]. For instance, one of the goals of Phoenix [3] program is to develop robotic on-orbit servicing to cooperatively recycle and reuse valuable components from retired and/or non-operational satellites in geostationary earth orbit (GEO). The challenge arises as the servicing satellite approaching the targets which may be non-cooperative and tumbling [4].

In the past years, great amount of efforts has been devoted to the space debris capture and removal [5]. Autonomous rendezvous and proximity operations (ARPO) between a chaser spacecraft and a target have attracted extensive attentions from researchers concerning the autonomous space debris removal and on-orbit servicing [6]. The challenge arises as the chaser is approaching a non-cooperative dysfunctional spacecraft or space debris. These operations, e.g., capture and repair a malfunctioned target, is a key technique in the space exploration [7].

The increasing number of space debris, such as the upper stage of a rocket, poses serious threats to space missions [8]. The Iridium/Cosmos collision has proposed immense potential of collision in the low earth orbit (LEO) [9]. In order to keep the spacecraft population in the LEO at a reasonable level, the debris objects, in the range of 1-8 metric ton, should be removed [10]. Furthermore, the growing population of the existing space debris threatens the safety of sustainable space discovery [11]. To address these threats, autonomous rendezvous and active space debris removal have been viewed as an attractive strategy [12]. In such missions, the chaser spacecraft needs to track the motion of space debris, and then approaches the target.

The development of key technologies in the autonomous rendezvous and proximity operations leads to the implementation of relevant space missions, such as Experimental Satellite Systems-10 (XSS-10) and XSS-11 [13],

Demonstration for Autonomous Rendezvous Technology (DART), Orbital Express (OE) [14] and the Spacecraft for the Universal Modification of Orbits (SUMO) [15]. In particular, a microsatellite is designed in the mission of XSS-11 to autonomously rendezvous with a non-cooperative resident space object (RSO) in low Earth orbit. The closest distance the XSS-11 reached around the target object in space was approximately 500 m. In addition, the technology of on-orbit refueling and reconfiguration of two satellites is validated through the DARPA's OE Advanced Technology Demonstration Program. Several scenarios are performed in this mission in 2007, including inspect, service, repair, component exchange and propellant transfer [16]. These programs clearly demonstrate the need for an effective and on-line control scheme for autonomous rendezvous and close proximity operations, especially for a non-cooperative tumbling spacecraft [17]. The Soyuz-TMA spacecraft is designed by the Russian Federal Space Agency for the purpose of human spaceflight. The spacecraft is designed to serve the International Space Station, and it has more latitude in the height and weight of the crew and improved parachute systems. The first commercially built and operated spacecraft Dragon is developed as a reusable cargo spacecraft by SpaceX, and it is firstly launched into space by the company's Falcon 9 rocket to rendezvous with the international space station in 2010.

Table 1.1 Comparisons of space missions

Mission	Date	Field	Target	Operation autonomy
ETS-7	1997 JAXA	Autonomous rendezvous and docking successfully demonstrated	Cooperative	Autonomous
Soyuz-TMA	2002 Russia	Rendezvous and docking with international space station	Cooperative	Manually-assisted
XSS-11	2005 NASA	Real time rendezvous and close range proximity operations	Non-cooperative	Autonomous
DART	2005 NASA	Failed by collision during proximity operations in a very close range	Cooperative	Autonomous
Orbital Express	2007 NASA	On-orbit fueling and servicing, target capture and autonomous operations	Cooperative	Autonomous
ATV	2007 ESA	Provide on-orbit service to the international space station	Cooperative	Autonomous
OLEV	2012 ESA	Provide on-orbit servicing to the GEO spacecraft and validate target capturing technologies	Cooperative	Autonomous
Tiangong	2013 CASA	Rendezvous and docking with space station demonstrated successfully	Cooperative	Manually-assisted

Mission	Date	Field	Target	Operation autonomy
Phoenix	2016 NASA	Demonstrate the target capture and provide maintenance to the spacecraft in GEO orbit	Non-cooperative	Autonomous

1.2 Justification of Research

Many control methodologies and/or strategies have been devoted to generating optimal approaching trajectories to transfer autonomously from one relative elliptical orbit to another, with the objectives of efficient propellant consumption, shortest approaching time, high control accuracy, robustness or the combinations of above, subject to operational constraints [18]. Among the proposed approaches, Nonlinear Optimal Control (NOC) has been recognized as one of the most attractive methods to deal with the constrained optimization problems since it optimizes a specific cost function while satisfying the nonlinear equity and/or inequity constraints. However, to obtain a feasible solution to the closed-loop NOC in a fast manner is challenging, even for an unconstrained case [24]. Considering the limit computational power, this is also one of the major concerns for the optimized trajectory planning of spacecraft orbiting the earth. Therefore, the reduction of computational complexity becomes a prior concern before the implementation of spacecraft autonomous rendezvous and proximity operations.

Alternatively, Nonlinear Model Predictive Control (NMPC), which is based on receding horizon strategy (RHS) and re-planning of the optimal trajectory in real time by solving the NOC at each sampling instant, has been proved as an effective method [25]. The effectiveness of NMPC in the applications is validated through the numerical simulations, which can be seen in the published papers. Therefore, the application of NMPC in ARPO a topic worth further studying, and the effectiveness of the application is to be determined.

In terms of the practical validation of the algorithm, the ground testbed provides a relatively low-cost experimentation for spacecraft proximity maneuvers [26]. In this research, the goal of the experiment is to apply the NMPC and verify its effectiveness in a hardware-in-the-loop setting. In particular, the attitude control of the simulator around a single axis is a comparative study of the real attitude control for a real spacecraft's three-axis attitude maneuver. The effectiveness of the proposed control schemes would be verified through the attitude maneuver experiment using the ground testbed.

1.2.1 Challenges of Rendezvous with Tumbling Target

The task of autonomous rendezvous and capture a tumbling non-cooperative target by a chaser spacecraft is challenging. The technical challenges can be summarized from the following perspectives:

(i) *Mathematical modeling of autonomous rendezvous with a non-*

cooperative tumbling target. A non-cooperative tumbling target is defined as a target that is not under control and has no communication between the chaser and the target during the rendezvous and capture process. Thus, the target's tumbling motion is supposed be mathematically described to avoid the collision during the rendezvous.

(ii) *Constrained path planning during the rendezvous process.* The practical constraints should be taken into account during the rendezvous and this leads to a constrained path planning problem. In addition, other requirements, such as, minimize the control error and sudden change of the control force that may cause chattering of the spacecraft, the tumbling motion of the target, just to name a few, should be taken into account for a safe and efficient rendezvous process.

(iii) *Real time capability*. The spacecraft rendezvous with a non-cooperative tumbling target is a real time process. Thus, the constrained path planning problem produces a nonlinear optimal control problem subject to a variety of constraints. It is challenging to solve the constrained optimization problem in a real time manner considering the limited computational resource onboard.

(iv) *Inertial parameter identification in post-capturing phase.*

After capturing the unknown target, the inertial moments of the compound spacecraft become unknown. The critical task in the post-capturing phase is to operate the combined spacecraft system using the task spacecraft's attitude control system. It is challenging to conduct a rest-to-rest attitude reorientation, while identifying the unknown inertial parameters of the combined system at the same time.

1.2.2 Limitations of Existing Researches

To date, numerous literatures proposed various approaches to generate the optimized trajectory in autonomous rendezvous and proximity operations. In particular, the previous study is focused on autonomous and rendezvous with a three-axis attitude-stabilized spacecraft [28]. Due to the complexity and particularity, the technique of approaching a tumbling target has aroused increasing interests and received extensive concerns from researchers in recent years, but it is still a topic far from being fully solved, thus require further study [31].

Unlike the works in previous research which primarily focused on applying NMPC to generate approaching trajectory for the chaser spacecraft to track until successful rendezvous with the target, this work considers active attitude control of the chaser spacecraft along the path until capturing the passive target to synchronize the orientation of the two spacecraft. Moreover,

practical constraints on actuators magnitude and LOS are included during the implementation of the NMPC algorithm proposed to guarantee the safety of the two spacecraft.

In terms of the mathematical model to describe the autonomous rendezvous, the Clohessy-Wiltshire (CW) [32] and Tschauner-Hempel (TH) [35] equations assume the target spacecraft to be a mass point. In order to avoid the collision with the flexible appendages, the size and dynamic characteristics of the tumbling target actually cannot be overlooked during the approaching process. In the meantime, stringent operational requirements, such as the thruster magnitude limitations and attitude control in post-capturing phase, should be taken into account to avoid the sudden change of control force that may cause the chattering of trajectory.

In terms of the control schemes proposed for ARPO, although NOC is considered as an attractive control candidate, the constraints involved in the rendezvous process make a big challenge to solve the constrained optimal control problem in an on-line manner. Therefore, it is necessary to develop a closed-loop control strategy by optimizing a specific cost function while satisfying the nonlinear equity and/or inequity constraints.

1.3 Objectives of Proposed Research

To address the challenges and limitations, this research is focused on

the development of control strategy for autonomous rendezvous and capture a non-cooperative tumbling target with the consideration of feasibility and reliability requirements for potential applications in space. Since the kinematic model of approaching a tumbling target is not available, the mathematical modeling of the target's tumbling motion becomes the first challenge encountered. Secondly, the control schemes with a variety of practical constraints have to be developed to solve the constrained optimization problem in a real time manner. Finally, the effectiveness and efficiency of the proposed control strategy have to be validated both theoretically and experimentally. Therefore, the objectives of this research are as follows:

(i) *Mathematical modeling of tumbling target* — Development of mathematical model of the tumbling target for the chaser spacecraft to use for its trajectory planning.

(ii) *Control schemes for autonomous rendezvous* — Development of innovative control schemes that is solvable in the real time manner for the autonomous rendezvous subject to a set of operational constraints.

(iii) *Verification* — Verification of the effectiveness of the proposed control schemes and apply it in the hardware-in-the-loop environment.

1.4 Methodology of Approach

The methodology of approach in this research begins with the rendezvous dynamics, including the TH model and the Line-of-Sight (LOS) model, and the rigid-body attitude model. The PWPF modulator is integrated into the NMPC to convert the continuous control force to the on-off mode. Furthermore, the recursive least squares (RLS) is integrated into the NMPC to form a new scheme to estimate the inertial parameter during the attitude maneuver in the post-capturing phase.

The NMPC has been widely used to solve the constrained optimal control problem, due to its advantage of online generation of a set of feedback control commands by iteratively solving an open-loop NOC problem at each sampling instant. The receding horizon process is repeated by shifting the time one-step forward each time [38].

Considering the practical restrictions in space missions, the control objective inevitably leads to an optimal control problem subject to a variety of constraints. Then the NMPC scheme is developed with considerations of safety and efficiency to address the limitations, such as, LOS constraint and thruster magnitude constraint. Finally, the spacecraft simulator is custom-built on the ground testbed to validate the feasibility and reliability of the proposed methodology. The methodology of approach is provided in the flow chart below.

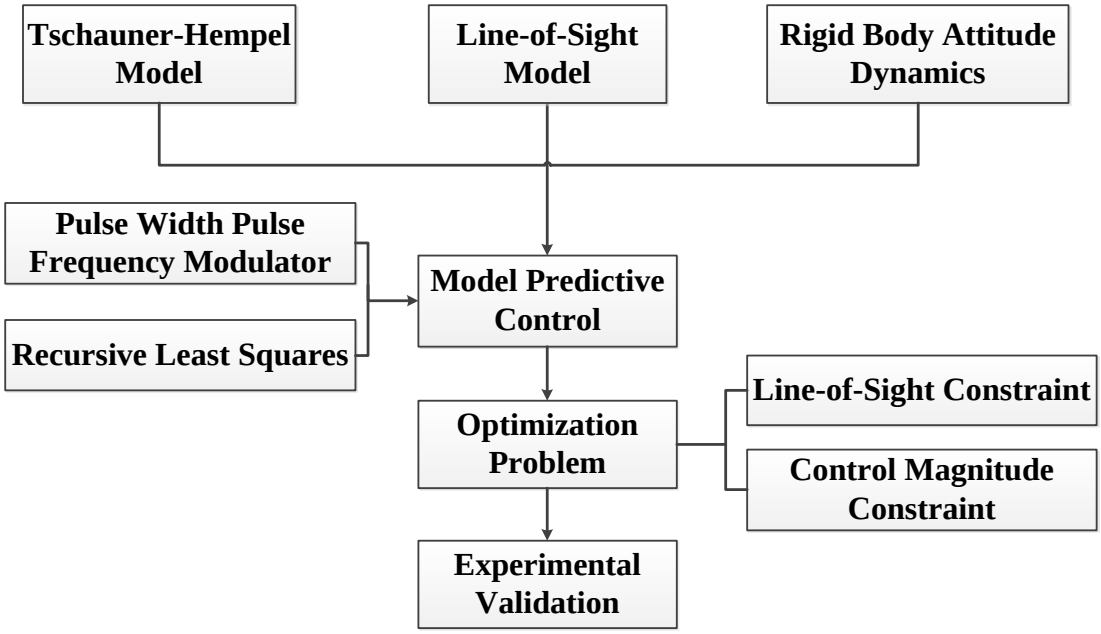

Figure 1.1 Method of Approach

1.5 Outline

The dissertation includes eight chapters. Following the introduction and justification in Chapter 1, a detailed literature review of the autonomous rendezvous and capture a tumbling target is conducted in Chapter 2. Chapter 3 presents the various mathematical formulations developed for autonomous rendezvous and various applied techniques, while Chapter 4 focuses on the nonlinear model predictive control algorithm and its stability analysis. The application studies under various rendezvous scenarios are conducted in Chapter 5 and the hardware and software development of the spacecraft simulator testbed for the validation are described in Chapter 6. To validate the effectiveness of the NMPC in the hardware-in-the-loop environment, the proposed NMPC scheme is applied in the attitude maneuver of the spacecraft

simulator in Chapter 7. Finally, the contributions of this doctoral research are summarized, and the future research directions are outlined in Chapter 8.

1.6 List of Journal Publications

The following is a full list of publications associated with this study.

1. **(Reference Paper A) P. Li** and Z. H. Zhu. "State Dependent Model Predictive Control For Orbital Rendezvous Using Pulse Width Pulse Frequency Modulated Thrusters". ***Advances in Space Research***, Vol. 58, pp. 64-73, 2016.

   doi.org/10.1016/j.asr.2016.04.022

   This paper won the "**Outstanding Paper Award for Young Scientist**" from COSPAR bureau.

2. **(Reference Paper B) P. Li** and Z. H. Zhu. "Line-of-Sight Nonlinear Model Predictive Control for Autonomous Rendezvous in Elliptical Orbit". ***Aerospace Science and Technology***, Vol. 69, pp. 236-243, 2017.

   doi.org/10.1016/j.ast.2017.06.030

3. **(Reference Paper C) P. Li** and Z. H. Zhu. "Model Predictive Control for Spacecraft Rendezvous in Elliptical Orbit". ***Acta Astronautica***, Vol. 146(7), pp. 339-348, 2018.

   doi: 10.1016/j.actaastro.2018.03.025

4. **(Reference Paper D) P. Li** and Z. H. Zhu. "Attitude Control of Compound

Spacecraft with Inertial Parameter Uncertainty in Post-grasping". To be submitted.

Chapter 2 LITERATURE REVIEW

Summary: In this chapter, we review the literature of autonomous rendezvous with a tumbling target and attitude control of compound spacecraft in post-grasping phase. Based on the literature review, the proposed methodology is suggested.

2.1 Spacecraft Rendezvous

In terms of the mathematical model to describe the autonomous rendezvous, the most widely used model with adequate precision is the Clohessy-Wiltshire (CW) equations [32], which was constructed in a Cartesian reference frame centered at the target spacecraft and can be solved analytically. As a linearized model with linear time-invariant (LTI) features, the CW equations are built on the assumptions of nearly circular orbit, small relative distance between the two spacecraft versus the orbit radius and the two body system [33]. As a result, the prediction error increases with the increase of eccentricity [37]. Carter further summarized the various rendezvous models and presented a concise state transition matrix to describe the rendezvous in

a general central force field [33].

2.2 Autonomous Rendezvous with Tumbling Target

Autonomous rendezvous between a chaser spacecraft and a non-cooperative target have attracted extensive attentions from researchers concerning the autonomous active space debris removal and on-orbit servicing [41]. The challenge arises as the servicing satellite approaching the non-cooperative and tumbling target. The relative navigation is a key technique during this process and it is assumed that the sensors can acquire the navigation information for guidance and control subsystems.

The autonomous rendezvous can be divided into four categories by the range between the chaser and target spacecraft, far, medium, close range and super close range which is appropriate to implement the proximity operations. This work focuses on the scenario where the two spacecraft are in the final stage of ARPO. In terms of rendezvous and approaching strategy design, Breger [45] developed an optimization-based model predictive controller for spacecraft formation flying that guarantees collision avoidance for a large class of anomalous system behavior, Matsumoto [47] investigated the problem of planning safe kinematic approach trajectories, and presented a fly-by approach for robotic capture of an uncontrolled rotating satellite. Richards [48] introduced the mixed-integer linear program method for finding fuel-optimal

trajectories subject to constraints of collision avoidance with obstacles or other vehicles and prevention of thruster plumes from one spacecraft impinging on another. Epenoy [49] introduced an exacted penalty function to the solution of inequality state-constrained optimal control problems for ordinary differential equations. Recently, Ping [50] formulated the rendezvous and proximity operations problem as a NOC problem which is then solved by a second-order cone programming method.

In terms of the nonlinear controller design and trajectory optimization in this field, Ma [51] presented an optimal control strategy to rendezvous with a tumbling satellite by applying Pontryagin's maximum principle but the case was restricted to the planar case, without considering path constraint and realistic conditions pertinent to close proximity orbit operations. The problem of coupled position and attitude dynamics together with flexural deformation suppression was formulated as a unified optimal control by Xin [52] using the θ-D nonlinear control technique. However, it is difficult to deal with path constraint and consider magnitude limitation of actuators due to the intrinsic ability of this algorithm. The optimal rendezvous problem with minimum-time and minimum-energy objectives is solved by Boyarko [53] using Gauss pseudospectral method. Unfortunately, a large number of Gauss nodes are needed after transforming the rendezvous into a nonlinear programming problem, thus the solution is difficult to obtain in a relatively short time period.

2.3 Model Predictive Control

Model predictive control is an advanced method of process control to control a process while satisfying the constraints. The associated receding horizon control principle has a history of development back to the late 1960s. It has been in use in the process industries in chemical plants and oil refineries since the 1980s [54]. It has been applied in chemical engineering and power system in recent years. Generalized predictive control (GPC) and dynamic matrix control (DMC) are classical examples of NMPC [57].

Many control methodologies and/or strategies have been devoted to generating optimal approaching trajectories to autonomously transfer from one elliptical orbit to another with various objectives, such as, efficient energy consumption, shortest approaching time, high control accuracy or robustness, subject to operational constraints [58]. Notably, NOC has been recognized as one of the most attractive methods to deal with the constrained optimization problems since it optimizes a specific cost function while satisfying the nonlinear equality and/or inequality constraints [62]. However, to obtain a feasible solution to the closed-loop NOC in a fast manner is challenging, even for an unconstrained case [63].

The attractive characteristics of NMPC make it a candidate for autonomous rendezvous. In particular, limited thruster capacity and sensing

region are typical constraints in rendezvous operations, whilst one of the intrinsic features of NMPC is the ability to handle constraints while considering the control objective [64]. Based on RHS, the NMPC is re-planning the optimal trajectory in real time by solving the NOC at each sampling instant. The resulting NOC problem can be further reduced to a quadratic programming (QP) problem that is computationally affordable for computers onboard spacecraft [65]. In addition, NMPC also features the capacity of inherent reconfiguration and online model parameters modification[57].

Considering the multiple sources of disturbance in space, Gavilan [66] developed standard (non-robust) NMPC into a robust NMPC using chance-constrained approach to cope with additive disturbances expressed by Gaussian probabilistic model and uncertainties caused by unmodeled dynamics. Lately, based on low thrust technique provided by the electric propulsion system, Leomanni [67] studied the spacecraft proximity operations using explicit model predictive control in which the plume impingement is considered. Hartley [68] illustrated how the model predictive control system is designed in the Mars Sample Return mission.

2.4 Pulse-Width-Pulse-Frequency Modulation

Although effective, the control commands from the existing control algorithms are not viable for most cold gas thrusters that work in an on-off

mode with constant magnitude [71]. The continuous control force command should be converted to a sequence of on-off pulses with different durations. Modulating continuous control into equivalent and discrete on-off pulses poses a challenging task for spacecraft designers [72].

Many on-off modulation algorithms have been proposed in the literature, such as, the Schimitt trigger control, the pseudo rate modulator, the integrated pulse frequency modulator and the pulse-width-pulse-frequency (PWPF) modulator [73]. The PWPF modulator is characterized by a first-order lag filter along with a Schimitt trigger inside the negative feedback loop. Compared with others, the PWPF is widely used in spacecraft attitude control system due to its advantages in controlling the on-off switching-states of thrusters in terms of closed-to-linear operation, reduced propellant consumption, high accuracy and adjustability to advanced control algorithms [74]. Up to date, few has attempted to integrate the PWPF modulation with the NMPC in ARPO.

2.5 Post-grasping Attitude Control and Inertial Identification

Over the past decades, space debris removal and on-orbit service by robots has drawn great attentions from researchers [76]. The critical task in these space missions is to capture the unknown non-cooperative debris or spacecraft (the target) with a task spacecraft and then operate the combined spacecraft system [79]. To control the tumbling risk caused by either the

capturing operations or the tumbling motion of the target, the preoccupation is to control the combined spacecraft to a stable attitude state using the task spacecraft's attitude control system [83]. Furthermore, the orientation of the combined spacecraft after capture may not satisfy the requirement of the antennas to point toward the Earth for signal transmission, or fails to meet the need of the solar panel to be perpendicular to sunlight for power generation [87]. Therefore, there is a need for a rest-to-rest attitude maneuver of the combined spacecraft. The high-accuracy reorientation control of the combined spacecraft is challenging due to the inertial redistribution after capturing the unknown target [90]. The object of our work is to conduct a rest-to-rest attitude reorientation, while simultaneously identifying the unknown inertial parameters of the combined system.

Many works have investigated the estimation of inertial parameters of spacecraft. Among them, the recursive least square (RLS) algorithm is one of the popular adaptive estimators for online application due to its fast convergence. Intuitively, the integration of RLS algorithm with NMPC could form an online closed-loop scheme to solve the optimal attitude control of the combined spacecraft effectively.

2.6 Experimental Validation

Experimental validation is a critical step to develop and validate the

relevant techniques in the development of guidance control and navigation strategy for ARPO. In order to emulate the space environment, it is worth noting that the testbed is expected to have similar dynamics characteristics to the real spacecraft in orbit [91].

Bevilacqua [94] introduced the floating spacecraft simulator testbed (FSST) at the Spacecraft Robotics Laboratory. Such an experimental setup is composed of a set of autonomous floating vehicles and a high-accuracy flat surface. This provides a tool for ground testing of guidance, control, and navigation strategies for spacecraft proximity maneuvers. Ciarcià [95] discussed an experimental campaign performed on the FSST that regarded the cooperative docking maneuvers between two vehicles. Scharf [96] described the Jet Propulsion Laboratory's formation control testbed, which comprised two 6-DOF robots on air bearings used to develop and validate formation-flying control architecture and algorithms. Bettanini [97] introduced the free-floater testbed where the floating vehicle was provided an anthropomorphic manipulator with 3-DOF that enabled capture operations.

Chapter 3 MATHEMATICAL FORMULATION

Summary: In this chapter, the classic spacecraft rendezvous models are introduced, and the orbital rendezvous model of a tumbling target is developed accordingly. These rendezvous models are integrated to the nonlinear model predictive control framework to fit the varying needs of various rendezvous scenarios. The effectiveness of these proposed schemes has been validated through numerical simulations and the results have been published in reference A, reference B and reference C.

3.1 Tschauner-Hempel Model

Consider a typical autonomous rendezvous and docking maneuver of a chaser with a target in the Earth's gravitational field. The relative motion is described in an inertial frame $OX_eY_eZ_e$ centered at the Earth as shown. The center of mass (CM) of the target is assumed moving in an elliptic orbit around the Earth, while the chaser is approaching the target. The orbital radii of CM of the target and the chaser are denoted by $\boldsymbol{R}_t$ and $\boldsymbol{R}_c$ in the frame, respectively. The relative motion of the chaser with respect to the target is

described in a LVLH (Local Vertical/Local Horizontal) coordinate system (*o-xyz*) that is centered at the CM of target as shown. The *x*-axis is aligned with $\boldsymbol{R}_t$ pointing outwards, the *z*-axis is aligned with the vector product of $\boldsymbol{R}_t$ and instantaneous orbital velocity of the target, and the *y*-axis completes a right-handed coordinate system.

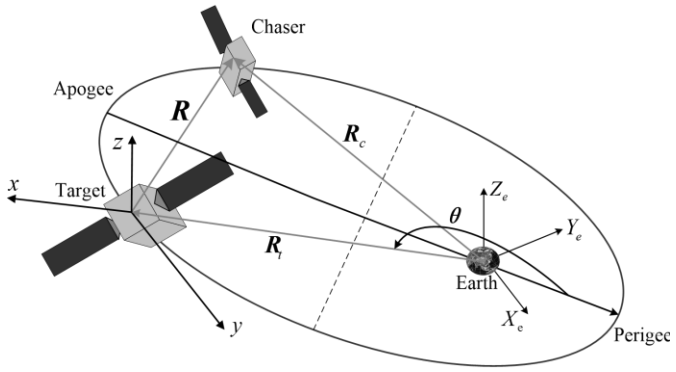

Figure 3.1 Schematic of spacecraft rendezvous and coordinate systems

$$\begin{cases} \dfrac{d^2\boldsymbol{R}_t}{dt^2} = -\dfrac{\mu}{R_t^3}\boldsymbol{R}_t \\ \dfrac{d^2\boldsymbol{R}_c}{dt^2} = -\dfrac{\mu}{R_c^3}\boldsymbol{R}_c + \boldsymbol{f}_c \end{cases} \tag{1.1}$$

where $d(\cdot)/dt$ is the time derivative expressed in the inertial frame, μ is the gravitational constant, $\boldsymbol{f}_c = \left[f_{cx}, f_{cy}, f_{cz} \right]^T$ is the control acceleration acting on the chaser.

The second order time derivative of the relative distance vector, $\boldsymbol{R} = \boldsymbol{R}_c - \boldsymbol{R}_t$, is written as,

$$\frac{d^2\boldsymbol{R}}{dt^2}=\frac{d^2\boldsymbol{R}_c}{dt^2}-\frac{d^2\boldsymbol{R}_t}{dt^2} \tag{1.2}$$

According to the coordinate transformation rules between different coordinate frames, the first and second order time derivatives of the relative distance vector in the orbital frame are written as,

$$\begin{cases}\dfrac{d\boldsymbol{R}}{dt}=\dfrac{\delta\boldsymbol{R}}{\delta t}+\boldsymbol{\omega}\times\boldsymbol{R}\\ \dfrac{d^2\boldsymbol{R}}{dt^2}=\dfrac{\delta^2\boldsymbol{R}}{\delta t^2}+2\boldsymbol{\omega}\times\dfrac{\delta\boldsymbol{R}}{\delta t}+\boldsymbol{\omega}\times\left(\boldsymbol{\omega}\times\boldsymbol{R}\right)+\dot{\boldsymbol{\omega}}\times\boldsymbol{R}\end{cases} \tag{1.3}$$

where $\delta(\cdot)/\delta t$ denotes the time derivative in the orbital frame and $\boldsymbol{\omega}$ is the angular velocity of the target. Rearrange Eq.(1.3) yields,

$$\frac{\delta^2\boldsymbol{R}}{\delta t^2}=-2\boldsymbol{\omega}\times\frac{\delta\boldsymbol{R}}{\delta t}-\boldsymbol{\omega}\times\left(\boldsymbol{\omega}\times\boldsymbol{R}\right)-\dot{\boldsymbol{\omega}}\times\boldsymbol{R}+\mu\left(\frac{\boldsymbol{R}_t}{R_t^3}-\frac{\boldsymbol{R}_c}{R_c^3}\right)+\boldsymbol{f}_c \tag{1.4}$$

In the orbital frame defined by Fig. 3.1, $\boldsymbol{\omega}=\left[0,0,\dot{\theta}\right]^T$, $\boldsymbol{R}_t=\left[R_t,0,0\right]^T$, $\boldsymbol{R}=\left[x,y,z\right]^T$ and $R_c=\sqrt{\left(R_t+x\right)^2+y^2+z^2}$ where θ is the true anomaly. e is the eccentricity of the orbit, a is the semi-major axis, n is the natural frequency of the orbit,

$$\begin{cases} n = \sqrt{\mu / a^3} \\ R_t = \dfrac{a\left(1-e^2\right)}{1+e\cos\theta} \\ \dot{\theta} = \dfrac{n\left(1+e\cos\theta\right)^2}{\left(1-e^2\right)^{3/2}} \\ \ddot{\theta} = \dfrac{-2n^2 e\sin\theta\left(1+e\cos\theta\right)^3}{\left(1-e^2\right)^3} \end{cases} \tag{1.5}$$

Substituting Eq.(1.5) into Eq.(1.4) yields,

$$\begin{cases} \ddot{x} = \dot{\theta}^2 x + \ddot{\theta} y + 2\dot{\theta}\dot{y} + \mu / R_t^2 - \mu\left(R_t + x\right)/R_c^3 + f_{cx} \\ \ddot{y} = -\ddot{\theta} x + \dot{\theta}^2 y - 2\dot{\theta}\dot{x} - \mu y / R_t^3 + f_{cy} \\ \ddot{z} = -\mu z / R_t^3 + f_{cz} \end{cases} \tag{1.6}$$

If the distance between two spacecraft is sufficiently small compared to the orbit radius, i.e., $R \ll R_c$ and $R \ll R_t$. The relative motion can be described by the linearized TH equations in the neighborhood of the target orbiting in an elliptic orbit [36], such that,

$$\begin{Bmatrix} \ddot{x} \\ \ddot{y} \\ \ddot{z} \end{Bmatrix} = -2\begin{bmatrix} 0 & -\dot{\theta} & 0 \\ \dot{\theta} & 0 & 0 \\ 0 & 0 & 0 \end{bmatrix}\begin{Bmatrix} \dot{x} \\ \dot{y} \\ \dot{z} \end{Bmatrix} - \begin{bmatrix} -\dot{\theta}^2 & 0 & 0 \\ 0 & -\dot{\theta}^2 & 0 \\ 0 & 0 & 0 \end{bmatrix}\begin{Bmatrix} x \\ y \\ z \end{Bmatrix} - \begin{bmatrix} 0 & -\ddot{\theta} & 0 \\ \ddot{\theta} & 0 & 0 \\ 0 & 0 & 0 \end{bmatrix}\begin{Bmatrix} x \\ y \\ z \end{Bmatrix} + \frac{\mu}{R_t^3}\begin{Bmatrix} 2x \\ -y \\ -z \end{Bmatrix} + \frac{1}{m_c}\begin{Bmatrix} F_x \\ F_y \\ F_z \end{Bmatrix} \tag{1.7}$$

where m_c is the mass of the chaser and $\boldsymbol{F} = \left\{F_x, F_y, F_z\right\}^T$ is the control force acting on the chaser, $\mu / R_t^3 = n^2\left(1+e\cos\theta\right)^3 / \left(1-e^2\right)^3$.

Introduce a state vector as $\boldsymbol{X} = \left\{x, y, z, \dot{x}, \dot{y}, \dot{z}\right\}^T$. The linearized TH

equation in Eq.(1.7) is reduced to the first-order state-space equation as

$$\dot{\boldsymbol{X}}(t) = \boldsymbol{A}(t)\boldsymbol{X}(t) + \boldsymbol{B}\boldsymbol{U}(t) \tag{1.8}$$

where $\boldsymbol{A} \in \Re^{6\times 6}$ is the system matrix and $\boldsymbol{B} \in \Re^{6\times 3}$ is the control input matrix,

$$\boldsymbol{A} = \begin{bmatrix} 0 & 0 & 0 & 1 & 0 & 0 \\ 0 & 0 & 0 & 0 & 1 & 0 \\ 0 & 0 & 0 & 0 & 0 & 1 \\ \dfrac{3+e\cos\theta}{1+e\cos\theta}\dot{\theta}^2 & \ddot{\theta} & 0 & 0 & 2\dot{\theta} & 0 \\ -\ddot{\theta} & \dfrac{e\cos\theta}{1+e\cos\theta}\dot{\theta}^2 & 0 & -2\dot{\theta} & 0 & 0 \\ 0 & 0 & -\dfrac{1}{1+e\cos\theta}\dot{\theta}^2 & 0 & 0 & 0 \end{bmatrix} \quad \boldsymbol{B} = \begin{bmatrix} 0 & 0 & 0 \\ 0 & 0 & 0 \\ 0 & 0 & 0 \\ 1 & 0 & 0 \\ 0 & 1 & 0 \\ 0 & 0 & 1 \end{bmatrix}$$

Equation (1.8) can be discretized using the zero-order hold into the linear time invariant (LTI) model, such as,

$$\boldsymbol{X}_{k+1} = \boldsymbol{A}_k \boldsymbol{X}_k + \boldsymbol{B}_k \boldsymbol{U}_k \tag{1.9}$$

where the subscripts k and (k+1) denote the time instants at t_k and t_{k+1}. It should be noted that the matrices $\boldsymbol{A}_k$ and $\boldsymbol{B}_k$ are constant within each time interval and are updated at the beginning of each time interval.

3.2 Tumbling Target

Assume the target is moving in an elliptic orbit. Its attitude is unstable and spinning around a fixed axis that is perpendicular to the orbital plane at

a constant velocity $\boldsymbol{\omega}_s = \{0, 0, -\omega_0\}$. The docking axis **L**, is normal to the spin axis and spins in the orbital plane. The control objective here is to guide the chaser to match the instantaneous position and velocity of the spinning docking port without collision with the target. Based on the above assumptions, a body fixed and target-centered spinning frame $(o\text{-}xyz)_s$ is introduced to describe the rotation of the docking axis, where oz_s is aligned with the spinning axis in the same direction of $\boldsymbol{\omega}_s$, ox_s is along the docking axis pointing towards to the docking port from the center of the target, and the oy_s completes a right-handed coordinate system. Figure 3.2 shows the docking axis, LVLH and spinning frames, and their geometric relationship. It should be noted that the path constraint, such as the LOS constraint in the case of rendezvous with an attitude stable target, is relaxed to allow more rendezvous window.

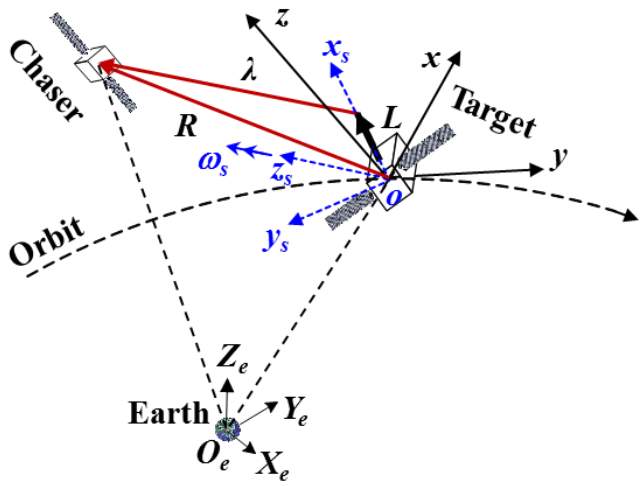

Figure 3.2 Definition of spinning frame

Accordingly, the position vector from the docking port to the CM of the chaser can be defined in the LVLH frame as,

$$\boldsymbol{\lambda}_k = \boldsymbol{R}_k - \boldsymbol{L}_k = \boldsymbol{R}_k - \boldsymbol{C}_{s\_k}^{LVLH}\boldsymbol{L}_s \tag{1.10}$$

where the subscript k refers the time instant, $\boldsymbol{\lambda}_k = \{\lambda_x, \lambda_y, \lambda_z\}_k^T$, $\boldsymbol{L}_k = \{L_x, L_y, 0\}_k^T$, $\boldsymbol{L}_s = \{l, 0, 0\}^T$ is the position vector of the docking port in the spinning frame, and $\boldsymbol{C}_{s\_k}^{LVLH}$ is the transformation matrix from the spinning frame to the LVLH frame, such that,

$$\boldsymbol{C}_{s\_k}^{LVLH} = \begin{bmatrix} \cos(\psi - \omega_0 t_k) & \sin(\psi - \omega_0 t_k) & 0 \\ \sin(\psi - \omega_0 t_k) & -\cos(\psi - \omega_0 t_k) & 0 \\ 0 & 0 & -1 \end{bmatrix}$$

where ψ is the angle between x-axis and x_s-axis initially.

Augmenting the state and control vectors as $\underline{\boldsymbol{X}}_k = \{\boldsymbol{X}_k^T, \boldsymbol{L}_k^T\}^T$ and combining Eq.(1.9) and Eq.(1.10) yield the complete discrete state-space model of the chaser as,

$$\underline{\boldsymbol{X}}_{k+1} = \underline{\boldsymbol{A}}_k \underline{\boldsymbol{X}}_k + \underline{\boldsymbol{B}}_k \underline{\boldsymbol{U}}_k \tag{1.11}$$

where $\underline{\boldsymbol{A}}_k = \boldsymbol{A}_k \oplus \boldsymbol{C}_{s\_k}^{LVLH} \in \Re^{9\times 9}$, $\underline{\boldsymbol{B}}_k = [\boldsymbol{B}_k; \boldsymbol{0}_{3\times 3}] \in \Re^{9\times 3}$ and $\underline{\boldsymbol{U}}_k = \boldsymbol{U}_k$, and $\oplus$ is the notation of direct sum.

3.3 Line-of-Sight Formulation

Consider a chaser approaching a target in the orbital plane of an elliptical orbit. The orbital frame, shown as $O-xyz$ in Fig. 3.3, is defined with its origin at the CM of the target, where the y-axis is along the orbital radius of the target, the x-axis lies in orbital plane and is perpendicular to the y-axis, and the z-axis is normal to the orbital plane to complete a right-hand system. The LOS frame is formed by the range ρ and azimuth angle θ with its origin at the CM of the target, where the azimuth angle θ is measured from the x-axis in the orbital plane as shown in the figure below.

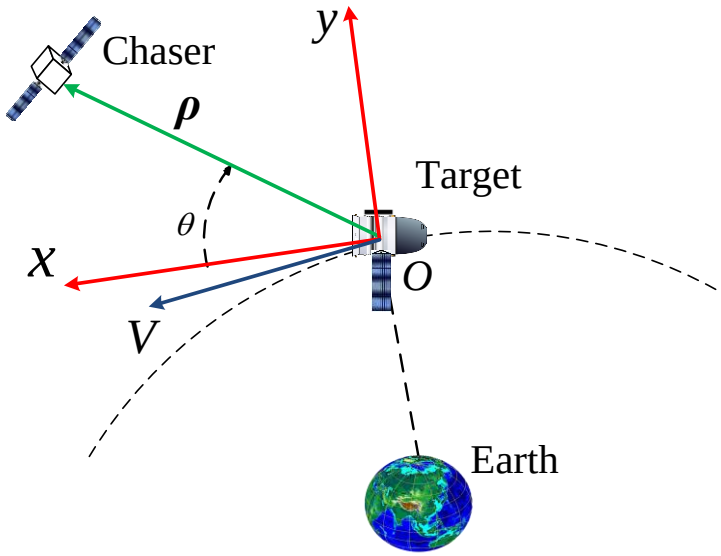

Figure 3.3 Schematic of the LOS frame

As shown above, the second derivatives of the relative distance vector are expressed in the orbital frame as [98],

$$\frac{\delta^2 \boldsymbol{R}}{\delta t^2} = -2\boldsymbol{\omega} \times \frac{\delta \boldsymbol{R}}{\delta t} - \boldsymbol{\omega} \times (\boldsymbol{\omega} \times \boldsymbol{R}) - \dot{\boldsymbol{\omega}} \times \boldsymbol{R} + \mu \left(\frac{\boldsymbol{R}_t}{R_t^3} - \frac{\boldsymbol{R}_c}{R_c^3} \right) + \boldsymbol{f}_c \tag{1.12}$$

Based on the definition of orbital frame as shown in Fig. 3.3, the vectors are explicitly expressed as,

$$\begin{cases} \boldsymbol{R} = \begin{bmatrix} x & y & z \end{bmatrix}^T \\ \boldsymbol{\omega} = \begin{bmatrix} 0 & 0 & -\dot{\theta} \end{bmatrix}^T \\ \boldsymbol{R}_t = \begin{bmatrix} 0 & R_t & 0 \end{bmatrix}^T, \quad \boldsymbol{R}_c = \begin{bmatrix} x & R_t + y & z \end{bmatrix}^T \end{cases} \tag{1.13}$$

Insert Eq.(1.13) into Eq.(1.12), the relative motion model is written as,

$$\begin{Bmatrix} \ddot{x} \\ \ddot{y} \\ \ddot{z} \end{Bmatrix} = \begin{bmatrix} 0 & -2\omega & 0 \\ 2\omega & 0 & 0 \\ 0 & 0 & 0 \end{bmatrix} \begin{Bmatrix} \dot{x} \\ \dot{y} \\ \dot{z} \end{Bmatrix} + \begin{bmatrix} \omega^2 & -\dot{\omega} & 0 \\ \dot{\omega} & \omega^2 & 0 \\ 0 & 0 & 0 \end{bmatrix} \begin{Bmatrix} x \\ y \\ z \end{Bmatrix} + \frac{\mu}{R_t^3} \left(\begin{Bmatrix} 0 \\ R_t \left(1 - \frac{R_t^3}{R_c^3} \right) \\ 0 \end{Bmatrix} - \frac{R_t^3}{R_c^3} \begin{Bmatrix} x \\ y \\ z \end{Bmatrix} \right) + \begin{Bmatrix} f_{cx} \\ f_{cy} \\ f_{cz} \end{Bmatrix} \tag{1.14}$$

where $R_c = \sqrt{x^2 + (R_t + y)^2 + z^2}$. Equation (1.14) can be further expressed as,

$$\begin{cases} \ddot{x} = -2\omega\dot{y} - \dot{\omega}y + \omega^2 x - \dfrac{\mu}{\left[x^2 + z^2 + (R_t + y)^2 \right]^{3/2}} x + f_{cx} \\ \ddot{y} = 2\omega\dot{x} + \dot{\omega}x + \omega^2 y + \dfrac{\mu}{R_t^2} - \dfrac{\mu(R_t + y)}{\left[x^2 + z^2 + (R_t + y)^2 \right]^{3/2}} + f_{cy} \\ \ddot{z} = -\dfrac{\mu}{\left[x^2 + z^2 + (R_t + y)^2 \right]^{3/2}} z + f_{cz} \end{cases} \tag{1.15}$$

Considering the fact that $\rho = \|\boldsymbol{R}\|$, $\rho \ll R_c$ and $\rho \ll R_t$, R_t^3 / R_c^3 is approximated as,

$$\frac{R_t^3}{R_c^3}=\frac{R_t^3}{\left[x^2+z^2+\left(R_t+y\right)^2\right]^{3/2}}=\frac{1}{\left[1+\frac{2y}{R_t}+\frac{x^2+y^2+z^2}{R_t^2}\right]^{3/2}}\approx 1+\left(\frac{2y}{R_t}\right)^{-\frac{3}{2}} \tag{1.16}$$

Expanding Eq.(1.16) and overlook the second order terms yields,

$$\frac{R_t^3}{R_c^3}\approx\left(1+\frac{2y}{R_t}\right)^{-\frac{3}{2}}\approx 1-\frac{3}{2}\cdot\frac{2y}{R_t}+\frac{15}{8}\cdot\left(\frac{2y}{R_t}\right)^2+\cdots\approx 1-\frac{3y}{R_t} \tag{1.17}$$

Substituting Eq.(1.17) into Eq.(1.16) yields,

$$\frac{\mu}{R_t^3}\left(\begin{Bmatrix}0\\ R_t\left(1-\frac{R_t^3}{R_c^3}\right)\\ 0\end{Bmatrix}-\frac{R_t^3}{R_c^3}\begin{Bmatrix}x\\ y\\ z\end{Bmatrix}\right)\approx\frac{\mu}{R_t^3}\begin{bmatrix}-x\\ 2y\\ -z\end{bmatrix} \tag{1.18}$$

Then, the relative motion of spacecraft can be described by the linearized TH equation in the orbital frame is written as,

$$\begin{Bmatrix}\ddot{x}\\ \ddot{y}\\ \ddot{z}\end{Bmatrix}=\begin{bmatrix}0 & -2\omega & 0\\ 2\omega & 0 & 0\\ 0 & 0 & 0\end{bmatrix}\begin{Bmatrix}\dot{x}\\ \dot{y}\\ \dot{z}\end{Bmatrix}+\begin{bmatrix}\omega^2 & -\dot{\omega} & 0\\ \dot{\omega} & \omega^2 & 0\\ 0 & 0 & 0\end{bmatrix}\begin{Bmatrix}x\\ y\\ z\end{Bmatrix}+\frac{\mu}{R_t^3}\begin{bmatrix}-x\\ 2y\\ -z\end{bmatrix}+\frac{1}{m_c}\begin{Bmatrix}F_x\\ F_y\\ F_z\end{Bmatrix} \tag{1.19}$$

To focus on the fundamentals of the LOS based NMPC, the current work is limited to the in-plane rendezvous with the target.

$$\begin{Bmatrix}\ddot{x}\\ \ddot{y}\end{Bmatrix}=\begin{bmatrix}0 & -2\omega\\ 2\omega & 0\end{bmatrix}\begin{Bmatrix}\dot{x}\\ \dot{y}\end{Bmatrix}+\begin{bmatrix}\omega^2 & -\dot{\omega}\\ \dot{\omega} & \omega^2\end{bmatrix}\begin{Bmatrix}x\\ y\end{Bmatrix}+\frac{\mu}{R_t^3}\begin{Bmatrix}-x\\ 2y\end{Bmatrix}+\frac{1}{m_c}\begin{Bmatrix}F_x\\ F_y\end{Bmatrix} \tag{1.20}$$

The relationship between the orbital frame and the LOS frame can be expressed as,

$$\begin{Bmatrix} x \\ y \end{Bmatrix} = \begin{bmatrix} \rho\cos\theta \\ \rho\sin\theta \end{bmatrix} \tag{1.21}$$

Accordingly, the first and second order derivatives of the relative states $\{x, y\}^T$ can be expressed in terms of LOS frame, such that,

$$\begin{cases} \dot{x} = \dot{\rho}\cos\theta - \rho\dot{\theta}\sin\theta \\ \dot{y} = \dot{\rho}\sin\theta + \rho\dot{\theta}\cos\theta \end{cases} \tag{1.22}$$

$$\begin{cases} \ddot{x} = \left(\ddot{\rho} - \rho\dot{\theta}^2\right)\cos\theta - \left(\rho\ddot{\theta} + 2\dot{\rho}\dot{\theta}\right)\sin\theta \\ \ddot{y} = \left(\ddot{\rho} - \rho\dot{\theta}^2\right)\sin\theta + \left(\rho\ddot{\theta} + 2\dot{\rho}\dot{\theta}\right)\cos\theta \end{cases} \tag{1.23}$$

Substituting Eq.(1.22) and Eq.(1.23) into Eq. (1.20) yields,

$$\begin{cases} \ddot{\rho} - \rho\left(\dot{\theta} - \omega\right)^2 + \dfrac{\mu}{R_c^3}\rho - \dfrac{\mu}{R_t^3}\left(1 - 3\sin^2\theta\right)\sin\theta = \dfrac{F_\rho}{m_c} \\ \rho\ddot{\theta} + 2\dot{\rho}\left(\dot{\theta} - \omega\right) - \dot{\omega}\rho - \dfrac{\mu}{R_t^2}\left(1 - \dfrac{R_t^3}{R_c^3}\right)\cos\theta = \dfrac{F_\theta}{m_c} \end{cases} \tag{1.24}$$

where $\{F_\rho, F_\theta\}^T$ is the applied force expressed in the LOS frame and can be transformed from the orbital frame as,

$$\begin{Bmatrix} F_\rho \\ F_\theta \end{Bmatrix} = \boldsymbol{A}^{-1}\begin{Bmatrix} F_x \\ F_y \end{Bmatrix}, \text{ and } \boldsymbol{A}^{-1} = \begin{bmatrix} \cos\theta & \sin\theta \\ -\sin\theta & \cos\theta \end{bmatrix}$$

Substituting Eq.(1.17) into Eq.(1.24), the equations of motion of the chaser in the LOS frame is expressed as,

$$\begin{cases} \ddot{\rho} - \rho\dot{\theta}^2 + 2\omega\rho\dot{\theta} + \left[\left(1-3\sin^2\theta\right)\dfrac{\mu}{R_t^3} - \omega^2\right]\rho = \dfrac{F_\rho}{m_c} \\ \rho\ddot{\theta} + 2\dot{\rho}\dot{\theta} - 2\omega\dot{\rho} - \left(\dot{\omega} + 3\dfrac{\mu}{R_t^3}\sin\theta\cos\theta\right)\rho = \dfrac{F_\theta}{m_c} \end{cases} \tag{1.25}$$

where F_ρ and F_θ are the force components in the ρ and θ directions of the LOS frame.

Introduce the new state vector $\boldsymbol{X} = \{x_1, x_2, x_3, x_4\}^T$ with $x_1 = \rho$, $x_2 = \theta$, $x_3 = \dot{\rho}$ and $x_4 = \rho\dot{\theta}$. Then, Eq. (1.25) is reduced to a set of first-order differential equations, such that,

$$\dot{\boldsymbol{X}}(t) = \boldsymbol{A}(\boldsymbol{X})\boldsymbol{X}(t) + \boldsymbol{B}\boldsymbol{U}(t) \tag{1.26}$$

$$\boldsymbol{A}(\boldsymbol{X}) = \begin{bmatrix} 0 & 0 & 1 & 0 \\ 0 & 0 & 0 & \dfrac{1}{x_1} \\ \omega^2 - \dfrac{\mu}{R_t^3}(1-3\sin^2 x_2) & 0 & 0 & \dfrac{x_4}{x_1} - 2\omega \\ \dot{\omega} + 3\dfrac{\mu}{R_t^3}\sin x_2 \cos x_2 & 0 & 2\left(\omega - \dfrac{x_4}{x_1}\right) & 0 \end{bmatrix} \text{ and } \boldsymbol{B} = \begin{bmatrix} 0 & 0 \\ 0 & 0 \\ 1 & 0 \\ 0 & 1 \end{bmatrix}$$

where $\boldsymbol{A}(\boldsymbol{X}) \in \Re^{4\times4}$ and $\boldsymbol{B} \in \Re^{4\times2}$ are the state-dependent system matrix and

control input matrix, respectively, and $\boldsymbol{U} = \left\{F_{x_1}, F_{x_2}\right\}^T / m_c$ is the control input. It should be noted that the state $x_1 = \rho$ will never approach to zero in practice because the target has finite dimensions. Similarly, Eq.(1.26) can be discretized using the zero-order hold into the following form, such as,

$$\boldsymbol{X}_{k+1} = \boldsymbol{A}_k \boldsymbol{X}_k + \boldsymbol{B}_k \boldsymbol{U}_k \tag{1.27}$$

where the subscripts k and (k+1) denote the time instants at t_k and t_{k+1}.

3.4 Rigid-body Attitude Dynamics

Assume a chaser spacecraft captures a non-cooperative target and then moves together in the post-capture phase as a single rigid-body. The attitude of the combined spacecraft is disturbed by the sudden addition of unknown mass of the target. The objective of the current work is to control the attitude of the combined spacecraft to a desired attitude while identifying its unknown inertial parameters. The attitude of the task spacecraft is assumed stationary before the capture. It is required the attitude of the combined spacecraft is stationary again at the end of maneuver, i.e., it is a rest-to-rest attitude maneuver.

Let the attitude of the combined spacecraft be described by Euler angles, $\Theta = \left\{\phi, \theta, \psi\right\}^T$ (roll, pitch and yaw). Spatial rotations in three dimensions can be

parametrized either using Euler angles or unit quaternions. Although the side effect is that Euler angle representation entails the risk of singularity, also called the gimbal lock, when the angle approaches ±90°, the Euler angles are still the most commonly used parameters when picturing a rotation in 3-dimensional space. The rotation along each axis is represented by degree that is conceptually easier to understand, more visual and intuitive. The attitude dynamics of the combined spacecraft can be expressed as [99],

$$\dot{\boldsymbol{\omega}} = \boldsymbol{J}^{-1}\left[\boldsymbol{U} - \boldsymbol{\omega}\times\left(\boldsymbol{J}\boldsymbol{\omega} + \boldsymbol{J}_r\boldsymbol{\omega}_r\right)\right] \text{ and } \boldsymbol{U} = -\boldsymbol{J}_r\dot{\boldsymbol{\omega}}_r \tag{1.28}$$

where $\boldsymbol{\omega} = \dot{\Theta} = \left\{\omega_x, \omega_y, \omega_z\right\}^T$ and $\boldsymbol{J} \in \Re^{3\times3}$ are the angular velocity and true inertial matrix of the combined spacecraft, $\boldsymbol{\omega}_r = \left\{\omega_{rx}, \omega_{ry}, \omega_{rz}\right\}^T$, $\dot{\boldsymbol{\omega}}_r$ and $\boldsymbol{J}_r \in \Re^{3\times3}$ are the angular velocity, angular acceleration and known inertial matrix of reaction wheels of the task spacecraft, $\boldsymbol{U} = \left\{T_x, T_y, T_z\right\}^T$ is the control torque generated by the reaction wheels. Assume $\boldsymbol{L} = \boldsymbol{J}\boldsymbol{\omega}$ is the angular momentum of the combined spacecraft. The control objective is to generate a counter angular momentum $\boldsymbol{L}_r = \boldsymbol{J}_r\boldsymbol{\omega}_r$ by the reaction wheels to maneuver the attitude of the combined spacecraft while keeping the angular momentum of the combined spacecraft remain zero, such that,

$$\boldsymbol{L} + \boldsymbol{L}_r = 0 \tag{1.29}$$

Assume the instantaneous angular velocities of the combined spacecraft are measurable, then the inertial parameters of the combined spacecraft are identifiable by Eq.(1.29), such that, $\boldsymbol{J\omega} = -\boldsymbol{J}_r\boldsymbol{\omega}_r$. For the sake of convenience, recast the true inertial matrix into a vector as $\bar{\boldsymbol{J}} = \left\{J_{xx}, J_{yy}, J_{zz}, J_{xy}, J_{xz}, J_{yz}\right\}^T$. Then, the angular momentum of the combined spacecraft can be written in form of the inertial vector as,

$$\boldsymbol{L} = \boldsymbol{J\omega} = \boldsymbol{H}\bar{\boldsymbol{J}} \quad \text{and} \quad \boldsymbol{H} = \begin{bmatrix} \omega_x & 0 & 0 & \omega_y & \omega_z & 0 \\ 0 & \omega_y & 0 & \omega_x & 0 & \omega_z \\ 0 & 0 & \omega_z & 0 & \omega_x & \omega_y \end{bmatrix} \tag{1.30}$$

where $\boldsymbol{H}$ is the matrix of angular velocity of the combined spacecraft.

Introduce the state vector $\boldsymbol{X} = \left\{\boldsymbol{\Theta}^T, \boldsymbol{\omega}^T\right\}^T = \left\{x_1, x_2, x_3, x_4, x_5, x_6\right\}^T$ with $x_1 = \phi$, $x_2 = \theta$, $x_3 = \psi$, $x_4 = \omega_x$, $x_5 = \omega_y$ and $x_6 = \omega_z$. Then, Eq.(1.28) can be recast into the form in the state space as

$$\dot{\boldsymbol{X}} = \boldsymbol{A}\left(\boldsymbol{X}\right)\boldsymbol{X} + \boldsymbol{BU} \tag{1.31}$$

Here $\boldsymbol{A} \in \Re^{6\times 6}$ is the state-dependent system matrix and $\boldsymbol{B} \in \Re^{6\times 3}$ is the control input matrix, such that,

$$\boldsymbol{A} = \begin{bmatrix} \boldsymbol{0} & \boldsymbol{I} \\ \boldsymbol{0} & -\boldsymbol{J}^{-1}\boldsymbol{\omega} \times \boldsymbol{J} + \boldsymbol{J}_r\boldsymbol{\omega}_r \times \boldsymbol{J}^{-1} \end{bmatrix}, \ \boldsymbol{B} = \begin{bmatrix} \boldsymbol{0} \\ \boldsymbol{J}^{-1} \end{bmatrix}$$

where $\boldsymbol{0}$ and $\boldsymbol{I}$ are 3×3 zero and identity matrices.

Discretizing Eq.(1.31) by the zero-order hold with a sampling interval T_s yields

$$\boldsymbol{X}_{k+1} = \boldsymbol{A}_k \boldsymbol{X}_k + \boldsymbol{B}_k \boldsymbol{U}_k \tag{1.32}$$

where $\boldsymbol{A}_k$, $\boldsymbol{B}_k$ and $\boldsymbol{U}_k$ are the system matrix, control input matrix and the control torque at time instant k, $\boldsymbol{X}_k$ and $\boldsymbol{X}_{k+1}$ are the state variables at time instants k and (k+1), respectively. It should be noted that the discretized matrices $\boldsymbol{A}_k$ and $\boldsymbol{B}_k$ are updated at the beginning of each sampling interval with the states at the end of previous time instant and kept constant within the interval T_s. Furthermore, they contain the unknown inertial parameters to be determined during the attitude maneuver process. The true angular momentum of the combined spacecraft at the time instant k is denoted as $\boldsymbol{L}_k = \boldsymbol{H}_k \bar{\boldsymbol{J}}$, where $\boldsymbol{H}_k$ is the matrix of observed angular velocities of the combined spacecraft or the observation matrix.

3.5 Pulse-Width-Pulse-Frequency Modulation

The error signal $e(t)$ is the difference between the output $\boldsymbol{U}^{PWPF}$ of the Schmitt trigger and the continuous control command $U(t)$. It is fed into the

filter with the gains of K_m and T_m. The output of the filter feeds the Schimitt trigger, where the U_{on} and U_{off} are the Schimitt trigger on/off-values and the U_m is the magnitude of the constant force thruster. $\tilde{\boldsymbol{U}}^{PWPF} = \left[\boldsymbol{U}_1^{PWPF}, \boldsymbol{U}_2^{PWPF}, \boldsymbol{U}_3^{PWPF}\right]^T$ is the vector of the thruster states obtained by PWPF modulators [71]. Figure 3.4 shows the block diagram of the PWPF modulator.

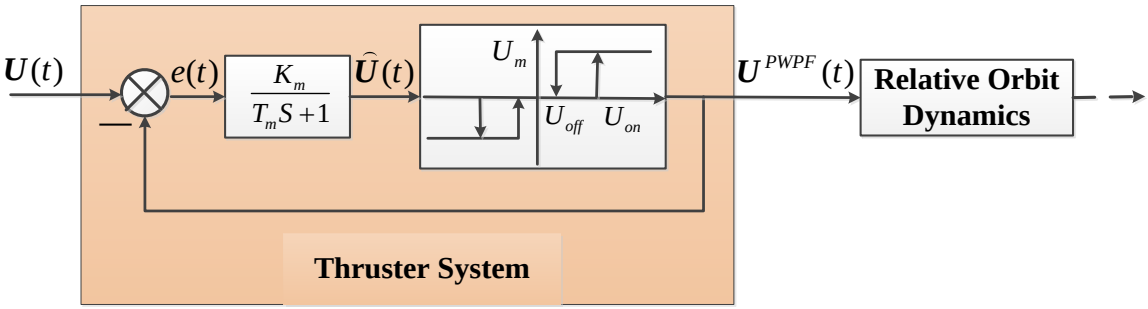

Figure 3.4 Block diagram of PWPF modulator

The switch on and off times of the Schimitt trigger are defined as [74]:

$$T_{on} = -T_m \ln\left\{1 + \frac{U_{on} - U_{off}}{K_m\left[E - U_m\right] - U_{on}}\right\} \tag{1.33}$$

$$T_{off} = -T_m \ln\left\{1 - \frac{U_{on} - U_{off}}{K_m E - U_{off}}\right\} \tag{1.34}$$

The modulating frequency of the PWPF modulator is determined by the switch on and off times

$$f = \frac{1}{T_{on} + T_{off}} \tag{1.35}$$

and the duty cycle is

$$DC = \frac{1+\ln\left(1 + a / x\right)}{\ln\left[1+a/\left(1-x\right)\right]} \tag{1.36}$$

where $E_d = U_{on} / K_m$ is the internal dead-band, $E_s = U_m + U_{off} / K_m$ is the saturation level, $a = \left(U_{on} - U_{off}\right) / \left[K_m \left(E_s - E_d\right)\right]$ is the normalized hysteresis width, and $x = \left(E - E_d\right) / \left(E_s - E_d\right)$ is the normalized input.

3.6 Recursive Least Squares Method

Define the estimated inertial vector as $\hat{\boldsymbol{J}} = \left\{\hat{J}_{xx}, \hat{J}_{yy}, \hat{J}_{zz}, \hat{J}_{xy}, \hat{J}_{xz}, \hat{J}_{yz}\right\}^T$. The objective of the inertial parameter identification is to minimize the weighted error between the true and estimated angular moments of the combined spacecraft during the controlled attitude maneuver, such as,

$$\begin{aligned} \min\ \Pi\left(\hat{\boldsymbol{J}}_k\right) &= \left(\boldsymbol{L}_k - \boldsymbol{H}_k \hat{\boldsymbol{J}}_k\right)^T \boldsymbol{W}_k \left(\boldsymbol{L}_k - \boldsymbol{H}_k \hat{\boldsymbol{J}}_k\right) \\ &= \left(-\boldsymbol{L}_{r,k} - \boldsymbol{H}_k \hat{\boldsymbol{J}}_k\right)^T \boldsymbol{W}_k \left(-\boldsymbol{L}_{r,k} - \boldsymbol{H}_k \hat{\boldsymbol{J}}_k\right) \end{aligned} \tag{1.37}$$

where $\boldsymbol{W}_k$ is the weight matrix at time instant k and $\hat{\boldsymbol{J}}_k$ is the estimated inertial vector at time instant k, such that,

$$\hat{\boldsymbol{J}}_k = -\boldsymbol{P}_k' \bar{\boldsymbol{H}}_k^T \bar{\boldsymbol{W}}_k \boldsymbol{L}_{r,k} \tag{1.38}$$

with $\boldsymbol{P}_k' = \left(\bar{\boldsymbol{H}}_k^T \bar{\boldsymbol{W}}_k \bar{\boldsymbol{H}}_k \right)^{-1}$ being the covariance matrix at time instant *k*.

The augmented weight and observation matrices in Eq.(1.38) are expressed as,

$$\bar{\boldsymbol{W}}_k = \begin{bmatrix} \boldsymbol{W}_1 & 0 & \cdots & 0 \\ 0 & \boldsymbol{W}_2 & \cdots & 0 \\ \vdots & \vdots & \ddots & \vdots \\ 0 & 0 & \cdots & \boldsymbol{W}_k \end{bmatrix}, \quad \bar{\boldsymbol{H}}_k = \begin{bmatrix} \boldsymbol{H}_1 \\ \boldsymbol{H}_2 \\ \vdots \\ \boldsymbol{H}_k \end{bmatrix}_k$$

Then, the estimated inertial vector at time instant (*k*+1) can be expressed as,

$$\begin{aligned} \hat{\boldsymbol{J}}_{k+1} &= \boldsymbol{P}_{k+1}' \begin{bmatrix} \bar{\boldsymbol{H}}_k^T & \boldsymbol{H}_{k+1}^T \end{bmatrix} \begin{bmatrix} \bar{\boldsymbol{W}}_k & 0 \\ 0 & \boldsymbol{W}_{k+1} \end{bmatrix} \begin{bmatrix} -\boldsymbol{L}_{r,k} \\ -\boldsymbol{L}_{r,k+1} \end{bmatrix} \\ &= -\boldsymbol{P}_{k+1}' \bar{\boldsymbol{H}}_k^T \bar{\boldsymbol{W}}_k \boldsymbol{L}_{r,k} - \boldsymbol{P}_{k+1}' \boldsymbol{H}_{k+1}^T \boldsymbol{W}_{k+1} \boldsymbol{L}_{r,k+1} \end{aligned} \tag{1.39}$$

$$\begin{aligned} \boldsymbol{P}_{k+1}' &= \left(\bar{\boldsymbol{H}}_{k+1}^T \bar{\boldsymbol{W}}_{k+1} \bar{\boldsymbol{H}}_{k+1} \right)^{-1} = \left(\begin{bmatrix} \bar{\boldsymbol{H}}_k^T & \boldsymbol{H}_{k+1}^T \end{bmatrix} \begin{bmatrix} \bar{\boldsymbol{W}}_k & 0 \\ 0 & \boldsymbol{W}_{k+1} \end{bmatrix} \begin{bmatrix} \bar{\boldsymbol{H}}_k \\ \boldsymbol{H}_{k+1} \end{bmatrix} \right)^{-1} \\ &= \left(\boldsymbol{P}_k'^{-1} + \boldsymbol{H}_{k+1}^T \boldsymbol{W}_{k+1} \boldsymbol{H}_{k+1} \right)^{-1} \\ &= \boldsymbol{P}_k' - \boldsymbol{P}_k' \boldsymbol{H}_{k+1}^T \left(\boldsymbol{W}_{k+1}^{-1} + \boldsymbol{H}_{k+1} \boldsymbol{P}_k' \boldsymbol{H}_{k+1}^T \right)^{-1} \boldsymbol{H}_{k+1} \boldsymbol{P}_k' \end{aligned} \tag{1.40}$$

From Eq.(1.38), one obtains

$$\boldsymbol{P}_k'^{-1} \hat{\boldsymbol{J}}_k = -\bar{\boldsymbol{H}}_k^T \bar{\boldsymbol{W}}_k \boldsymbol{L}_{r,k} \tag{1.41}$$

From Eq.(1.40), one obtains

$$\boldsymbol{P}_k'^{-1} = \boldsymbol{P}_{k+1}'^{-1} - \boldsymbol{H}_{k+1}^T \boldsymbol{W}_{k+1} \boldsymbol{H}_{k+1} \tag{1.42}$$

Substituting Eq.(1.42) into Eq.(1.41) yields,

$$-\bar{\boldsymbol{H}}_k^T \bar{\boldsymbol{W}}_k \boldsymbol{L}_{r,k} = \left(\boldsymbol{P}_{k+1}'^{-1} - \boldsymbol{H}_{k+1}^T \boldsymbol{W}_{k+1} \boldsymbol{H}_{k+1} \right) \hat{\boldsymbol{J}}_k \tag{1.43}$$

Then, the recursive estimation of inertial vector at time instant (k+1) is given by substituting Eq.(1.43) into Eq.(1.39), such that,

$$\begin{aligned} \hat{\boldsymbol{J}}_{k+1} &= \boldsymbol{P}_{k+1}' \left(\boldsymbol{P}_{k+1}'^{-1} - \boldsymbol{H}_{k+1}^T \boldsymbol{W}_{k+1} \boldsymbol{H}_{k+1} \right) \hat{\boldsymbol{J}}_k - \boldsymbol{P}_{k+1}' \boldsymbol{H}_{k+1}^T \boldsymbol{W}_{k+1} \boldsymbol{L}_{r,k+1} \\ &= \hat{\boldsymbol{J}}_k + \boldsymbol{P}_{k+1}' \boldsymbol{H}_{k+1}^T \boldsymbol{W}_{k+1} \left(-\boldsymbol{L}_{r,k+1} - \boldsymbol{H}_{k+1} \hat{\boldsymbol{J}}_k \right) \end{aligned} \tag{1.44}$$

To initialize the RLS algorithm, the initial values of matrices of $\boldsymbol{W}_0$ and $\boldsymbol{P}_0'$ are provided as follows. First, the weight matrix $\boldsymbol{W}_{k+1}$ is assumed a constant matrix $\boldsymbol{W}$ for simplicity. Next, the initial covariance matrix $\boldsymbol{P}_0'$ is chosen as $\boldsymbol{P}_0' = \alpha \boldsymbol{I}$, where α is a large positive number to ensure fast convergence speed and high estimation accuracy.

Chapter 4 NONLINEAR MODEL PREDICTIVE CONTROL

Summary: The NMPC is characterized with the online generation of a set of feedback control commands by iteratively solving an open-loop discrete-time NOC (DNOC) problem at each sampling instant. The receding horizon process is repeated by shifting the time one-step forward each time. Accordingly, the optimal control problem can be formulated as a series of continuous-time nonlinear optimal control (CNOC) problems by NMPC at each sampling instant. In this chapter, the traditional constrained nonlinear optimal control problem is reformulated as a nonlinear model predictive control problem subject to various constraints, and the stability of the model predictive control is discussed.

4.1 Quadratic Programming Formulation

Denote the starting and ending times of the rendezvous as t_1 and t_f. Divide the total time interval into n subintervals evenly, such that, $[t_1, t_2, \cdots, t_{n+1}]$ where $t_{n+1} = t_f$. Furthermore, assume predictive (T_p) and control

(T_c) horizons are constant with $T_p \geq T_c$. Then, the receding predictive horizon $[t_k,\ t_k + T_p]$ of the kth CNOC problem starts from $t_k \in [t_1, t_{n+1}]$ with the following definition.

Problem Ψ_{CNOC}: At any time instant $t_k \in [t_1, t_{n+1}]$, find the control input rate $\dot{\boldsymbol{U}}(t)$ and states $\boldsymbol{X}(t)$ that minimize the following quadratic cost function over a given predictive horizon T_p,

$$\min J_{t_k} = \int_{t_k}^{t_k+T_p} \left\{\boldsymbol{X}(t) - \boldsymbol{X}_d\right\}^T \boldsymbol{Q}(t) \left\{\boldsymbol{X}(t) - \boldsymbol{X}_d\right\} dt + \int_{t_k}^{t_k+T_c} \dot{\boldsymbol{U}}(t)^T \boldsymbol{P}(t) \dot{\boldsymbol{U}}(t)\, dt \qquad (2.1)$$

subject to the system dynamics

$$\dot{\boldsymbol{X}}(t) = \boldsymbol{A}(\boldsymbol{X})\boldsymbol{X}(t) + \boldsymbol{B}\boldsymbol{U}(t) \qquad (2.2)$$

and the box constraint

$$\left|U_i(t)\right| \leq U^{max} \qquad (2.3)$$

where $\boldsymbol{X}_d$ is the desired states, $U_i(t)$ is the ith element of the control input $\boldsymbol{U}(t)$, U^{max} is the maximum control input available, and ($\boldsymbol{Q}(t)$, $\boldsymbol{P}(t)$) are the time-varying and positive definite symmetric weight matrices, respectively. The solution of the kth CNOC problem is used as the initial condition for the $(k+1)$th CNOC problem.

To solve the CNOC problem, it is discretized into the DNOC problem

over the given receding predictive horizon T_p as follows.

Problem Ψ_{DNOC}: At any time instant $k \in [1, n+1]$, find the sequences of incremental control impulse $\Delta \boldsymbol{U}_k = \boldsymbol{U}_k - \boldsymbol{U}_{k-1}$ and state vectors $\boldsymbol{X}_k$ that minimize the quadratic cost function over the given predictive horizon,

$$\min J_k = \sum_{i=k+1}^{k+N} \{\boldsymbol{X}_i - \boldsymbol{X}_d\}^T \boldsymbol{Q}_k \{\boldsymbol{X}_i - \boldsymbol{X}_d\} + \sum_{i=k}^{k+N_c-1} \Delta \boldsymbol{U}_i^T \boldsymbol{P}_k \Delta \boldsymbol{U}_i \tag{2.4}$$

subject to the system dynamics

$$\boldsymbol{X}_{i+1} = \boldsymbol{A}_i \boldsymbol{X}_i + \boldsymbol{B}_i \boldsymbol{U}_i, \qquad (i = k+1, \ldots, k+N) \tag{2.5}$$

and the box constraint

$$|U_i|_k \le U^{max} \tag{2.6}$$

where the corresponding predictive and control horizons $T_p = NT_s$ and $T_c = N_c T_s$ are placed by N and N_c with the assumption of $N_c \le N$. Note that T_s is the sampling time interval. Moreover, Eq. (2.4) is the discrete representation of Eq.(2.1) by zero-order holder, where the coefficient matrices $\boldsymbol{A}_i$ and $\boldsymbol{B}_i$ are assumed constant within each sampling time interval T_s, but are updated at the beginning of each time interval with the states at the end of previous time interval.

It is worth noting that $\boldsymbol{Q}_k$ and $\boldsymbol{P}_k$ are the weight matrices representing

the two competing aspects of the control: accuracy and smoothness. For cases where the control accuracy is paramount, the weight matrix $\boldsymbol{P}_k$ could be set to a null matrix to guarantee the predicted states tracking the desired states precisely. On the other hand, $\boldsymbol{Q}_k$ could be replaced by a null matrix if the control smoothness is the major concern.

The resulting DNOC problem is computationally heavy and is transformed into a quadratic programming problem whose solution can be obtained as follows. Define the recursive relationship of the control input at any time instant with respect to the *k*th time instant in the control horizon as

$$\begin{cases} \boldsymbol{U}_{k,k} = \Delta\boldsymbol{U}_k + \boldsymbol{U}_{k-1} \\ \boldsymbol{U}_{k+1,k} = \left(\Delta\boldsymbol{U}_{k+1} + \Delta\boldsymbol{U}_k\right) + \boldsymbol{U}_{k-1} \\ \quad \vdots \\ \boldsymbol{U}_{k+N_c-1,k} = \sum_{i=0}^{N_c-1} \Delta\boldsymbol{U}_{k+i} + \boldsymbol{U}_{k-1} \\ \quad \vdots \\ \boldsymbol{U}_{k+i,k} = \boldsymbol{U}_{k+N_c-1,k} \quad \left(i = N_c, \ldots, N\right) \end{cases} \tag{2.7}$$

or in a compact notation

$$\tilde{\boldsymbol{U}}_{k,k} = \tilde{\boldsymbol{M}}\Delta\tilde{\boldsymbol{U}}_k + \tilde{\boldsymbol{F}}\boldsymbol{U}_{k-1} \tag{2.8}$$

where $\boldsymbol{U}_{k+i,k}$ is the predicted control input at the (*k+i*)th time instant with respect to the *k*th time instant, $\boldsymbol{U}_{k-1}$ is the known control input at the *k*th time

instant, $\tilde{\boldsymbol{U}}_{k,k} = \sum_{i=0}^{N_c-1} \boldsymbol{U}_{k+i,k}|i\rangle$ and $\Delta\tilde{\boldsymbol{U}}_k = \sum_{i=0}^{N_c-1} \Delta\boldsymbol{U}_{k+i}|i\rangle$ ($|\cdot\rangle$ is the Ket vector notation), $\tilde{\boldsymbol{M}}$ is a lower triangular matrix with $\tilde{\boldsymbol{M}}(i,j) = \boldsymbol{I}$, $(i \geq j)$, and $\tilde{\boldsymbol{F}} = \sum_{i=1}^{N_c} \boldsymbol{I}|i\rangle$ where $\boldsymbol{I}$ is the identity matrix and its dimension equals to the size of the state vector.

Correspondingly, the set of states $\boldsymbol{X}_{k+j,k}, (j = 1,\ldots,N)$, in the predictive horizon with respect to the kth time instant can be evaluated recursively, such that,

$$\begin{cases} \boldsymbol{X}_{k+1,k} = \boldsymbol{A}_k \boldsymbol{X}_k + \boldsymbol{B}_k \boldsymbol{U}_{k,k} \\ \boldsymbol{X}_{k+2,k} = (\boldsymbol{A}_{k+1}\boldsymbol{A}_k)\boldsymbol{X}_k + (\boldsymbol{A}_{k+1}\boldsymbol{B}_k)\boldsymbol{U}_{k,k} + \boldsymbol{B}_{k+1}\boldsymbol{U}_{k+1,k} \\ \quad\vdots \\ \boldsymbol{X}_{k+N,k} = \prod_{j=0}^{N-1} \boldsymbol{A}_{k+j}\boldsymbol{X}_k + \sum_{j=0}^{N-1}\left[(\prod_{i=1+j}^{N-1} \boldsymbol{A}_{k+i})\boldsymbol{B}_{k+j}\boldsymbol{U}_{k+j,k} \right] \end{cases} \tag{2.9}$$

Substituting Eq.(2.8) into Eq.(2.9) yields the set of predicted states $\boldsymbol{X}_{k+j,k}, (j = 1,\ldots,N)$, in terms of $\Delta\tilde{\boldsymbol{U}}_{k,k}$ and in the compact notation as,

$$\tilde{\boldsymbol{X}}_k^p = \boldsymbol{\phi}\boldsymbol{X}_k + \boldsymbol{\Gamma}\boldsymbol{U}_{k-1} + \boldsymbol{G}\Delta\tilde{\boldsymbol{U}}_k \tag{2.10}$$

or

$$\begin{Bmatrix} \boldsymbol{X}_{k+1|k} \\ \boldsymbol{X}_{k+2|k} \\ \vdots \\ \boldsymbol{X}_{k+N_c|k} \\ \boldsymbol{X}_{k+N_c+1|k} \\ \vdots \\ \boldsymbol{X}_{k+N|k} \end{Bmatrix} = \begin{Bmatrix} \boldsymbol{A}_k \\ \boldsymbol{A}_{k+1}\boldsymbol{A}_k \\ \vdots \\ \prod_{m=0}^{N_c-1} \boldsymbol{A}_{k+m} \\ \prod_{m=0}^{N_c} \boldsymbol{A}_{k+m} \\ \vdots \\ \prod_{m=0}^{N-1} \boldsymbol{A}_{k+m} \end{Bmatrix} \boldsymbol{X}(k) + \begin{Bmatrix} \boldsymbol{B}_k \\ \boldsymbol{B}_{k+1} \\ \vdots \\ \sum_{l=0}^{N_c-1} (\prod_{i=1+l}^{j-1} \boldsymbol{A}_{k+i}) \boldsymbol{B}_{k+l} \\ \left[\sum_{l=0}^{N_c-1} (\prod_{i=1+l}^{N_c} \boldsymbol{A}_{k+i}) \boldsymbol{B}_{k+l} \right] + \boldsymbol{B}_{N_c} \\ \vdots \\ \left[\sum_{l=0}^{N_c-1} (\prod_{i=1+l}^{N-1} \boldsymbol{A}_{k+i}) \boldsymbol{B}_{k+l} \right] + \left[\sum_{m=N_c+1}^{N} (\prod_{i=m}^{N-1} \boldsymbol{A}_i) \boldsymbol{B}_{i-1} \right] \end{Bmatrix} \boldsymbol{U}_{k-1} +$$

$$\begin{bmatrix} \boldsymbol{B}_k & \cdots & \boldsymbol{0} \\ \boldsymbol{A}_{k+1}\boldsymbol{B}_k + \boldsymbol{B}_{k+1} & \cdots & \boldsymbol{0} \\ \vdots & \ddots & \vdots \\ \sum_{l=0}^{N_c-1} (\prod_{i=1+l}^{N_c-1} \boldsymbol{A}_{k+i}) \boldsymbol{B}_{k+l} & \cdots & \boldsymbol{B}_{k+N_c-1} \\ \left[\sum_{l=0}^{N_c-1} (\prod_{i=1+l}^{N_c} \boldsymbol{A}_{k+i}) \boldsymbol{B}_{k+l} \right] + \boldsymbol{B}_{N_c} & \cdots & (\boldsymbol{A}_{N_c}\boldsymbol{B}_{k+N_c-1} + \boldsymbol{B}_{N_c}) \\ \vdots & \ddots & \vdots \\ \left[\sum_{l=0}^{N_c-1} (\prod_{i=1+l}^{N-1} \boldsymbol{A}_{k+i}) \boldsymbol{B}_{k+l} \right] + \left[\sum_{m=N_c+1}^{N} (\prod_{i=m}^{N-1} \boldsymbol{A}_i) \boldsymbol{B}_{i-1} \right] & \cdots & (\prod_{i=N_c}^{N-1} \boldsymbol{A}_i) \boldsymbol{B}_{k+N_c-1} + \left[\sum_{m=N_c+1}^{N} (\prod_{i=m}^{N-1} \boldsymbol{A}_i) \boldsymbol{B}_{i-1} \right] \end{bmatrix} \begin{Bmatrix} \Delta \boldsymbol{U}_{k|k} \\ \vdots \\ \Delta \boldsymbol{U}_{k+N_c-1|k} \end{Bmatrix} \quad (2.11)$$

where $\tilde{\boldsymbol{X}}_k^p = \sum_{i=1}^{N} \boldsymbol{X}_{k+i,k} | i \rangle$ and the superscript p indicates the vector is composed of the predicted states. Notably, the coefficient matrices $\boldsymbol{\phi}$, $\boldsymbol{\Gamma}$ and $\boldsymbol{G}$ are constant within each time step but are updated at the beginning of each step with the states at the end of previous step. For the sake of derivation convenience, the subscript k is omitted and the same is applied to the matrices $\boldsymbol{E}$, $\boldsymbol{H}$ and $\boldsymbol{C}$ to be discussed later. Furthermore, the cost function in Eq.(2.4) is rewritten in a compact form,

$$\min J_k = \left\{ \tilde{\boldsymbol{X}}_k^p - \tilde{\boldsymbol{X}}_d \right\}^T \tilde{\boldsymbol{Q}} \left\{ \tilde{\boldsymbol{X}}_k^p - \tilde{\boldsymbol{X}}_d \right\} + \Delta \tilde{\boldsymbol{U}}_k^T \tilde{\boldsymbol{P}} \Delta \tilde{\boldsymbol{U}}_k \tag{2.12}$$

where $\tilde{\boldsymbol{X}}_d = \sum_{i=1}^{N} \boldsymbol{X}_d | i \rangle$, $\tilde{\boldsymbol{Q}} = \overset{N}{\underset{i=1}{\oplus}} \boldsymbol{Q}_i$ and $\tilde{\boldsymbol{P}} = \overset{N_c}{\underset{i=1}{\oplus}} \boldsymbol{P}_i$ ($\oplus$ is the direct sum notation). It is worth noting that the weight matrices $\tilde{\boldsymbol{Q}}$ and $\tilde{\boldsymbol{P}}$ inherit the symmetric property from $\boldsymbol{Q}_i, (i = 1, 2, ..., N)$ and $\boldsymbol{P}_i, (i = 1, 2, ..., N_c)$, and thus $\tilde{\boldsymbol{Q}} = \tilde{\boldsymbol{Q}}^T$ and $\tilde{\boldsymbol{P}} = \tilde{\boldsymbol{P}}^T$.

Defining and substituting an auxiliary vector $\boldsymbol{E} = \tilde{\boldsymbol{X}}_d - \boldsymbol{\phi} \tilde{\boldsymbol{X}}_k^p - \boldsymbol{\Gamma} \boldsymbol{U}_{k-1}$ into Eq.(2.12) yield,

$$\begin{aligned} \min J_k &= \left\{ \boldsymbol{G} \Delta \tilde{\boldsymbol{U}}_k - \boldsymbol{E} \right\}^T \tilde{\boldsymbol{Q}} \left\{ \boldsymbol{G} \Delta \tilde{\boldsymbol{U}}_k - \boldsymbol{E} \right\} + \Delta \tilde{\boldsymbol{U}}_k^T \tilde{\boldsymbol{P}} \Delta \tilde{\boldsymbol{U}}_k \\ &= \left\{ \Delta \tilde{\boldsymbol{U}}_k^T \boldsymbol{G}^T - \boldsymbol{E}^T \right\} \tilde{\boldsymbol{Q}} \left\{ \boldsymbol{G} \Delta \tilde{\boldsymbol{U}}_k - \boldsymbol{E} \right\} + \Delta \tilde{\boldsymbol{U}}_k^T \tilde{\boldsymbol{P}} \Delta \tilde{\boldsymbol{U}}_k \\ &= \Delta \tilde{\boldsymbol{U}}_k^T \left[\boldsymbol{G}^T \tilde{\boldsymbol{Q}} \boldsymbol{G} + \tilde{\boldsymbol{P}} \right] \Delta \tilde{\boldsymbol{U}}_k - 2 \boldsymbol{E}^T \tilde{\boldsymbol{Q}} \boldsymbol{G} \Delta \tilde{\boldsymbol{U}}_k^T + \boldsymbol{E}^T \tilde{\boldsymbol{Q}} \boldsymbol{E} \\ &= \frac{1}{2} \Delta \tilde{\boldsymbol{U}}_k^T \boldsymbol{H} \Delta \tilde{\boldsymbol{U}}_k + \boldsymbol{C}^T \Delta \tilde{\boldsymbol{U}}_k^T + \boldsymbol{E}^T \tilde{\boldsymbol{Q}} \boldsymbol{E} \end{aligned} \tag{2.13}$$

where $\boldsymbol{H} = 2\left[\boldsymbol{G}^T \tilde{\boldsymbol{Q}} \boldsymbol{G} + \tilde{\boldsymbol{P}} \right]$ is the Hessian matrix that is positive definite and symmetric, $\boldsymbol{C} = -2 \boldsymbol{G}^T \tilde{\boldsymbol{Q}} \boldsymbol{E}$ is a column vector with the same dimension of $\Delta \tilde{\boldsymbol{U}}_k$. Note that the vector $\boldsymbol{E}$ is constant within each time interval. Thus, the term $\boldsymbol{E}^T \tilde{\boldsymbol{Q}} \boldsymbol{E}$ is constant and does not affect the minimization of the cost function. It can be safely ignored from the cost function. Accordingly, Eq.(2.13) is equivalent to the following standard QP problem.

Problem Ψ_{QP}: find $\Delta\tilde{\boldsymbol{U}}_k$ that minimizes the following cost function,

$$\min J_k = \frac{1}{2}\Delta\tilde{\boldsymbol{U}}_k^T \boldsymbol{H}\Delta\tilde{\boldsymbol{U}}_k + \boldsymbol{C}^T\Delta\tilde{\boldsymbol{U}}_k \tag{2.14}$$

The positive definite matrix $\boldsymbol{H}$ makes it a convex optimization problem where $\Delta\tilde{\boldsymbol{U}}_k$ is a global minimum.

4.2 Control Magnitude Constraint

The original constraint imposed on the control input is shown as Eq.(2.6), it can be converted to the inequality constraint in terms of the augmented control increments $\Delta\tilde{\boldsymbol{U}}_k$ by substituting Eq.(2.8) into Eq.(2.6), yields:

$$-\tilde{\boldsymbol{U}}^{max} \le \tilde{\boldsymbol{M}}\Delta\tilde{\boldsymbol{U}}_k + \tilde{\boldsymbol{F}}\boldsymbol{U}_{k-1} \le \tilde{\boldsymbol{U}}^{max} \tag{2.15}$$

or

$$\begin{bmatrix} \tilde{\boldsymbol{M}} \\ -\tilde{\boldsymbol{M}} \end{bmatrix}\Delta\tilde{\boldsymbol{U}}_k \le \begin{Bmatrix} \tilde{\boldsymbol{U}}^{max} - \tilde{\boldsymbol{F}}\boldsymbol{U}_{k-1} \\ \tilde{\boldsymbol{U}}^{max} + \tilde{\boldsymbol{F}}\boldsymbol{U}_{k-1} \end{Bmatrix} \tag{2.16}$$

where $\tilde{\boldsymbol{U}}^{max} = \sum_{i=1}^{N_c} \boldsymbol{U}^{max}|i\rangle$.

4.3 Line-of-Sight Constraint

The LOS constraint helps not only maintain the visual contact with the target, but also defines the tolerate limit for the control of relative position of

the chaser. It should be noted that the LOS constraint could be imposed on x-, y-, z-axis directions depending on the requirement of the mission, although only the LOS constrains in the minus y- and x-axis are given in this section.

Assume the target is moving in an elliptic orbit with a stable attitude. The chaser approaches the target autonomously from the minus *y*-axis Fig. 4.1 or *x*-axis Fig. 4.2, respectively. To avoid the collision with the target, the chaser is required to approach the target within a corridor defined by a rectangular cone of LOS originated at the docking port with two half-angles constructed around the docking axis, such that,

$$\begin{cases} -\tan\alpha \le \dfrac{z_k}{-y_k - l} \le \tan\alpha \\ -\tan\beta \le \dfrac{x_k}{-y_k - l} \le \tan\beta \end{cases} \text{; along minus } y\text{-axis} \tag{2.17}$$

$$\begin{cases} -\tan\alpha \le \dfrac{y_k}{-x_k - l} \le \tan\alpha \\ -\tan\beta \le \dfrac{z_k}{-x_k - l} \le \tan\beta \end{cases} \text{; along minus } x\text{-axis} \tag{2.18}$$

where x_k, y_k and z_k are the relative position coordinates of the chaser in the LVLH frame at time instant k, l is the distance from the CM of the target to the origin of LOS cone located at the docking port, α and β are the half angles of cone in the *z*-axis and *x*-axis directions, respectively.

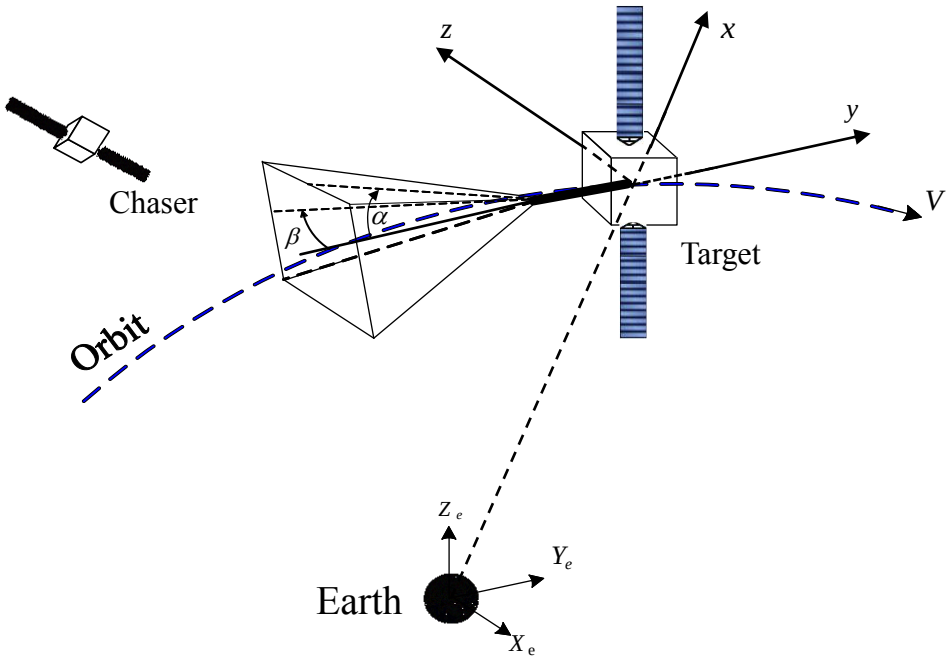

Figure 4.1 Chaser approaching target from minus y-axis

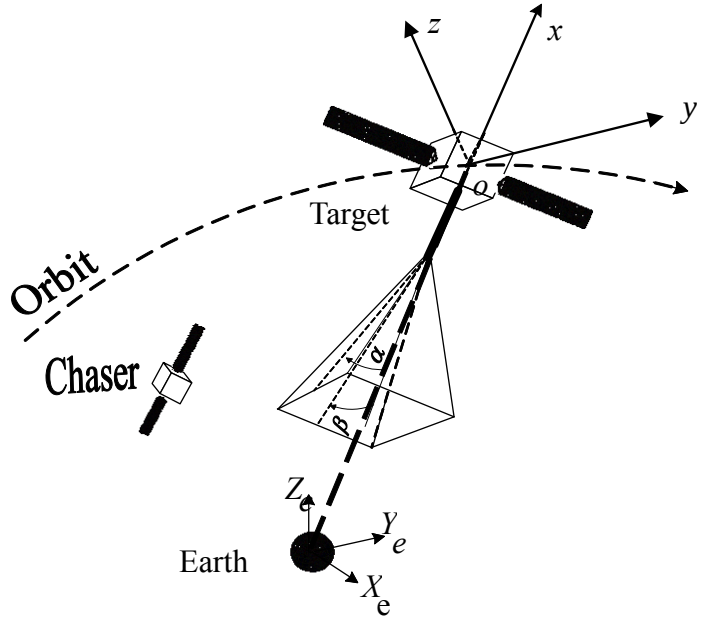

Figure 4.2 Chaser approaching target from minus x-axis

Then, the LOS constraint can be converted to the standard inequality form as follows,

$$\boldsymbol{A}_s \begin{Bmatrix} x_k \\ y_k \\ z_k \end{Bmatrix} \le -\boldsymbol{l} \tag{2.19}$$

with

$$\boldsymbol{A}_s = \begin{bmatrix} 0 & 1 & -\cot\alpha \\ 0 & 1 & \cot\alpha \\ \cot\beta & 1 & 0 \\ -\cot\beta & 1 & 0 \end{bmatrix},\ \boldsymbol{l} = \begin{Bmatrix} l \\ l \\ l \\ l \end{Bmatrix};\ \text{along minus } y\text{-axis} \tag{2.20}$$

$$\boldsymbol{A}_s = \begin{bmatrix} 1 & \cot\alpha & 0 \\ 1 & -\cot\alpha & 0 \\ 1 & 0 & \cot\beta \\ 1 & 0 & -\cot\beta \end{bmatrix},\ \boldsymbol{l} = \begin{Bmatrix} l \\ l \\ l \\ l \end{Bmatrix};\ \text{along minus } x\text{-axis} \tag{2.21}$$

The LOS constraint imposed on the states can be further formulated in terms of the augmented vector of predicted states $\tilde{\boldsymbol{X}}_k^p$, such that,

$$\tilde{\boldsymbol{A}}_s \tilde{\boldsymbol{X}}_k^p \le -\tilde{\boldsymbol{l}} \tag{2.22}$$

where $\bar{\boldsymbol{A}}_s = \left[\boldsymbol{A}_s, \boldsymbol{0}_{4\times 3}\right] \in \Re^{4\times 6}$, $\tilde{\boldsymbol{A}}_s = \bigoplus_{i=1}^{N} \bar{\boldsymbol{A}}_s$ and $\tilde{\boldsymbol{l}} = \sum_{i=1}^{N} \boldsymbol{l}_i |i\rangle$.

Next, the constraint on the state is converted to the inequality constraint in terms of the augmented control increments $\Delta\tilde{\boldsymbol{U}}_k$ which is the solution of the

QP problem. Substitute Eq.(2.10) into Eq.(2.22) yield the constraints in terms of $\Delta\tilde{\boldsymbol{U}}_k$, yields:

$$\tilde{\boldsymbol{A}}_s \boldsymbol{G}\Delta\tilde{\boldsymbol{U}}_k \le -\tilde{\boldsymbol{l}} - \tilde{\boldsymbol{A}}_s\boldsymbol{\phi}\boldsymbol{X}_k - \tilde{\boldsymbol{A}}_s\boldsymbol{\Gamma}\boldsymbol{U}_{k-1} \tag{2.23}$$

So far, the original optimal control problem has been converted into a standard QP problem subject to the equality and inequality constraints.

4.4 Stability Analysis with Terminal State Constraint

To the best of our knowledge, a lot of research focused on the stability analysis of the NMPC. However, there is no universal stability theory proposed for it [100]. The close-loop stability is important for controller design and Lyapunov theory is a candidate approach to prove the stability of the NMPC [101]. The nonlinearity introduced by the constraints may make the NMPC a nonlinear control problem [102]. Generally, the close-loop stability of the model predictive controller can be proved under certain conditions [103]. The detailed discussion on the stability theory of NMPC is comprehensively stated in the literatures [54].

The core to establish closed-loop stability is based on an equality constraint on the terminal state, which is $x\left(k+N|k\right)=0$. Take the single-input system as an example, the closed-loop model predictive control system is asymptotically stable based on the following assumptions [57],

1. An additional constraint $x(k+N|k)=0$ is placed on the final state of the receding horizon optimization problem, the terminal state constraint $x(k+N|k)=0$ is a result of the control sequence $\Delta u(k+m)=L(m)^T\eta$, $(m=0,1,2,\ldots,N)$.

2. For each sampling instant k, there exists a solution η such that the cost function is minimized subject to the inequality constraints and terminal state constraint $x(k+N|k)=0$.

Proof. The key to the stability result is to construct a Lyapunov function for the model predictive control system. Choose the cost function as the Lyapunov candidate function $V(x(k),k)$,

$$V(x(k),k)=\sum_{m=1}^{N}x(k+m|k)^T\boldsymbol{Q}x(k+m|k)+\sum_{m=0}^{N-1}\Delta u(k+m)^T\boldsymbol{P}\Delta u(k+m) \qquad (2.24)$$

where $x(k+m|k)=A^m x(k)+\sum_{i=0}^{m-1}A^{m-i-1}BL(i)^T\eta^k$ and η^k is, at time k, the parameter vector solution of the original cost function with respect to both inequality and equality constraints, and $\Delta u(k+m)=L(m)^T\eta^k$. The existence of η^k is ensured by the second assumption stated in the theorem. Namely, $V(x(k),k)=J_{\min}$, where η^k is a function of $x(k)$. It is seen that $V(x(k),k)$ is positive definite and $V(x(k),k)$ tends to infinity if $x(k)$ tends to infinity. Similarly, the Lyapunov candidate function at time instant (k+1) becomes,

$$V\left(x(k+1),k+1\right)=\sum_{m=1}^{N}x\left(k+1+m|k+1\right)^{T}\boldsymbol{Q}x\left(k+1+m|k+1\right)+\sum_{m=0}^{N-1}\Delta u\left(k+1+m\right)^{T}\boldsymbol{P}\Delta u\left(k+1+m\right) \tag{2.25}$$

And $x\left(k+1+m|k+1\right)=\boldsymbol{A}^{m}x\left(k+1\right)+\sum_{i=0}^{m-1}\boldsymbol{A}^{m-i-1}\boldsymbol{B}L\left(i\right)^{T}\eta^{k+1}$, η^{k+1} is the parameter vector solution at (k+1) and $\Delta u\left(k+1+m\right)=L\left(m\right)^{T}\eta^{k+1}$.

Assuming that all constraints are satisfied at the sample time k, a feasible solution of η^{k+1} for the initial state information $x\left(k+1\right)$ in the receding horizon is η^{k}. Therefore, the feasible control sequence at (k+1) is to shift the elements in $L\left(0\right)^{T}\eta^{k}$, $L\left(1\right)^{T}\eta^{k}$, $L\left(2\right)^{T}\eta^{k}$,..., $L\left(N-1\right)^{T}\eta^{k}$ one step forward and replace the last element by zero to obtain the sequence $L\left(1\right)^{T}\eta^{k}$, $L\left(2\right)^{T}\eta^{k}$,..., $L\left(N-1\right)^{T}\eta^{k}$, 0. Because of the optimality in the solution of η^{k+1}, it is seen that

$$V\left(x(k+1),k+1\right)\le\bar{V}\left(x(k+1),k+1\right) \tag{2.26}$$

where $\bar{V}\left(x(k+1),k+1\right)$ is similar to Eq.(2.25) except that the control sequence is replaced by the feasible sequence $L\left(1\right)^{T}\eta^{k}$, $L\left(2\right)^{T}\eta^{k}$,..., $L\left(N-1\right)^{T}\eta^{k}$, 0. The difference between $V\left(x(k+1),k+1\right)$ and $V\left(x(k),k\right)$ is then bounded by

$$V\left(x(k+1),k+1\right)-V\left(x(k),k\right)\le\bar{V}\left(x(k+1),k+1\right)-V\left(x(k),k\right) \tag{2.27}$$

Note that because the $\bar{V}\left(x\left(k+1\right),k+1\right)$ shares the same control sequence and the same state sequence with $V\left(x\left(k\right),k\right)$ for the sample time k+1, k+2, …, k+N–1, the difference between these two functions is,

$$\begin{aligned}\bar{V}\left(x\left(k+1\right),k+1\right)-V\left(x\left(k\right),k\right)&=x\left(k+N\left|k\right.\right)^{T}\boldsymbol{Q}x\left(k+N\left|k\right.\right)\\&-x\left(k+1\right)^{T}\boldsymbol{Q}x\left(k+1\right)-\Delta u\left(k\right)^{T}\boldsymbol{P}\Delta u\left(k\right)\end{aligned}\tag{2.28}$$

From the first assumption, we have

$$\bar{V}\left(x\left(k+1\right),k+1\right)-V\left(x\left(k\right),k\right)=-x\left(k+1\right)^{T}\boldsymbol{Q}x\left(k+1\right)-\Delta u\left(k\right)^{T}\boldsymbol{P}\Delta u\left(k\right)\tag{2.29}$$

Hence, the difference of the Lyapunov function is

$$V\left(x\left(k+1\right),k+1\right)-V\left(x\left(k\right),k\right)\le-x\left(k+1\right)^{T}\boldsymbol{Q}x\left(k+1\right)-\Delta u\left(k\right)^{T}\boldsymbol{P}\Delta u\left(k\right)<0\tag{2.30}$$

The negative difference indicates the asymptotic stability of the model predictive control system.

Chapter 5 CASE STUDIES

Summary: Considering the particular requirements of different space missions, the NMPC is combined with various techniques to construct different control schemes. In particular, the PWPF technique is integrated into the NMPC to modulate the continuous control force into the on/off form during the autonomous rendezvous with an attitude stable target. Further, the NMPC is applied to the tumbling model and LOS model when approaching a tumbling target spacecraft. Moreover, the RLS method is adopted in combination with the NMPC during the attitude control of compound spacecraft in post-capturing phase. The effectiveness of the various control schemes is explicitly validated, and the detailed numerical simulations are given in this chapter. The theories and simulation results have been published in reference papers A, B and C as listed at the end of Chapter 1.

5.1 PWPF Modulation Based Autonomous Rendezvous

In this section, a new scheme of PWPF based NMPC is proposed in ARPO near a non-cooperative target using on-off thrusters. Practical

constraints on actuators' magnitude and LOS are imposed in the NMPC algorithm to prevent the collision between two spacecraft. The optimal control problem is formulated by converting the continuous control input into a sequence of pulses of constant magnitude by controlling the thruster firing frequency and duration.

The control objective is to optimize the control accuracy and control smoothness subjected to the discontinuous on-off propulsion system. The optimized continuous control input at each sampling instant is converted to a sequence of on-off pulses by a PWPF modulator to control thrusters' firing. Subsequently in the numerical simulation, the effectiveness of the newly proposed integration of NMPC and PWPF modulation is proved to be more energy efficient compared with continuous control force.

5.1.1 Numerical Implementation

Based on the receding horizon strategy, the optimization process keeps being shifted forward with the constrained QP that is solved at each iteration step. Once the control corrections $\Delta\tilde{\boldsymbol{U}}_k$ are solved, the control input at the time instant k and the state at the time instant $k+1$ are updated. The process diagram is shown in Fig. 5.1, where the continuous control force is applied to spacecraft directly.

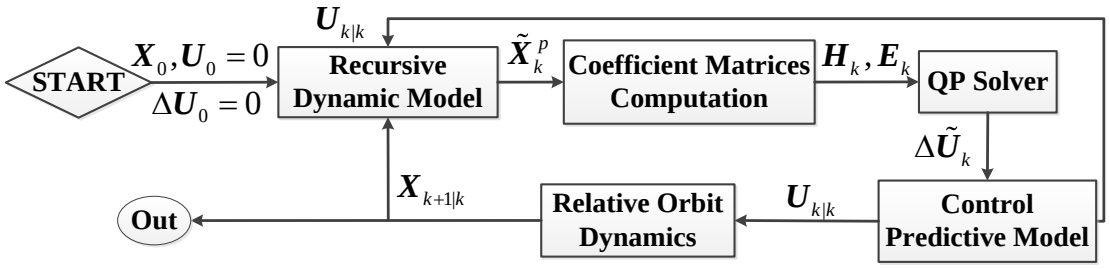

Figure 5.1 Block diagram of NMPC without PWPF modulation

The NMPC with continuous thrust can be extended to the discrete thrusts with constant magnitude as shown in Fig. 5.2. This is achieved by feeding a continuous control input to the PWPF modulator at each time instant, which controls the thruster system to generate a series of on-off pulses.

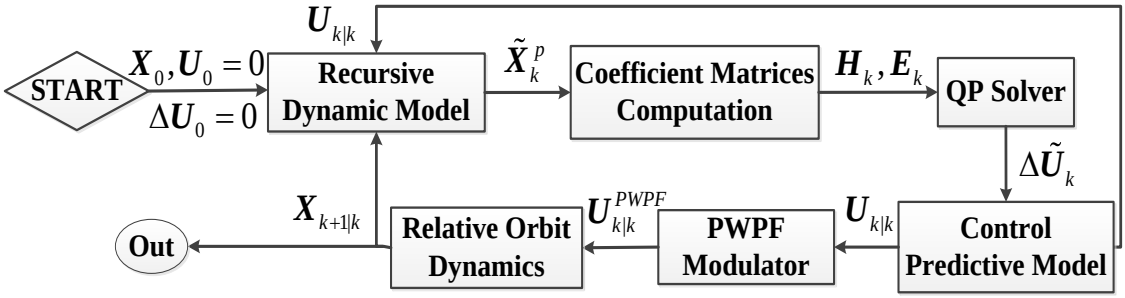

Figure 5.2 Block diagram of NMPC with PWPF modulation

The models of continuous force and discrete force are listed as above. The modulated pulse sequence is obtained by modulating the continuous force in each channel and the thrusters are switched on and off repeatedly to drive the chaser approaching the target spacecraft while reducing the relative velocity. The PWPF modulator, working in alternative on-off mode, is used to generate an equivalent thrusting effect on the chaser with equal maximum control output.

5.1.2 Results and Discussion

The advantage of the NMPC with PWPF modulation is demonstrated in the ARPO of a three-axis stable target in an elliptical orbit by comparing the results of the NMPC without PWPF modulation. Assume the chaser approaches the target along the minus V-bar direction. The masses of the target and the chaser are 800 *kg* and 50 *kg*, respectively. The initial position and velocity of the chaser with respect to the target are defined as {-3 *m*, -50 *m*, -1 *m*}^{T} and {0.01 *m/s*, 0.05 *m/s*, 0.03 *m/s*}^{T}. The docking axis is 0.1 *m* long, measured from the surface of the target to the docking port. The target is a cubic shape and its dimension is 1x1x1 *m*. Therefore, the docking port is 1.1 *m* away from the target's CM to and the desired final states are {0 *m*, -1.1 *m*, 0 *m*}^{T} and {0, 0, 0}^{T} , respectively. The maximum continuous force is set 1.5 *N* and simulation time is set 120 *s* for all cases in the final approaching process. The orbital elements of the target, control parameters and ranges of PWPF parameters are given in Tables 5.1, 5.2 and 5.3, respectively. Furthermore, the values of the PWPF parameters in this simulation are given as $K_m = 4$, $T_m = 1$, $U_{on} = 0.5$, $U_{off} = 0.1$ and $U_m = 1.5$. Finally, the on-off frequency of thrusters is defined as 10 *Hz*.

Table 5.1 Orbital elements of target

Parameters	Values

Eccentricity	0.3
Semi-major axis, km	12000
Inclination, deg	10°
Argument of perigee, deg	30°
Right ascension of the ascending node, deg	10°
True anomaly, deg	0°

Table 5.2 Parameters of NMPC

Parameters	Values
State weight matrix	$\boldsymbol{Q} = 1 \times I_{N \cdot state\_num}$
Control weight matrix	$\boldsymbol{P} = 10 \times I_{N_c \cdot ctrl\_num}$
Predictive horizon	$N = 450$
Control horizon	$N_c = 3$
Sampling time	$T_s = 0.1$ s

Table 5.3 Parameter ranges of PWPF modulator

Parameters	Values
Filter gain K_m	3-6
Time constant T_m	0.7-1.2
On-value U_{on}	*0.5-0.8*

Off-value U_{off}	0.1-0.4
Schmitt trigger Output U_m, N	2-8

To compare the energy consumption by the continuous force and modulated pulse control, an energy index is constructed as follows,

$$w(t) = \int_0^t \|u\|^2 d\tau$$

where $w(t)$ is an energy index with the unit of $N^2 s$.

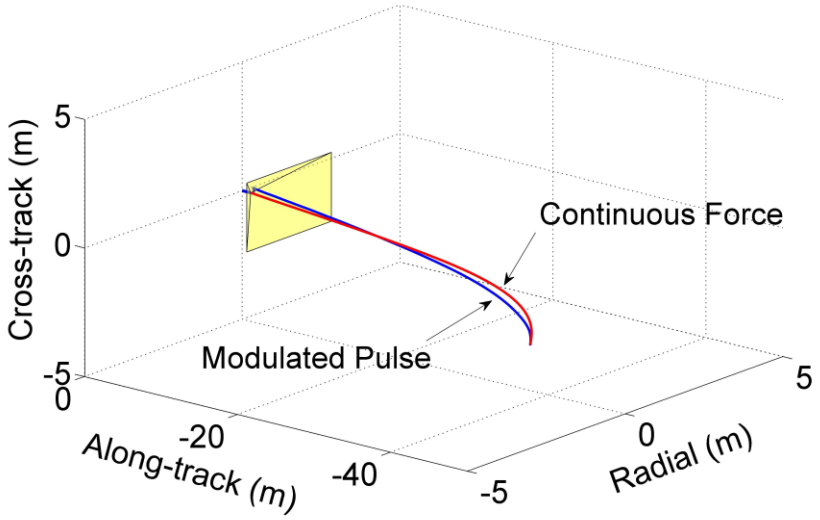

(a)

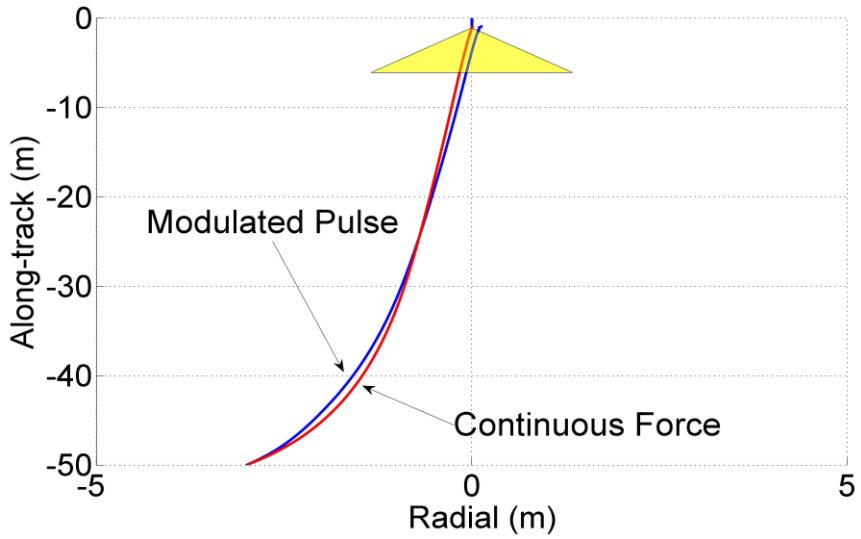

(b)

Figure 5.3 Approaching trajectory (a) and its projections (b)

The 3D (three-dimensional) views of the optimized approaching trajectory of the chaser from the minus V-bar direction are shown in Fig. 5.3, where the projected view of the LOS is shown as the triangle. The LOS constraint is represented by the yellow cubic cone in Fig. 5.3 (a) and yellow triangle in Fig. 5.3 (b). All trajectories with and without the PWPF modulation fall within the LOS and satisfy the safety constraint. Both trajectories approach the docking port nearly along a straight line from the minus V-bar direction in the final stage, leading to a successful docking.

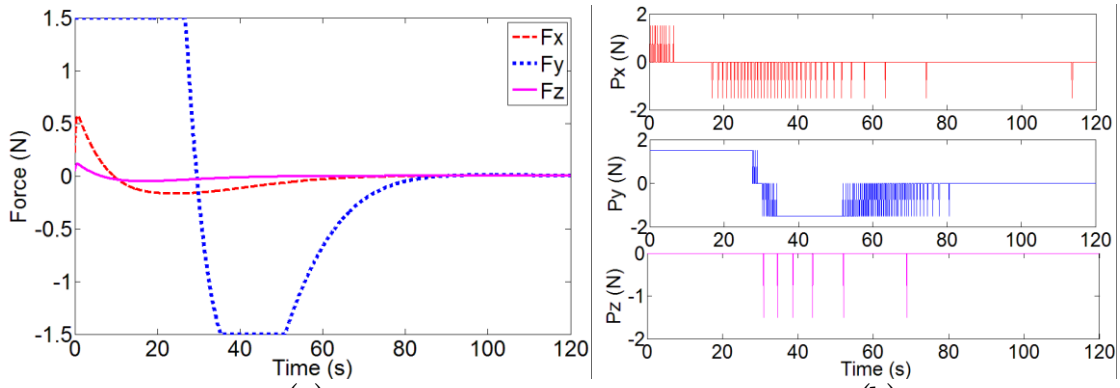

(a) (b)

Figure 5.4 Controls (a) continuous and (b) modulated pulses

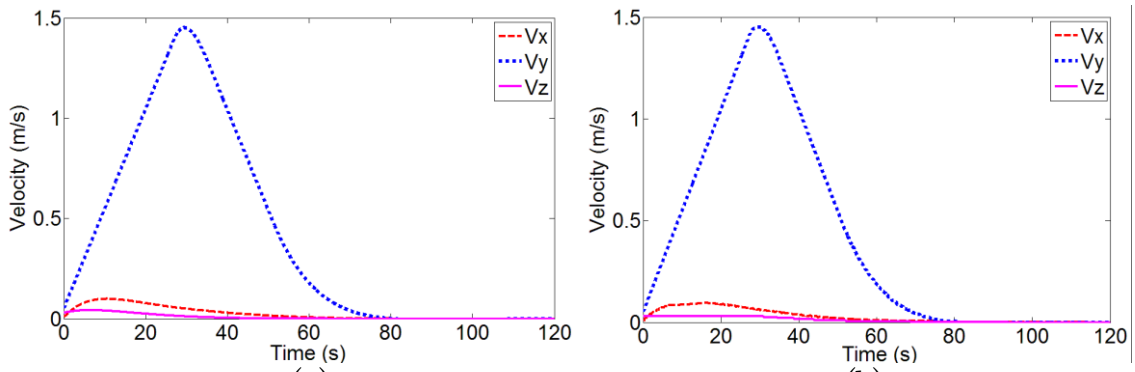

(a) (b)

Figure 5.5 Relative velocity (a) continuous and (b) modulated pulses

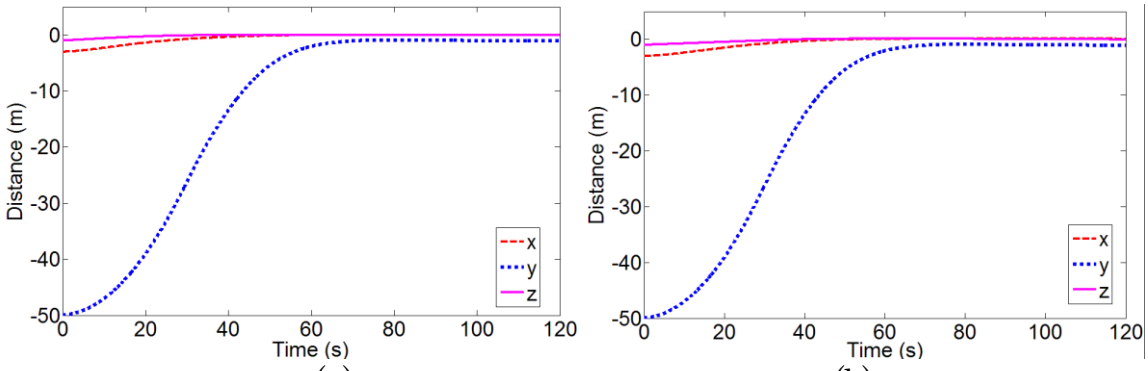

(a) (b)

Figure 5.6 Relative distance (a) continuous and (b) modulated pulses

Next, the time histories of relative distance, velocity and controls of the chaser are shown in Figs. 5.4-5.6. To compare the results based on the same benchmark, the maximum output for continuous and pulse forces are

restricted to no more than 1.5 *N*, the negative thrust, 5 *N*, means the thrusters are firing to the opposite direction. It shows clearly in Fig. 5.4 that both the continuous and pulse forces reach the maximum limit to reduce the relatively large distance in the *y*-axis at the beginning, then the chaser starts to slow down by firing the thrusters at the opposite direction when the relative distance in the *y*-axis is reduced to 30 *m* to ensure the safety. As required thrust reduced in the final stage, the difference between two thrusting methods in the approaching position and velocity becomes unnoticeable. As the chaser is in the close proximity of the target, the thrusts in the y and z-directions are turned off completely to avoid excessive firings.

Furthermore, since the two spacecraft are assumed static before the final approaching starts, thus firing thrusters inevitably speeds up the chaser and causes a large relative velocity, less than 1.5 *m/s* as in Fig. 5.5. However, the relative velocity decreases gradually after reaching the peak and no overshoot in the relative distance curves is caused. In particular, the trajectories of relative distance and relative velocity by the modulated pulses show a stable and gradual transient response with almost no overshoot, seen in Fig. 5.6, although thrusters fire frequently at different time instants. Zero overshoot in y-direction shows the collision is avoided in the final approaching process, in the meantime, zero overshoot in x- and z- directions indicate that the chaser does not need to adjust its position back and forth resulting less

consumption of fuel, and zero overshoot. For instance, Fig. 5.7 shows the energy index in both cases, where the discrete pulse case is 117.22 N^2s and the continuous force case is 103.19 N^2s. Thus, the NMPC with the PWPF modulation is advantageous in reducing fuel consumption.

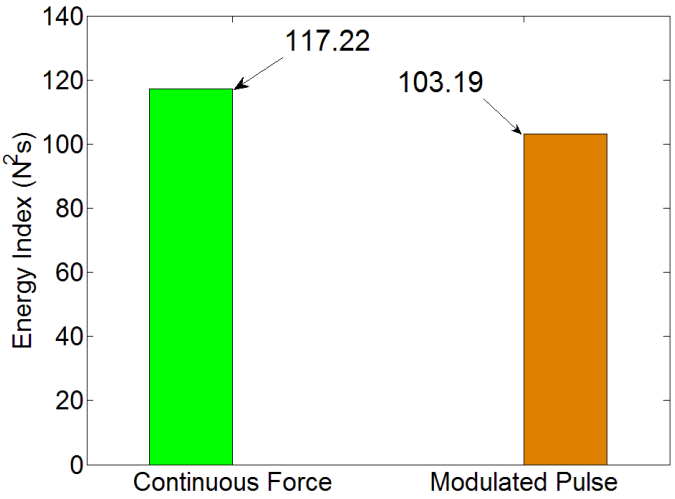

Figure 5.7 Energy consumption

It is worth noting that a shorter approaching time, generally, requires relatively large control force, this may yield a large relative velocity in the middle of approaching and further lead to a higher energy consumption. Further, feasible solution to complete the rendezvous in very short time may not exist in extreme cases, and thus fail to satisfy the same constraints. By contrast, a longer approaching time requires relatively small force since the chaser can speed up and slow down slowly and gradually without causing sudden change in the relative velocity.

Table 5.4 Control precision comparison

Parameters	Continuous Force	Modulated Pulse
x, m	0.0006	0.0825
y, m	0.0188	0.0115
z, m	0.0000	0.0213
$\dot{x}$ *, m/s*	0.0001	0.0029
$\dot{y}$ *, m/s*	0.0010	0.0020
$\dot{z}$ *, m/s*	0.0000	0.0000

Finally, the control precision of final states by two methods is shown in Table 5.4. Obviously, the continuous force achieves better precision than the pulse thrust. This is because the continuous thrust is able to meet the control requirement of NMPC exactly and can generate arbitrarily small force in the last few meters. However, to meet the momentarily peak thrust may lead to an unnecessary large thruster, which will add extra mass to the spacecraft. Furthermore, the continuous and variable output of thrust poses an engineering challenge to the thrust design. The NMPC with the PWPF modulation avoids these challenges by using modulated pulses.

It is interesting to note that the errors occur although the maximum thrusts required in these directions are comparable with the magnitude of pulses. This is partially due to the thrusters stop firing in the docking stage. Additionally, the reason behind this is that the thrusters can only generate control pulse with fixed magnitude, thus error occurs when the magnitude of

the continuous force is either too large or too small, compared with the designated magnitude of the thrusters. To circumvent this difficulty, future study can concentrate on the artificial intelligence algorithm to online tune the parameters in the PWPF modulator, or other modulation techniques, based on the generated continuous control force at every time instant. Furthermore, by lowering the value of U_{off}, the thrusters will fire for a longer period in the docking stage to reduce the position and velocity errors. However, this will result in excessive firings and high fuel consumption. Therefore, a trade-off between the fuel consumption and the control error should be carefully considered for the potential implementation of the proposed control algorithm.

5.1.3 Conclusion

This section develops a new scheme of PWPF based NMPC in ARPO to accommodate the widely used constant output thrusters while achieve lower fuel consumption. The control problem is formulated by integrating the PWPF into the NMPC to minimize the control error and control roughness for a safe, smooth and fuel-efficient approaching trajectory. The resulting nonlinear programming problem is converted into a series of convex QP problems subject to operational constraints and then solved at every sample time instant. Numerical simulations are conducted to compare the control performances of NMPC with and without PWPF in ARPO of a three-axis stabilized target. The results show that the NMPC with PWPF is capable of achieving control

objective with the equal maximum output of control force, less fuel consumption and acceptable control time and accuracy. To find the optimal set of PWPF parameters to further reduce the control error remains a topic worth studying, following research can focus on using artificial intelligence techniques or global optimization methods to search appropriate values of parameters in PWPF modulator and other modulating techniques.

5.2 Tumbling Model based Autonomous Rendezvous

This section focuses on the control of autonomous rendezvous with attitude stable or spinning targets in an elliptical orbit. In a more general case, the tumbling is likely to spin around its axisymmetric axis. The target's spinning angular velocity is unknown but measurable to the chaser spacecraft. The previous work is extended by mathematically introducing the tumbling plane where the spinning axis is rotating. The tumbling plane is assumed perpendicular to the spinning axis that is constantly rotating within this plane. Therefore, the constrained control problem of approaching a tumbling non-cooperative target is more challenging and requires further study.

The linearized TH equation is used to describe the motion of spacecraft and the problem is formulated as model predictive control. The control objective is to maximize control accuracy and smoothness simultaneously to avoid unexpected change or overshoot of trajectory for safe rendezvous. And

the objective is achieved by minimizing the weighted summations of control errors and increments. The effects of two sets of horizons (control and predictive horizons) in the model predictive control are examined in terms of fuel consumption, rendezvous time and computational effort. This is less investigated compared with its counterpart of cooperative targets without the requirement of control smoothness, to the best knowledge of authors. Subsequently, numerical simulations are conducted to verify the effectiveness of the proposed approach and the influences of various parameters on the control performance are explicitly studied.

5.2.1 Numerical Implementation

It is worth noting that the positive definite matrix $\boldsymbol{H}$ makes it a convex QP problem where the solution is a global minimum. The resulting QP problem is solved by the interior-point method due to its high convergence rate and ease of implementation. The implementation process is shown in the figure below, where the iterative optimization process is shifted forward with the constrained QP problem solved at each iteration step. Once the control increments $\boldsymbol{\Delta}\tilde{\boldsymbol{U}}_k$ are solved, the control input at the time instant k and the state at the time instant (k+1) are updated. It should be noted that the lengths of the predictive horizon N and control horizon N_c should be properly selected as they would directly affect the dimensions of matrices $\boldsymbol{\Gamma}$ and $\boldsymbol{G}$, and further indirectly determine the size of matrices $\boldsymbol{H}$ and $\boldsymbol{f}$. Therefore, a longer length

of N and N_c would increase computational efforts because all matrices must be updated at each time instant.

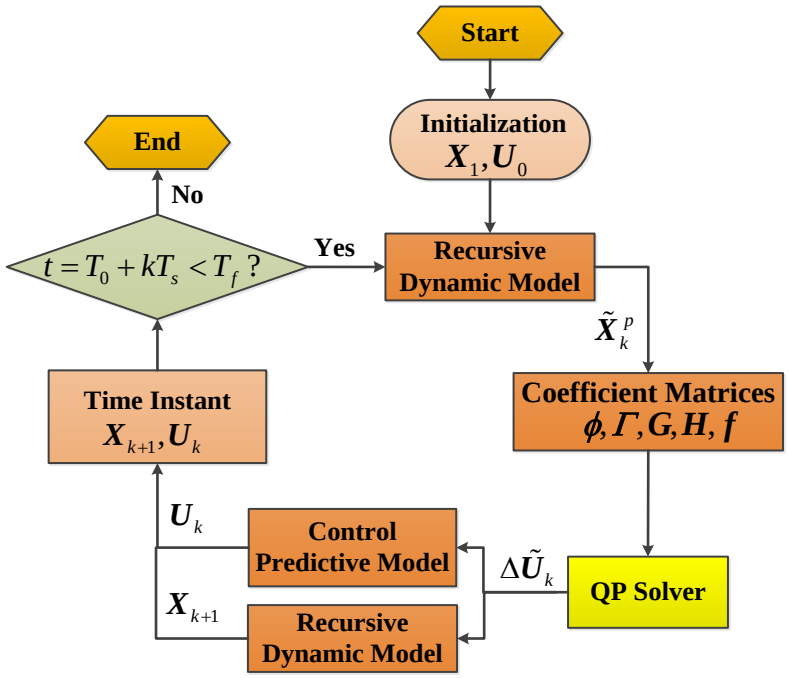

Figure 5.8 Flow chart of the receding horizon optimization strategy

5.2.2 Results and Discussion

The proposed NMPC algorithm is applied to the problem of ARPO with stable and spinning targets in an elliptical orbit. Assume the target is a cubic with a 0.1 *m* long docking axis mounted on one of its side surfaces. The dimension of the target is 1.8×1.8×1.8 *m*. Therefore, the distance from the target's CM to the docking port is 1 *m*. The masses of the target and chaser are 900 *kg* and 100 *kg*, respectively. The angles of the LOS constraint are defined as $\alpha = \beta = 30^\circ$ and the sampling time T_s is 0.1 *s*. The maximum control force is

restricted to 1 N and the orbital elements of the target are given in Table 5.5. If not specified otherwise, the triangular yellow region in the following figures represents the projection of the LOS constraint in the orbital plane.

Table 5.5 Orbital elements of the target

Parameters	Values
Eccentricity (e)	0.1
Semi-major axis (a), km	12,000
Inclination (i), deg	50°
Argument of perigee (ω), deg	30°
Right ascension of ascending node (Ω), deg	10°
Initial true anomaly (θ), deg	0°

5.2.2.1 Approach a Three-axis Stabilized Target

In this section, the in-plane and out-of-plane rendezvous with an attitude stable target in an elliptical orbit are studied.

1) In-Plane Rendezvous

Firstly, the proposed NMPC is examined by considering a simplified case where the chaser is approaching the target in the orbital plane. The initial position and velocity of the chaser with respect to the target are defined as $\{15\ m,\ 0\ m,\ 0\ m\}^T$ and $\{0.5\ m/s,\ 2\ m/s,\ 0\ m/s\}^T$, respectively. The corresponding weight matrices are defined as $\boldsymbol{Q} = diag(80,\ 80,\ 80,\ 80,\ 80,\ 80)$ and $\boldsymbol{P}$ =

diag(100, 100, 100). The simulation time is set 300 *s*. Furthermore, the problem is analyzed with the same weights by the classic state-dependent Riccati equation (SDRE) method as a benchmark. It should be noted that the cost functions in the SDRE and NMPC methods are different. The cost function in the SDRE is the weighted sum of state errors and total controls, while its counterpart in the NMPC is the weighted sum of state errors and control increments. The energy consumption is assessed by an energy index, $E(t) = \int_0^t \|\boldsymbol{U}\|^2 dt$, with the unit of $N^2 s$.

As for the controller design of autonomous rendezvous, generally speaking, the smaller the approaching velocity, the less stringent requirement for the control approach to achieve the predefined goal. Normally, the relative velocity is rather small when the chaser spacecraft is approaching the target in close range so as to avoid collision and guarantee safety. In the numerical simulations, however, the value of approaching velocity is assumed to be a bit bigger simply to verify the effectiveness of the control approach and its application in the ARPO. It is reasonable to infer that the controller would be capable to handle a slower approaching process if a faster approaching is managed properly.

To begin with, the influence of the control (N_c) and predictive (N) horizons on the accumulated control inputs ($\sum_{i=0}^{n-1} \|\boldsymbol{U}_i\|$), rendezvous time and

computational effort is investigated to examine the NMPC performance. Particularly, for every control horizon $N_c = \{1,3,5\}$, the accumulated control inputs, rendezvous time and computational effort are calculated at different predictive horizons $N = \{10,20,30,40,50,60,70\}$. It is worth noting that the rendezvous time is recorded when the distance between the chaser and the docking port is less than 0.1 *m*.

The analysis results are shown in Fig. 5.9, where the accumulated control inputs are shown in Fig. 5.9 (a), the rendezvous time in Fig. 5.9 (b) and the computational effort in Fig. 5.9 (c). As shown in Fig. 5.9 (a), the magnitude of the accumulated control inputs decreases as the number of predictive horizon *N* increases for all given N_c. The increase of *N* includes more predicted states in the QP, leading to improved control accuracy or less error in the states. Consequently, smaller control correction or control increment input is required. This is desirable in practical implementation as it consumes less fuel. After *N*> 40, the variation of accumulated control inputs is less than 5%, which indicates the NMPC is converged. However, it should be noted that the number of predictive horizon must be subject to the constraint of rendezvous time, which is specified by mission requirement. In addition to the convergence of predictive horizon *N*, it is also observed that the control prediction becomes more accurate as N_c increases for all given *N*. This is evident that the difference in accumulated control inputs is reduced monotonously as N_c increases from 1

to 5. Noticeably, the solution converges after $N_c = 3$.

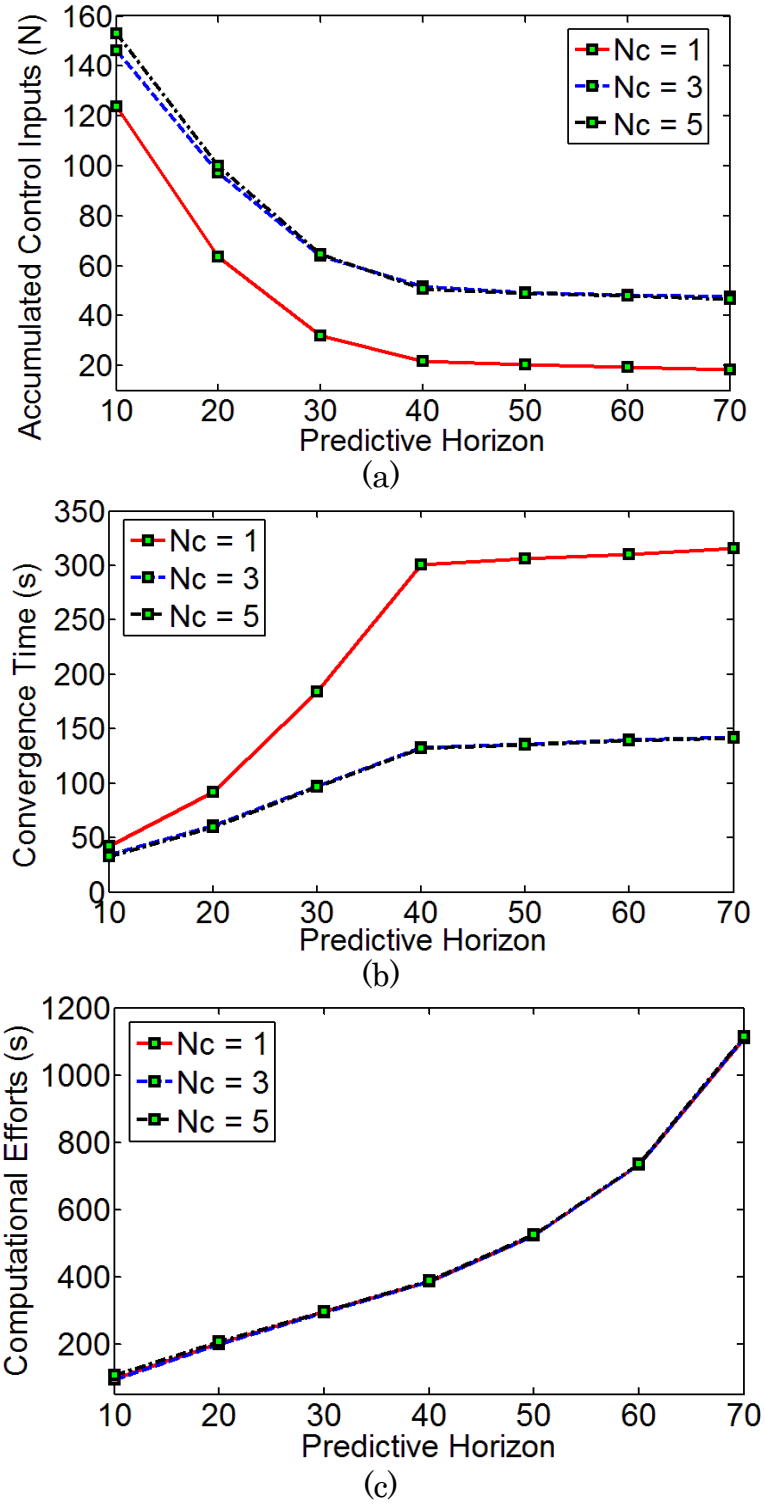

Figure 5.9 Influences of predictive and control horizons on (a) accumulated

control force, (b) rendezvous time and (c) computational efforts

Figure 5.9 (b) shows the dependence of rendezvous time on the numbers of predictive and control horizons. It can be seen the number of predictive horizon affects the rendezvous time, for instance, the rendezvous time reduces significantly from N_c = 1 to 3 for all given N. However, the solution converges after N_c = 3, the same as indicated in Fig. 5.9 (a). For all given N_c, the rendezvous time increases as the number of predictive horizon increases. This is in-line with the trend shown in Fig. 5.9 (a) for the accumulated control inputs, where the smaller control increment input leads to slower convergence rate.

Figure 5.9 (c) shows the computational effort in term of CPU time. Interestingly, the number of control horizon does not affect the CPU time very much and the difference diminishes as the number of predictive horizon increases. This is caused by the distinguished difference in the values of two horizons. For all given N_c, the CPU time increases as N increases as expected. This is mainly due to the fact that the larger predictive horizon N results in a longer sequence of predicted states $\boldsymbol{X}(k+j|k), j=1,2,\ldots,N$, and higher dimensions of the corresponding matrices $\boldsymbol{\phi}$, $\boldsymbol{\Gamma}$ and $\boldsymbol{G}$. Therefore, a longer CPU time is required to deal with the increased computational complexity.

The above analysis shows that the control parameters, the numbers of predictive and control horizons, affect the performance of the proposed NMPC

significantly. Even though a larger N_c speeds up the convergence of the states with slight increase in CPU time, it results in higher control inputs and correspondingly higher fuel consumption. From the engineering perspective, it is not desirable. Furthermore, a larger N results in the reduction of the accumulated control inputs and increase of the convergence (rendezvous) time, which is desirable for engineering implementation. However, it increases the CPU time, which will be challenging for the limited capacity of onboard computer. Therefore, $N_c = 1$ is selected for the following simulations and N is determined as a trade-off among the accumulated control inputs, rendezvous time and computational effort in each scenario.

Next, the results of approaching trajectories and time histories of relative distance with $N_c = 1$ and $N = 30$ by the SDRE and proposed NMPC are shown in Fig. 5.10. The approaching trajectories by both controllers reach the designated position as shown in Fig. 5.10 (a). The trajectory shows that the chaser spacecraft reaches the docking port in a straightforward manner. It is smooth and within the LOS cone without any overshoot as required. However, the trajectory by the SDRE is curved towards the docking port. Although it stays within the LOS cone for the most part of the trajectory, the overshoot occurs in the final docking stage, leading to an unsafe maneuver. This is because no path constraint, such as the LOS constraint in the NMPC, can be imposed by this classic SDRE controller.

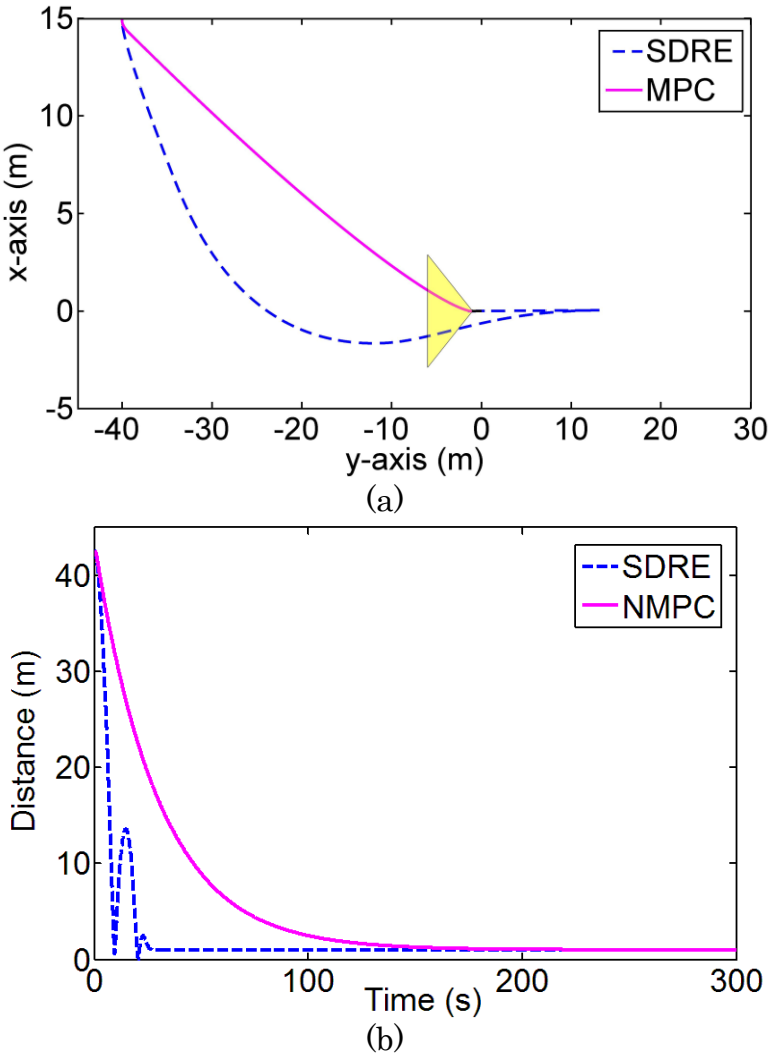

Figure 5.10 Comparisons of using SDRE and NMPC: (a) approaching trajectory and (b) relative distance

The difference of two trajectories is evident in the time histories of relative distance shown in Fig. 5.10 (b), where the NMPC is smoother and the SDRE shows some transient response due to overshoot. The different characters of two controllers can be attributed to the different cost functions. The NMPC penalizes the control increment inputs to adjust the control indirectly. This is designed to prevent the sudden movement of the chaser. In

contrast, the SDRE penalizes the total control inputs to adjust the control directly, which does not prevent the sudden change in control input.

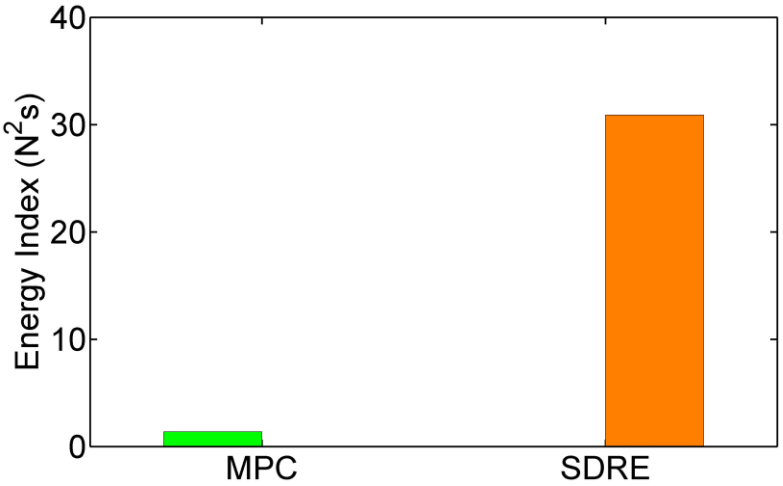

Figure 5.11 Energy consumption during the rendezvous process

Finally, the energy consumption by two controllers is shown in Fig. 5.11. The proposed NMPC consumes much less fuel than the SDRE does due to its smooth trajectory without overshoot that requires extra energy to correct the deviation.

2) Out-of-Plane Rendezvous

In this case, the case study is extended to the out-of-plane rendezvous in an elliptical orbit. Two rendezvous cases are considered with their initial rendezvous conditions of the chaser given in Table 5.6. Furthermore, the corresponding weight matrices in NMPC are $\boldsymbol{P}$ = *diag*(500, 500, 500) while $\boldsymbol{Q}$ = *diag*(1, 1, 1, 20, 40, 20) and *diag*(1, 1, 1, 40, 20, 20) for minus *y*- and *x*-axis directions, respectively. In addition, the control and predictive horizons are

given as $N_c = 1$ and $N = 20$ and the rendezvous process is set 300 *s*.

Table 5.6 Initial condition of rendezvous

Direction	Position (*m*)	Velocity (*m/s*)
Minus *y*-axis	[20, -60, 5]	[-0.5, 0.8, -0.1]
Minus *x*-axis	[-70, 15, 6]	[0.1, -0.2, -0.2]

Figure 5.12 illustrates 3D views of the optimized approaching trajectories of the chaser starting from the minus y- and x-axis with the LOS constraint and the projected views of trajectories in the orbital plane. It shows that the chaser first adjusts its path to the extension of the LOS cone smoothly, and then approaches the docking port to achieve a successful docking.

Figures 5.13 shows the time histories of the relative distance and control force in the approaching maneuver. The position of the chaser converges to the docking port after around 300 *s*, the constraint on the control force is satisfied at all time with the maximum control force less than 1 *N*. Thus, the NMPC controller satisfies our requirements.

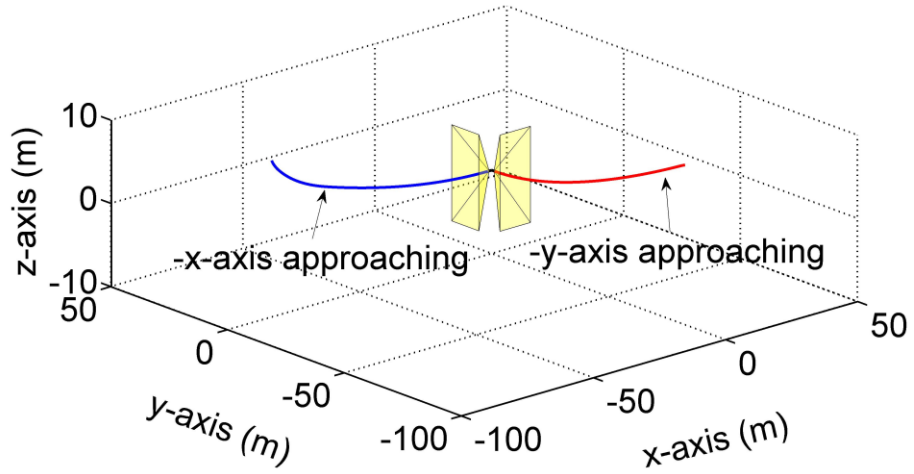

(a)

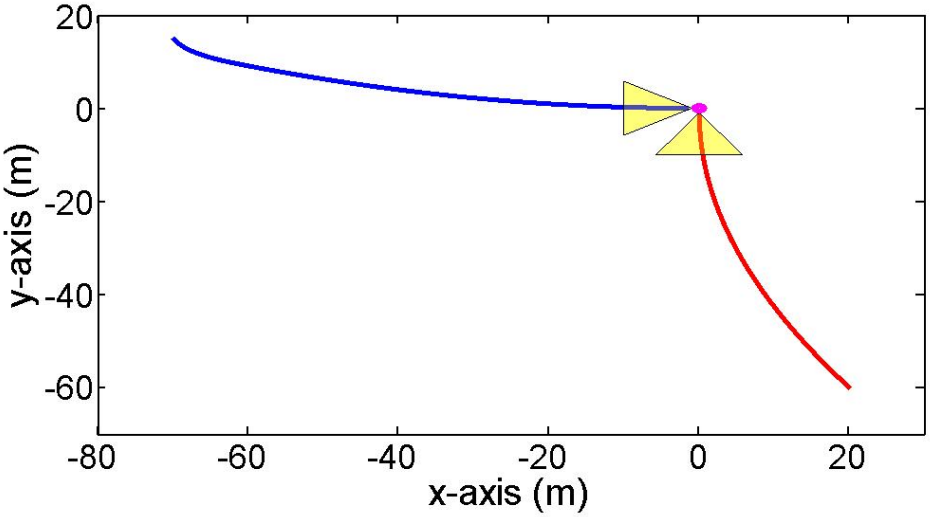

(b)

Figure 5.12 Approaching trajectories along minus x, y-axis directions: (a) 3D in space, (b) trajectory projection in orbital plane

To begin with, the influence of the control (N_c) and predictive (N) horizons on the accumulated control inputs ($\sum_{i=0}^{n-1}\|\boldsymbol{U}_i\|$), rendezvous time and computational effort is investigated to examine the NMPC performance. Particularly, for every control horizon $N_c = \{1,3,5\}$, the accumulated control

inputs, rendezvous time and computational effort are calculated at different predictive horizons $N = \{10, 20, 30, 40, 50, 60, 70\}$. It is worth noting that the rendezvous time is recorded when the distance between the chaser and the docking port is less than 0.1 *m*.

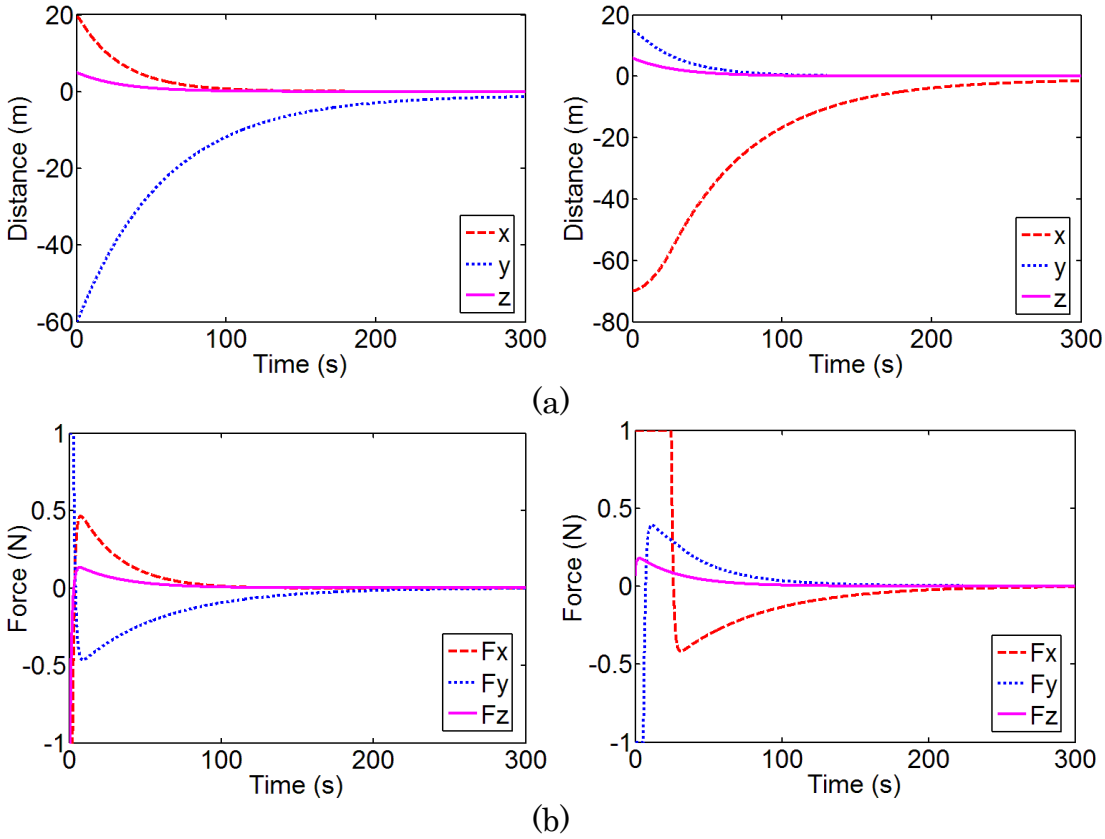

Figure 5.13 (a) Relative distance and (b) control force for rendezvous from minus y-axis (left) and minus x-axis (right).

As shown in Fig. 5.14 (a), the magnitude of the accumulated control inputs decreases as the number of predictive horizon N increases for all given N_c. The increase of N includes more predicted states in the QP, leading to improved control accuracy or less error in the states. Consequently, smaller control correction or control increment input is required. This is desirable in

practical implementation as it consumes less fuel. After $N > 40$, the variation of accumulated control inputs is less than 5%, which indicates the NMPC is converged. However, it should be noted that the number of predictive horizon must be subject to the constraint of rendezvous time, which is specified by mission requirement. In addition to the convergence of predictive horizon N, it is also observed that the control prediction becomes more accurate as N_c increases for all given N. This is evident that the difference in accumulated control inputs is reduced monotonously as N_c increases from 1 to 5. Noticeably, the solution converges after N_c = 3. However, the magnitude of the accumulated control inputs increases as N_c increases. This is because the assumption of $\Delta \boldsymbol{U}_{k+i} \neq 0 \quad (i = 0,1,\ldots,N_c - 1)$ and $\Delta \boldsymbol{U}_{k+i} \equiv 0 \quad (i = N_c, N_c + 1,\ldots,N-1)$, where the large N_c results in more non-zero control increment terms added to the total control input for the next time instant. From the practical perspective, the larger value of the accumulated control inputs implies more fuel consumption, which is undesirable.

Figure 5.14 (b) shows the dependence of rendezvous time on the numbers of predictive and control horizons. It can be seen the number of predictive horizon affects the rendezvous time, for instance, the rendezvous time reduces significantly from N_c = 1 to 3 for all given N. However, the solution converges after N_c = 3, the same as indicated in Fig. 5.14 (a). For all given N_c, the rendezvous time increases as the number of predictive horizon

increases. This is in-line with the trend shown in Fig. 5.14 (a) for the accumulated control inputs, where the smaller control increment input leads to slower convergence rate.

Figure 5.14 (c) shows the computational effort in term of CPU time. Interestingly, the number of control horizon does not affect the CPU time very much and the difference diminishes as the number of predictive horizon increases. This is mainly caused by the distinguished difference in the values of two horizons. For all given N_c, the CPU time increases as N increases as expected. This is mainly due to the fact that the larger predictive horizon N results in a longer sequence of predicted states $\boldsymbol{X}(k+j\,|\,k), j=1,2,\ldots,N$, and higher dimensions of the corresponding matrices $\boldsymbol{\phi}$, $\boldsymbol{\Gamma}$ and $\boldsymbol{G}$. Therefore, a longer CPU time is required to deal with the increased computational complexity.

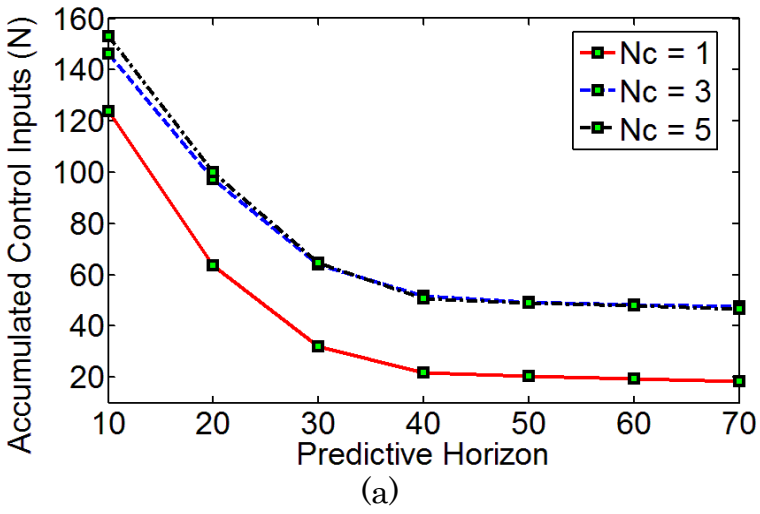

(a)

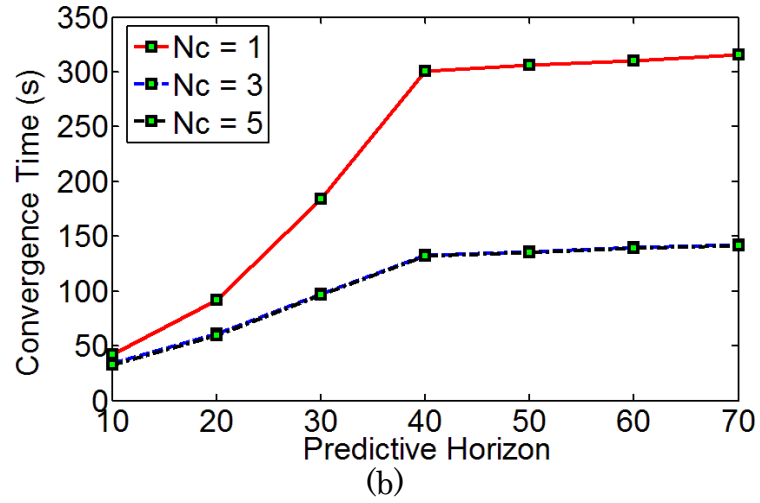

(b)

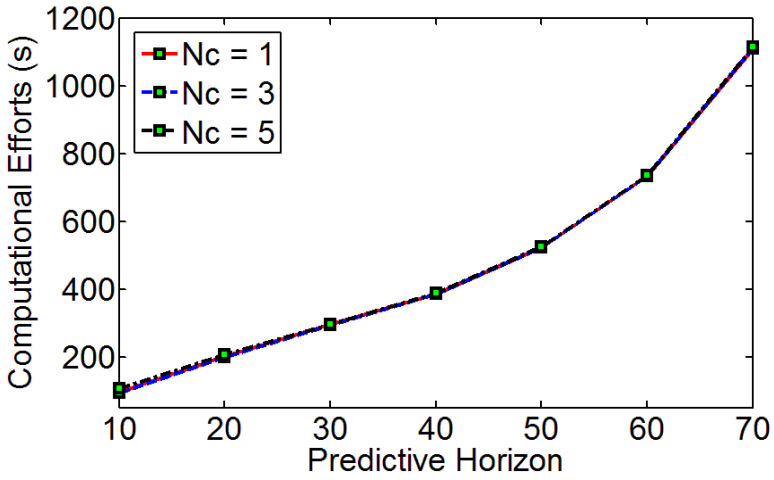

(c)

Figure 5.14 Influences of predictive and control horizons on (a) accumulated control force, (b) rendezvous time and (c) computational efforts

The above analysis shows that the control parameters, the numbers of predictive and control horizons, affect the performance of the proposed NMPC significantly. Even though a larger N_c speeds up the convergence of the states with slight increase in CPU time, it results in higher control inputs and correspondingly higher fuel consumption. From the engineering perspective, it is not desirable. Furthermore, a larger N results in the reduction of the accumulated control inputs and increase of the convergence (rendezvous) time,

which is desirable for engineering implementation. However, it increases the CPU time, which will be challenging for the limited capacity of onboard computer. Therefore, $N_c = 1$ is selected for the following simulations and N is determined as a trade-off among the accumulated control inputs, rendezvous time and computational effort in each scenario.

5.2.2.2 Rendezvous with a Spinning Target

After the case of an attitude stable target, the ability of the proposed NMPC in dealing with a spinning target is demonstrated. Assume the chaser and target are in the same orbital plane. The docking axis of the target is assumed initially in the minus y-axis direction and spinning at the velocity $\boldsymbol{\omega}_{s0} = \{0, 0, -\omega_0\}^T$ with $\omega_0 = 3°/s$. The chaser is assumed initially trailing behind the target by -10 m in the minus y-axis direction and stationary with respect to the target. Three initial positions of the chaser in the radial direction are considered, such as, -5 m, 0 m and 5 m, in the LVLH frame, respectively. The corresponding weight matrices are $\boldsymbol{P}$ = *diag*(1, 1, 1) and $\boldsymbol{Q}$ = *diag*(80, 80, 80, 80, 80, 80). In addition, the numbers of control and predictive horizons are set as $N_c = 1$ and $N = 30$, respectively. The simulation time is set to 30 s.

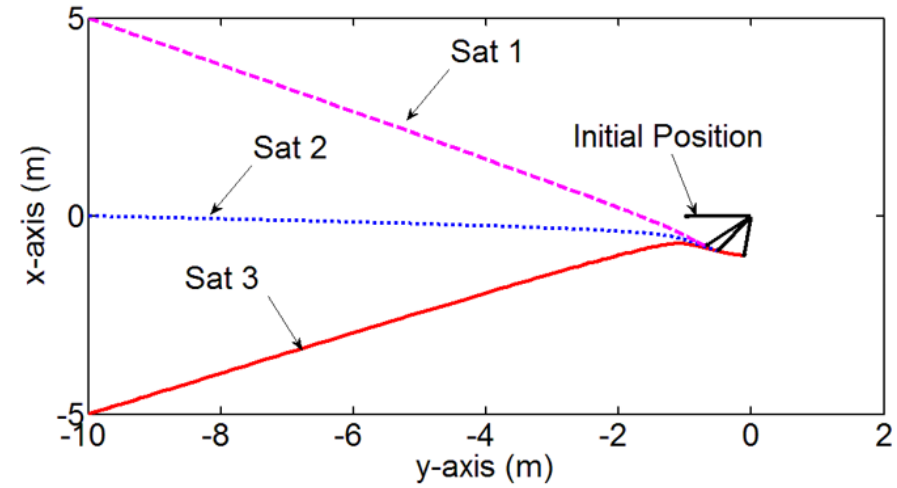

(a)

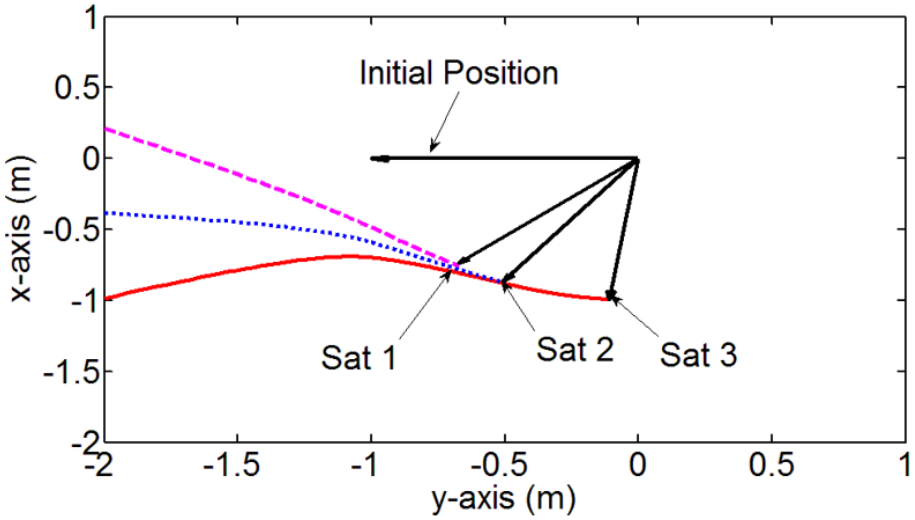

(b)

Figure 5.15 Y-axis approaching trajectories in the orbital plane from various initial positions (a) and zoomed-in trajectories (b) when the target is spinning at $\omega_o = 3^{\circ}/s$

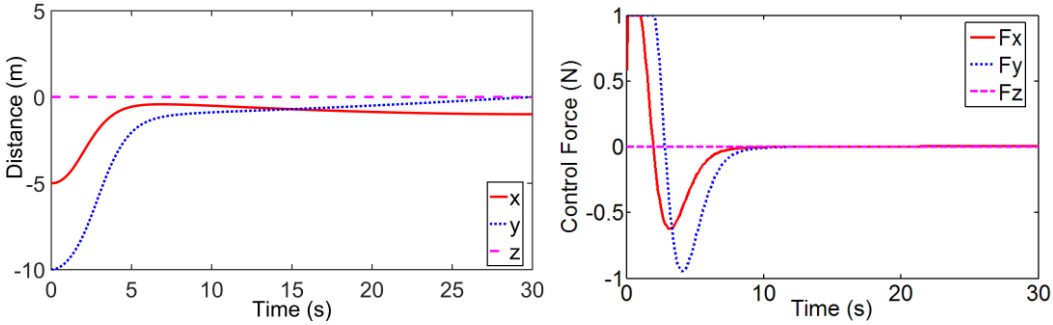

(a)

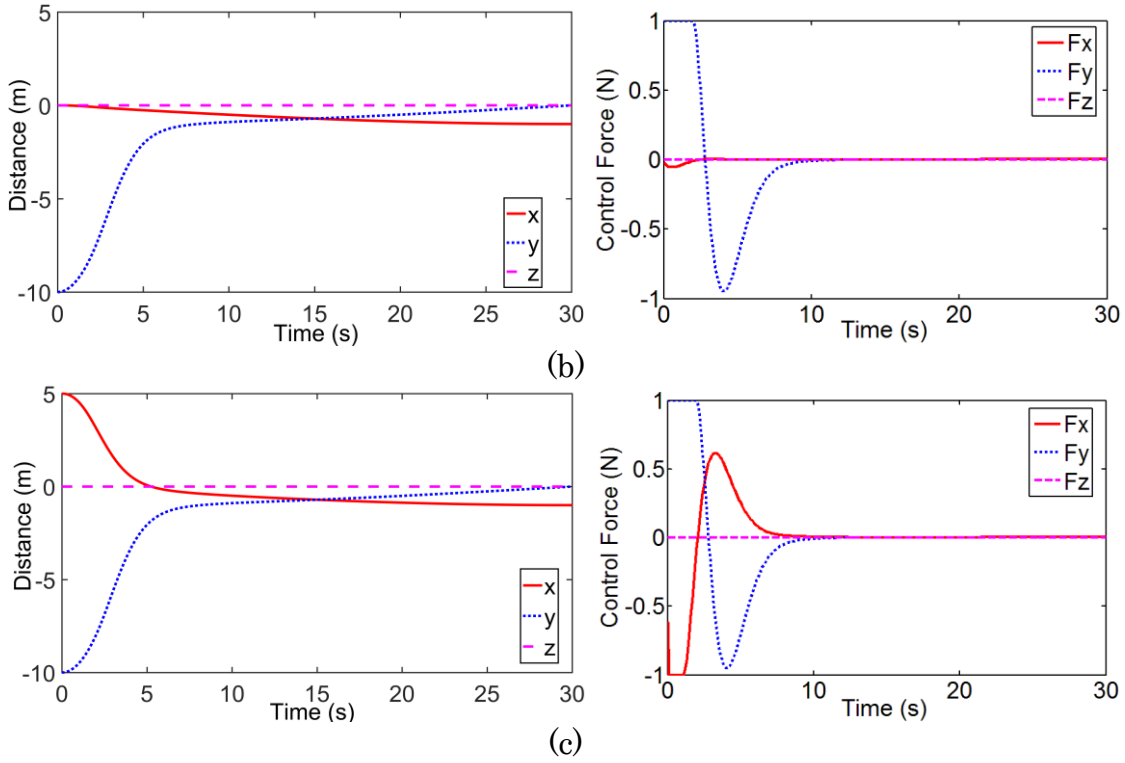

Figure 5.16 Relative distance (left) and control force (right) for (a) sat 1, (b) sat 2 and (c) sat 3

The along-track approach trajectories, time histories of relative distance and control force are shown in Figs. 5.15 and 5.16. It can be seen that the proposed control scheme successfully controls the chaser completing rendezvous with the spinning docking axis in all cases. The chaser starting from three different positions reaches the docking port at 17 *s*, 20 *s* and 28 *s*, respectively.

5.2.3 Conclusion

This section investigates the control problem of spacecraft autonomous rendezvous and proximity operation of a spacecraft in an elliptical orbit by the

model predictive control. Numerical simulations are conducted in two different scenarios: rendezvous with a stable target and a spinning target, respectively. First, the effects of different control and predictive horizons are investigated to achieve better control performance in terms of accumulated control inputs, rendezvous time and computational effort. It is found that the solution converges after the number of control horizon is greater than three with finite increase of computational efforts. However, it results in higher accumulated control inputs, which is proportional to fuel consumption. Therefore, it is recommended to use lower number of control horizon (Nc = 1). Furthermore, the number of predictive horizon is found to affect accumulated control inputs, rendezvous time and computational efforts. Consequently, the number of predictive horizon N should be selected as a trade-off between control performance and mission requirements. Next, the effectiveness of the proposed control strategy is demonstrated by comparing with the standard state-dependent Riccati equation control algorithm using the same set of initial conditions and parameters. The results show that the newly proposed control strategy achieves better fuel efficiency by enforcing the smoothness of control input (no overshoot in final docking stage).

5.3 Line-of-Sight Based Autonomous Rendezvous

In the active debris removal missions, autonomous rendezvous with a

target in near-field generally employs laser imaging detection and ranging system and advance video guidance system for relative navigation. The state feedback with measurement uncertainties is introduced to form a closed-loop optimal control problem by integration of receding horizon strategy. This section investigates the trajectory planning and control of autonomous spacecraft rendezvous with a passive non-cooperative target with LOS dynamics. The control problem is formulated in terms of LOS azimuth angles with respect to the target.

The aforementioned approaches were based on the LVLH formulation, including the LVLH based NMPC approach. As a result, the relative navigation information has to be transformed from the LOS frame to the LVLH frame. The extra transformation between the LOS and LVLH frames complicates the derivation of guidance control and adds extra computational efforts for onboard computers. To reduce the computational requirement for the onboard computers, LOS based autonomous rendezvous were developed to employ the navigation directly.

No attempt has been made to the LOS based NMPC in autonomous spacecraft rendezvous, to the best of our knowledge. The numerical results show that the newly proposed line-of-sight nonlinear model predictive control scheme is able to effectively generate optimized approach trajectories with satisfactory control accuracy and the proposed method is insensitive to the

measurement uncertainties.

5.3.1 Numerical Implementation

Finally, measurement errors ($\delta\rho, \delta\theta$) from navigation sensing systems are inevitable, such as the optical artifacts (e.g., glints, glares, saturations, hot pixels) in the sensors' fields of view, which may result in sudden changes in control input. Theoretically, the sudden changes in control input could be indirectly rejected by smoothing the control input increment, which is the objective of the proposed optimal control cost function. Thus, the effectiveness of disturbance rejection will be demonstrated by adding the errors $\delta \boldsymbol{X} = [\delta\rho, \delta\theta, 0, 0]^T$ to the control input $\boldsymbol{U}_k$ and state $\boldsymbol{X}_{k+1}$ at the beginning of each time instant. The navigation errors are assumed as white noise with zero mean. The problem is then solved by the interior-point method due to its high convergence rate and the ease of implementation and the computational diagram of the close-loop control strategy is given below.

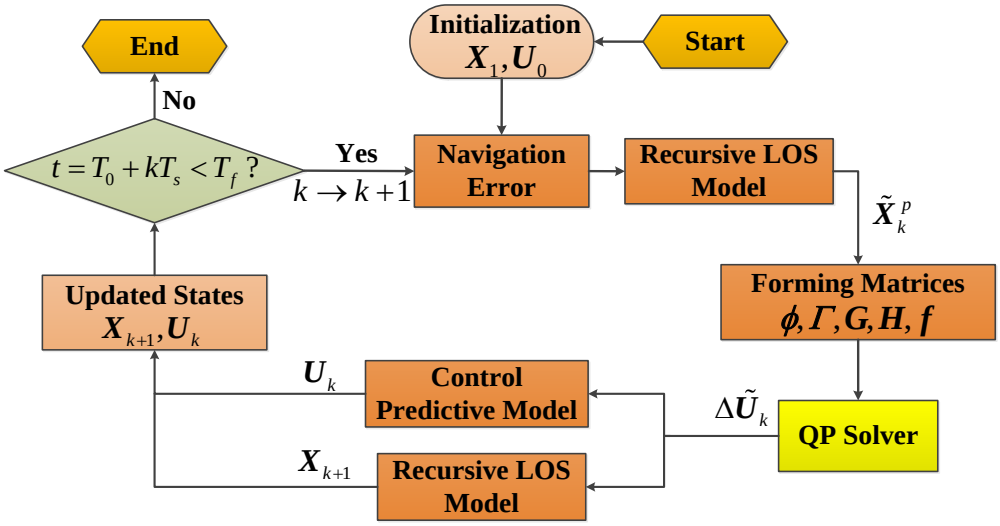

Figure 5.17 Block diagram of LOS based NMPC

5.3.2 Rendezvous Strategy

The rendezvous of the chaser with the target is achieved by a judicious two-phased strategy to ensure the final azimuth direction at rendezvous to be satisfied precisely. In the first phase, the control task is to maneuver the chaser from its initial position to an intermediate point in the vicinity of the target for collision avoidance, such that, $\rho > \rho_S$ and ρ_S is the safety distance from the target determined by the mission requirement. At the same time, the chaser must adjust its azimuth angle from the initial condition θ_0 to the desired value, $\theta = \theta_d$. In the second phase, the control task is to approach the target in a straight trajectory along the desired azimuth angle until $\rho = \rho_d$ to accomplish the rendezvous mission. In the current work, it is assumed that $\rho_S = 20$ m, θ_0 and θ_d are determined by the particular rendezvous scenarios as specified in the following numerical examples.

The above two-phased rendezvous strategy is achieved by the properly selected weight matrices, seen in Table 5.7. Assume the chaser's ability to maneuver in LOS range and angle directions is equally important in the rendezvous mission. This leads to the same penalties on the two control input (F_ρ, F_θ) in the weight matrix $\boldsymbol{P}$. The determination of weight matrix $\boldsymbol{Q}$ is heavily dependent on the rendezvous strategy. The control task in the first phase requires the chaser to aim the target in the required azimuth angle with a safe distance away. In this phase, the control accuracy for the azimuth angle is less important when the chaser is far away from the target. Accordingly, the penalty on the azimuth angle θ is set much larger than that on the LOS range ρ in this phase. In the second phase, it is critical to maintain a smooth trajectory in the proximity operation. Thus, the penalty for the third state (the approaching speed) is designed to slow down the relative velocity of the chaser for a safe approach. The last diagonal element in the weight matrix $\boldsymbol{Q}$ is the penalty for the fourth state - azimuth angular rate and is designed as state dependent, $1/\rho$, instead of constant. Different from other three penalties, this penalty weight increases dramatically as the chaser approaches the target. Thus, the azimuth angular rate is reduced quickly to avoid the chattering of approaching trajectory because a stable azimuth angle at the final approach is mission critical. Again, it should be noted that the LOS range ρ does not decrease to zero in real situation even when the rendezvous is completed. This

is because the LOS frame is centered at the CM of the target and there is a minimum value of ρ measured from the CM to external surface of the target.

Table 5.7 Parameters of weight matrices

Parameter	Value
State weight matrix	$Q = diag(50, 5000, 1000, 1/\rho)$
Control weight matrix	$P = diag(100, 100)$

5.3.3 Results and Discussion

The advantages of the proposed LOS NMPC in the spacecraft rendezvous are demonstrated by dynamic simulation of two rendezvous scenarios. The rendezvous conditions are listed in Table 5.8. The chaser is assumed to navigate by optical sensing system with direct measurement of the range and azimuth angle to the target. The sensor uncertainties, listed in the following table, are taken as a disturbance to the state, where σ_ρ and σ_θ are the standard deviations of the Gaussian distributions in terms of LOS range ρ and the azimuth angle θ, respectively.

The target is assumed moving in an elliptic orbit with a semi-major axis of 10,000 *km* and a true anomaly of 0°. The initial position of the target is assumed at perigee with an initial relative distance between the chaser and the target spacecraft of 80 *m*. To explore the application limit of the proposed approach, the eccentricity of 0.3 is used in the case studies.

Table 5.8 Rendezvous conditions

Parameters	Case 1		Case 2	
	Initial state	Desired state	Initial state	Desired state
ρ , m	80	1	80	1
θ , °	0	0, 90, 180, 270	0, –90, –180, –270	–90
$\dot{\rho}$, m/s	0	0	0	0
$\dot{\theta}$, $°/s$	0	0	0	0

The predictive horizon and control horizons are defined as $N = 10$ and $N_c = 1$. The mass of the chaser is assumed as 500 kg and the maximum available control thrust is limited to $U^{max} = 1$ N. The simulation duration is set to 600 s and the sampling time is $T_s = 0.1$ s. Note that the simulation results are shown in the LOS frame and the relative states are transformed to the orbital frame to show the approaching trajectory.

Table 5.9 Rendezvous navigation sensor uncertainties

Measurands	Standard deviation (σ)
LOS Range (ρ), cm	1.518
Azimuth angle (θ), °	0.002787

5.3.2.1 Approach Target in Different Directions

In this case, the coplanar rendezvous with the target from various directions is studied. At $t = 0$, the chaser is assumed to running in the same orbit as the target, but 80 m ahead with 0° azimuth angle. The control objective

is to approach the target along x_0-axis and y_0-axis directions by controlling the azimuth angle θ equal to 0°, 90°, 180° and 270°, respectively. For the purpose of collision avoidance and subsequent proximity operations, the chaser is required to stop at 1 *m* away from the target in all directions at the end of approach.

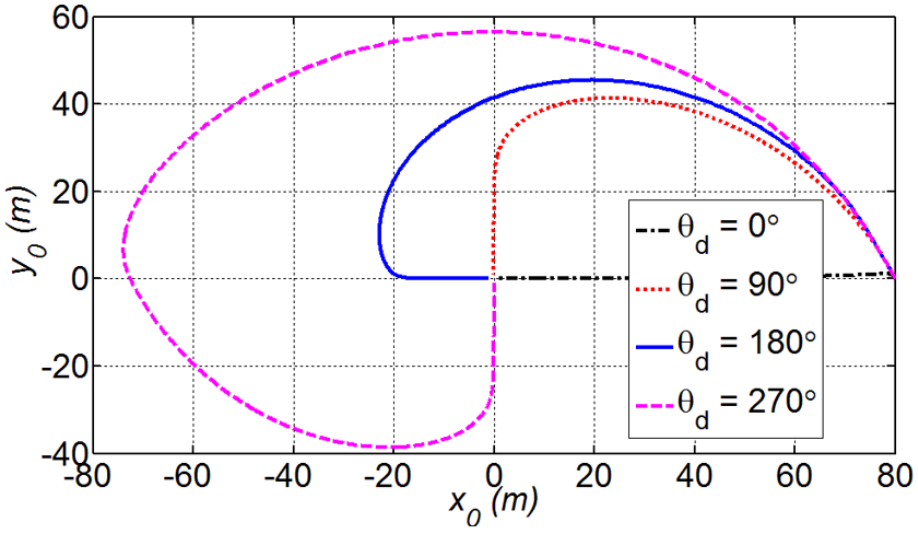

Figure 5.18 In-plane approaching trajectories for Case 1

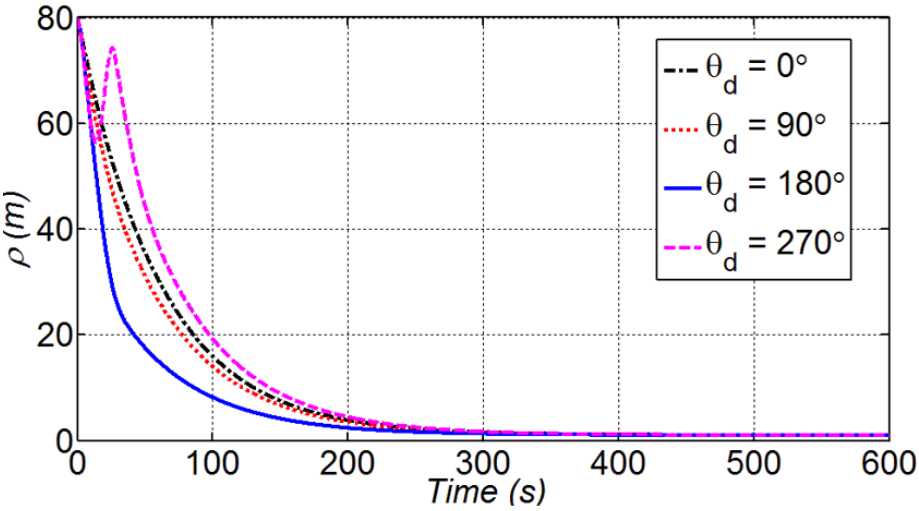

(a)

(b)

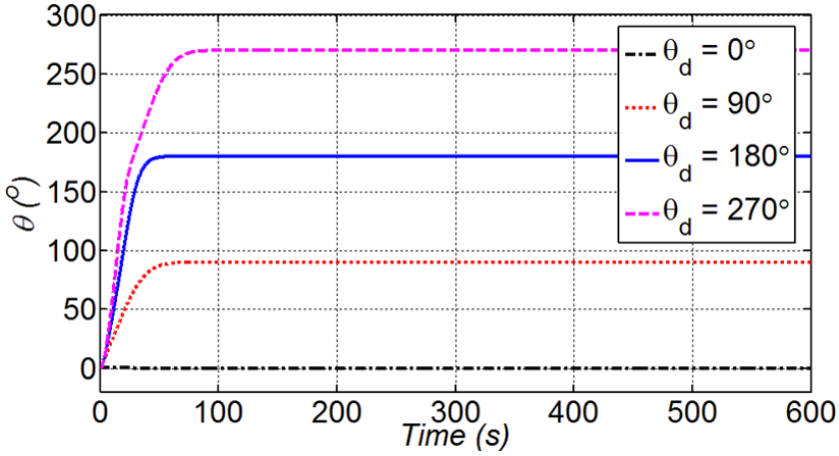

(c)

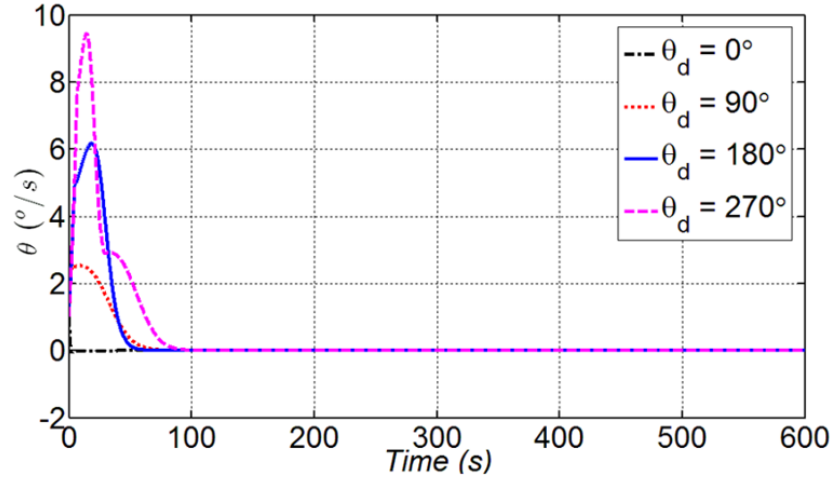

(d)

Figure 5.19 Case 1: (a) LOS range (b) relative velocity (c) azimuth angle and (d) azimuth angle rate

Figure 5.18 shows the coplanar approaching trajectories in the orbital frame along x_0-axis and y_0-axis directions, respectively. The chaser maneuvers around the target first to align the azimuth angle to the desired ones and then approaches to the desired position nearly in a straight line in the final stage as required, leading to a successful rendezvous.

Next, Fig. 5.19 displays the time histories of the LOS range, relative

velocity, azimuth angle and azimuth angle rate, respectively. Since the penalty term $1/\rho$ is relatively small at the beginning, the control on the azimuth angle rate is weak and the angle approaches to the desired value at a high rate initially. As the LOS range reduces and the penalty term $1/\rho$ increases, the azimuth angle rate is reduced, and the change of azimuth is flattened. As a result, the chaser adjusts its trajectory with respect to the target first and then approaches in a straight line. This approaching mode is widely adopted in space rendezvous missions to avoid collision with the target. The azimuth angle reaches its desired value at 100 *s* while the chaser reaches its final position at 600 *s*. The proposed control scheme yields smooth trajectories in all cases. It shows there is nearly no overshoot in the time histories of the LOS range and the azimuth angle.

To further demonstrate the effectiveness of the proposed control law, the control force profiles in the LOS range and azimuth angle channels are plotted in Fig. 5.20. It is interesting to note that the control force F_ρ in the LOS range channel reaches its maximum output magnitude, –1 *N*, in the first tens of seconds, see Fig. 5.20 (a), in order to quickly decrease the LOS range to reduce the rendezvous time.

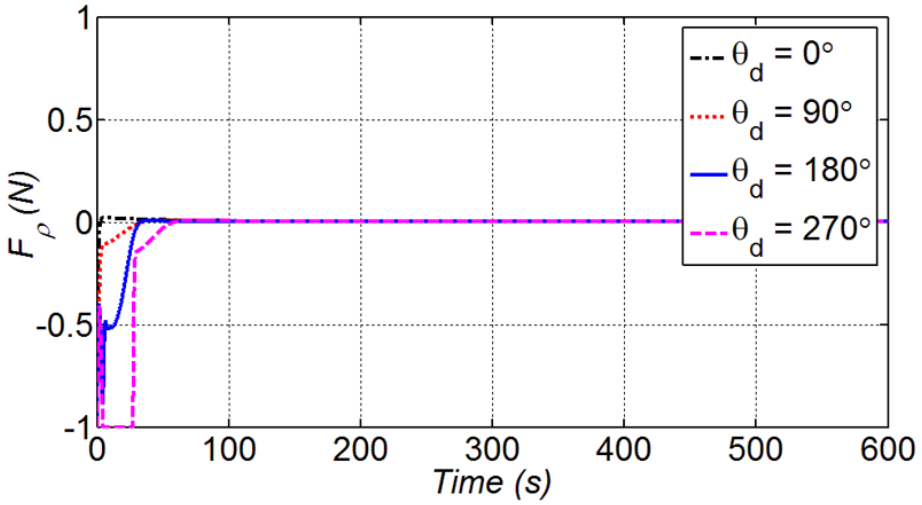

(a)

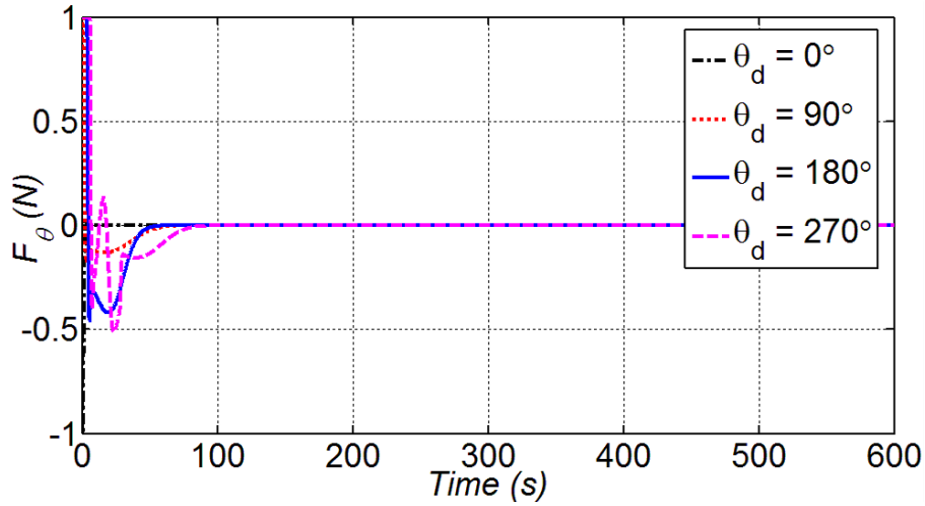

(b)

Figure 5.20 Control input: (a) LOS range and (b) azimuth angle

The negative symbol means the corresponding thrust is against the motion. The control force F_θ in the azimuth angle channel converges to zero at around 100 s after the azimuth angle reaches its desired value, see Fig. 5.20 (b), reflecting the effectiveness of the proposed two-phased rendezvous strategy. Furthermore, the chattering in the control force profiles is very small, which indicates that the proposed control law is effective in rejecting the

measurement uncertainties to reach the desired values of the LOS range and azimuth angle smoothly.

5.3.2.2 Approach Target from Different Initial Azimuth Angles

In this case, the coplanar rendezvous with the target is studied by assuming the chaser starting from different initial azimuth angles but with the same distance, 80 *m*, from the target. The control objective is to drive the chaser approaching the target in the $-y_0$-axis direction from 4 different initial azimuth angles: 0°, –90°, –180° and –270°, respectively. Similar to Case 1, the chaser is required to stop at 1 *m* away from the target in the $-y_0$-axis direction at the end of rendezvous for subsequent proximity operations.

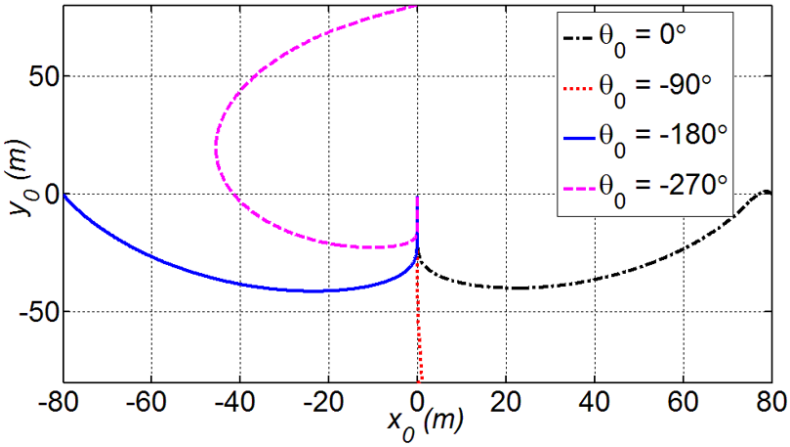

Figure 5.21 In-plane approaching trajectories for Case 2

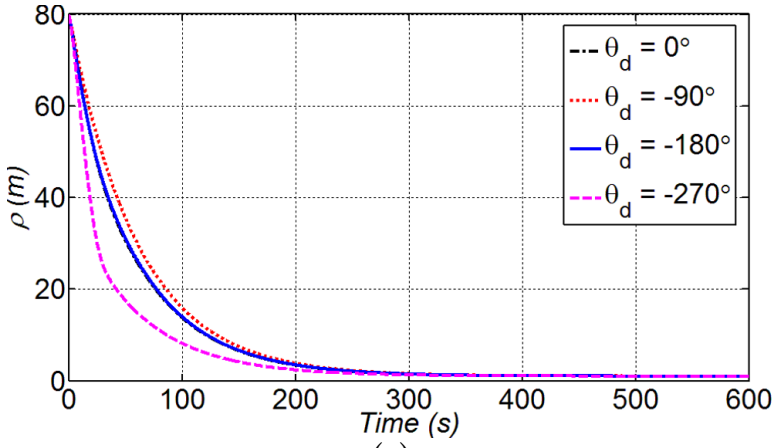
80
60
40
20
0
ρ (m)
0
100
200
300
400
500
600
Time (s)
θd = 0°
θd = -90°
θd = -180°
θd = -270°

(a)

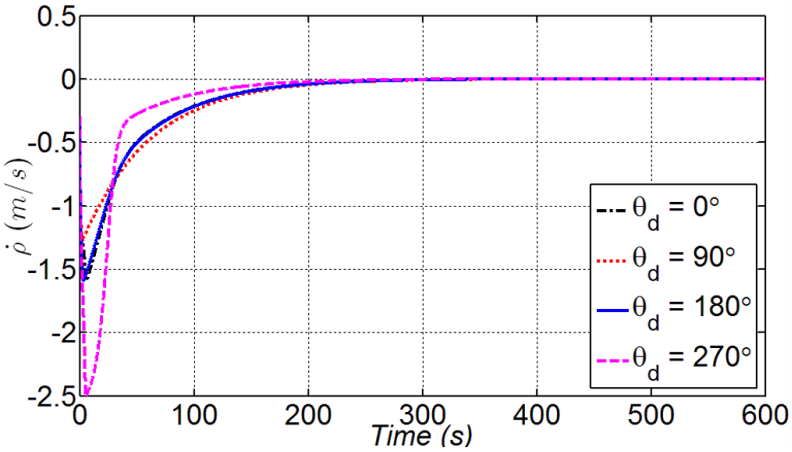
0.5
0
-0.5
-1
-1.5
-2
-2.5
ρ̇ (m/s)
0
100
200
300
400
500
600
Time (s)
θd = 0°
θd = 90°
θd = 180°
θd = 270°

(b)

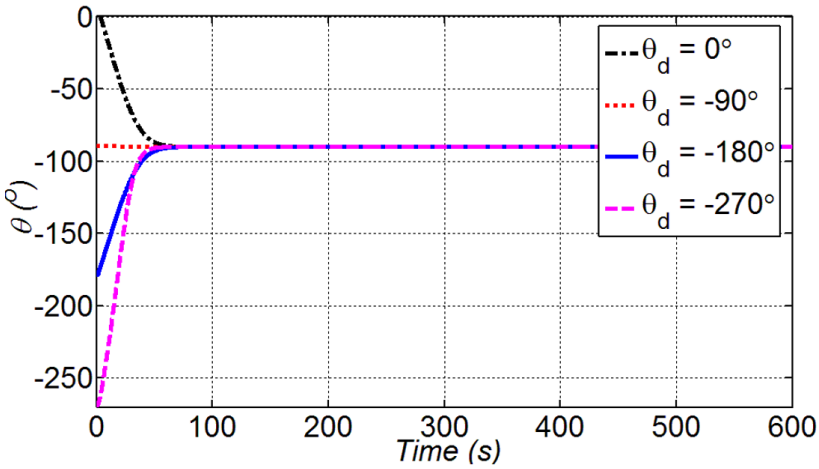
0
-50
-100
-150
-200
-250
θ (°)
0
100
200
300
400
500
600
Time (s)
θd = 0°
θd = -90°
θd = -180°
θd = -270°

(c)

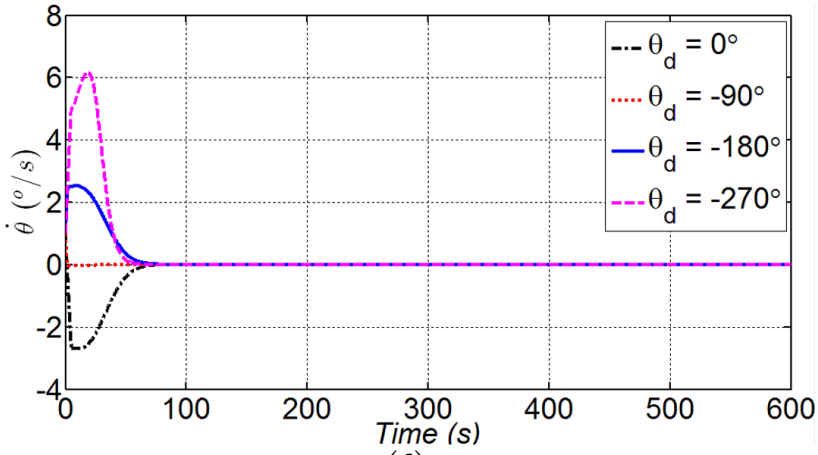

(d)

Figure 5.22 Case 2: (a) LOS range (b) relative velocity (c) azimuth angle and (d) azimuth angle rate

Figure 5.21 plots the rendezvous trajectories in the orbital frame. In all cases, the chaser successfully maneuvers to the vicinity of the target in the $-y_0$-axis direction first and then decreases the LOS range to the designated position in a straight line as required. Figure 5.22 shows the responses of the LOS range, relative velocity, azimuth angle and azimuth angle rate, respectively. Similarly, the azimuth angle rate changes quickly in the first 70 *s* since the chaser is far away from the target and the penalty term $1/\rho$ is relatively small. As the chaser getting closer to the target, the penalty $1/\rho$ increases hyperbolically. Accordingly, the azimuth angle rate approaches zero quickly which implies the azimuth angle reaches its desired value. The chaser adjusts its orientation with respect to the target prior to approach a straight trajectory in the final approach as per the rendezvous strategy. The trajectories are smooth as required.

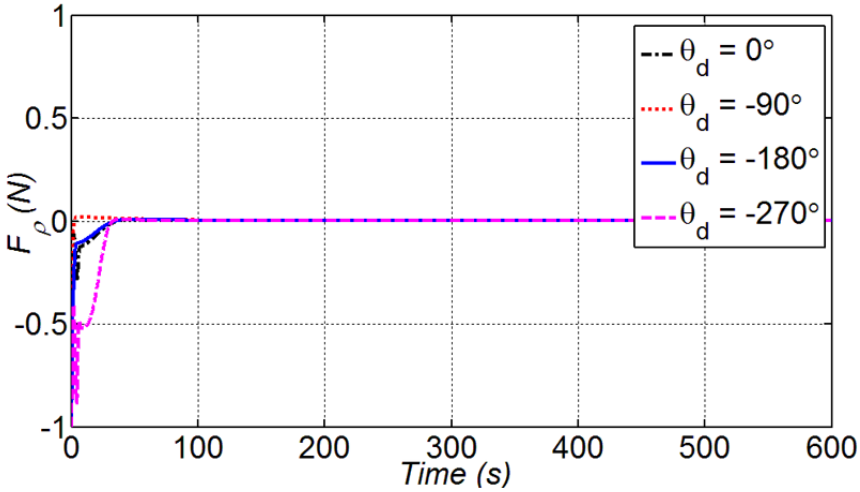

(a)

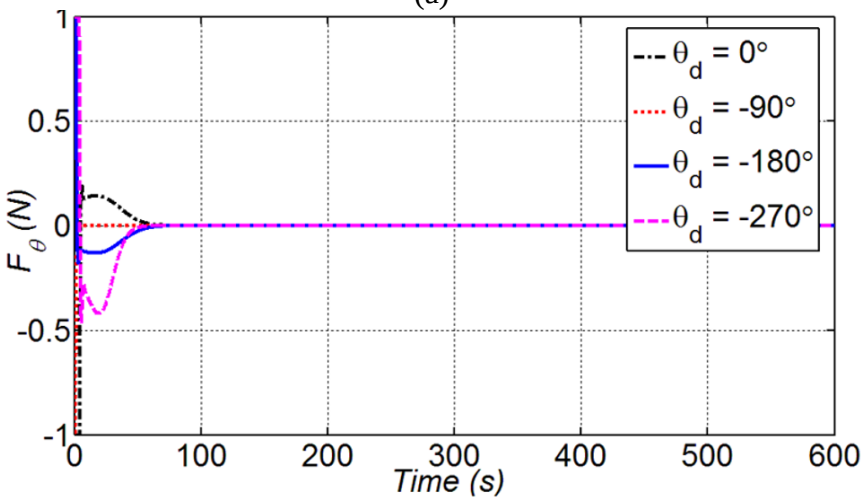

(b)

Figure 5.23 Control input: (a) LOS range and (b) azimuth angle

Finally, Fig. 5.23 plots the control forces in the LOS range and azimuth angle channels. It should be noted that the direct outputs of the relative navigation system are the LOS range and the azimuth angle. Our comparison did not include the time delay due to the transformation of navigation information between the LOS and orbital frames, which depends on individual converter and circuitry. Therefore, the integrated relative navigation and the control system under the LOS frame is advantageous theoretically in saving

computational efforts and opens the possibility to other savings by eliminating the conversion circuitry.

5.3.4 Conclusion

This section develops a LOS based NMPC for the coplanar autonomous rendezvous with non-cooperative targets. The LOS formulation simplifies the equations of relative dynamics of spacecraft using the relative navigation information from the measurement directly. The NMPC model is derived into a state dependent representation and the control is optimized for the control error and control smoothness simultaneously to achieve a smooth transient response. Numerical simulations demonstrate the newly proposed method is effective and capable of achieving the control objective and it is insensitive to navigation measurement errors.

5.4 Post-grasping Attitude Control of Compound Spacecraft

In this section, a new scheme of attitude control with inertial parameter identification is proposed based on the RLS and the NMPC to achieve an optimal post-capture attitude control of the combined spacecraft with bounded thrust, while identifying the inertia parameters simultaneously.

The proposed scheme computes control torques at each sampling instant based on the estimated inertial parameters until the rest-to-rest attitude maneuver task is completed with the inertial parameters successfully

identified. It also provides a closed-loop optimization strategy to identify the unknown inertial parameters via the model predictive control by minimizing both control error and roughness for a smooth attitude maneuvering trajectory. Numerical results show that the newly proposed scheme is able to effectively estimate the inertia parameters and maneuver the attitude of the combined spacecraft simultaneously.

5.4.1 Numerical Implementation

The block diagram for the numerical implementation of the newly developed algorithm is shown as below. In particular, the initial guess of the inertial vector $\hat{\boldsymbol{J}}_0$ together with the initial conditions of state and control vectors $(\boldsymbol{X}_1, \boldsymbol{U}_0)$ are given as inputs to the attitude dynamics. It is noted that the estimated inertia is applied here since the true inertial parameters are unknown. Upon formation of the matrices, the solution $\Delta\tilde{\boldsymbol{U}}_k$ is obtained after solving a QP problem. Then, the control input $\boldsymbol{U}_k$ is used to calculate the next state vector $\boldsymbol{X}_{k+1}$ based on the attitude dynamics. In the meantime, the angular velocity $\boldsymbol{\omega}_{k+1}$ is measured to form the observation matrix $\boldsymbol{H}_{k+1}$. By using the RLS algorithm, the inertial vector $\hat{\boldsymbol{J}}_{k+1}$ and the covariance matrix $\boldsymbol{P}'_{k+1}$ are updated to time instant $(k+1)$ with their current values. In this way, the RLS based inertial parameter identification is integrated to the NMPC to estimate

the inertial parameters and the estimates are updated at every time instant during the attitude control.

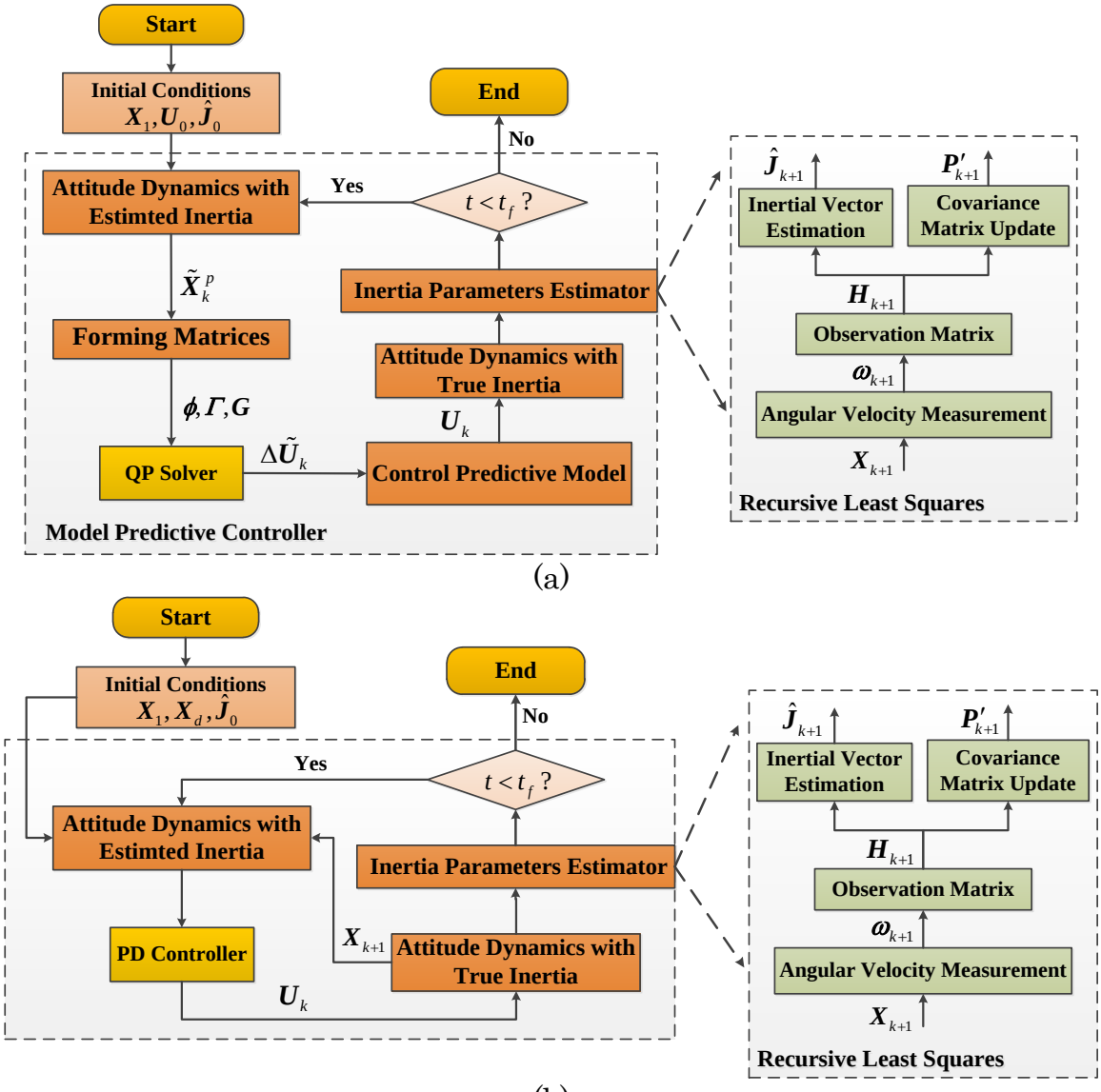

Figure 5.24 Block diagram of RLS parameter identification with NMPC (a) and PD controllers (b)

5.4.2 Results and Discussion

The performance of the proposed inertial parameter identification for the post-capture spacecraft attitude control is demonstrated by numerical

simulation. The control objective is to drive the attitude of the combined spacecraft from its initially disturbed orientation Θ_0 to the desired orientation Θ_d where the inertial parameters are unknown a priori. Since this is a rest-to-rest attitude maneuver, the initial and desired angular velocities must be zero, such that, $\boldsymbol{\omega}_0 = \boldsymbol{\omega}_d = 0$. The initial Euler angles (roll, pitch and yaw) are assumed as $\phi_0 = 1^\circ$, $\theta_0 = 2^\circ$, $\psi_0 = 3^\circ$ and their desired states are $\phi_d = 6^\circ$, $\theta_d = -7^\circ$, $\psi_d = 8^\circ$, respectively. Furthermore, assume the true inertia vector of the combined spacecraft is $\bar{\boldsymbol{J}} = \{30, 40, 50, 5, 4, 3\}^T$ $kg \cdot m^2$, the initial guess is $\hat{\boldsymbol{J}}_0 = \{100, 75, 90, 1, 5, 5\}^T$ $kg \cdot m^2$, and the inertia matrix of the reaction wheels is $\boldsymbol{J}_r = diag\{5, 5, 5\}^T$ $kg \cdot m^2$. The predictive horizon and control horizons in the NMPC are defined as N = 30 and N_c = 1, and the values of the weight matrices are listed in Table 5.10. To compare the control result, the NMPC with bounded torque and PD controller are both applied to generate control torque during the attitude maneuvering process under the identical initial conditions. The maximum magnitude of the control torque output is 5 Nm, and the control gains in the PD controller are Kp = -8 and Kd = -17. Finally, the simulation time is set to 150 s and the sampling time step is T_s = 0.1 s.

Table 5.10 Initial conditions

Parameters	Value

State weight matrix	$Q = diag(1000, 1000, 1000, 10, 10, 10)$
Control weight matrix	$P = diag(1,1,1)$
Covariance matrix	$\boldsymbol{P}_0' = 10^2 \cdot diag(1,\ 1,\ 1,\ 1,\ 1,\ 1)$
Weight matrix	$\boldsymbol{W} = 10^5 \cdot diag(1,\ 1,\ 1)$

The simulation results of inertial identification of six inertial parameters $\left\{J_{xx}, J_{yy}, J_{zz}, J_{xy}, J_{xz}, J_{yz}\right\}$ under the case of unbounded torque are shown in the following figures. The initial guess of inertial parameters $\hat{\boldsymbol{J}}_0$ converges to the true values $\bar{\boldsymbol{J}}$ in both scenarios, and this indicates the recursive least square method is effective and efficient in inertial parameter identification. Seen from the comparative study listed above, it takes a bit longer time for the identification curves to converge using the NMPC controller, this is because NMPC tries to minimize the control error between the actual state and the desired state while minimizing the control increment, this leads to a relatively slow change to the control output.

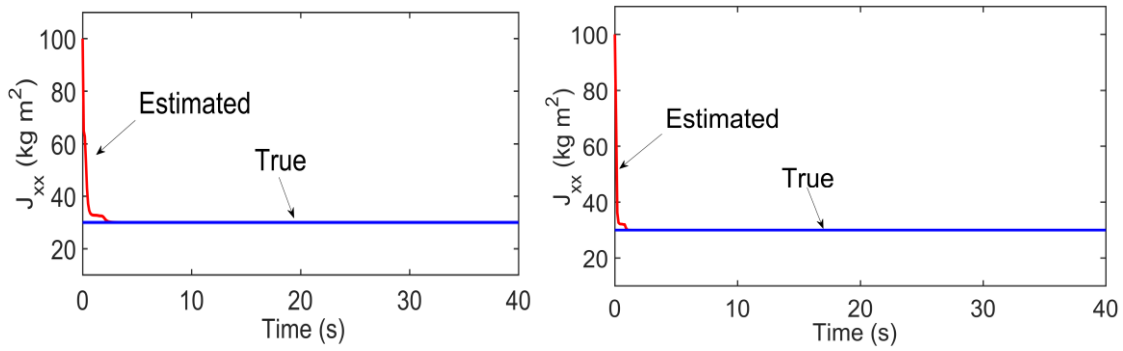

(a) (b)

Figure 5.25 J_{xx} : (a) NMPC and (b) PD controller under unbounded torque

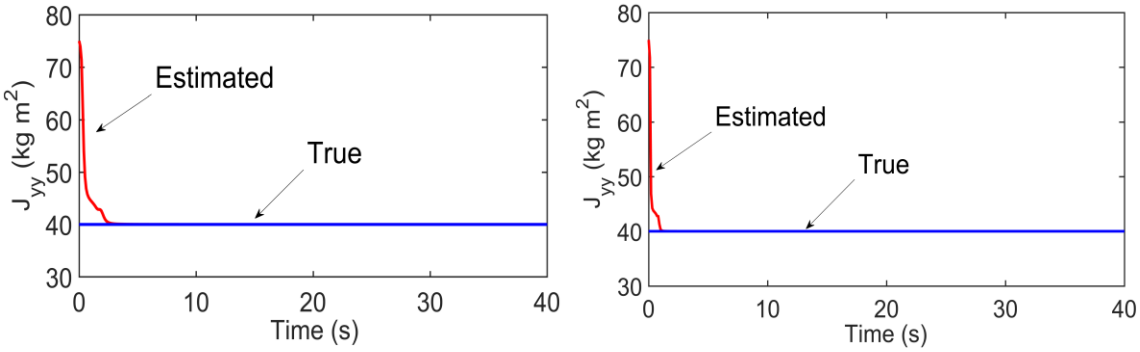

(a) (b)

Figure 5.26 J_{yy} : (a) NMPC and (b) PD controller under unbounded torque

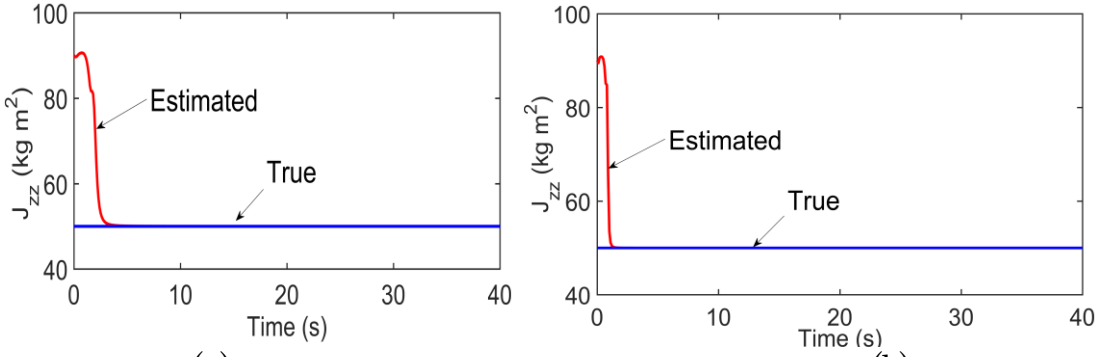

(a) (b)

Figure 5.27 J_{zz} : (a) NMPC and (b) PD controller under unbounded torque

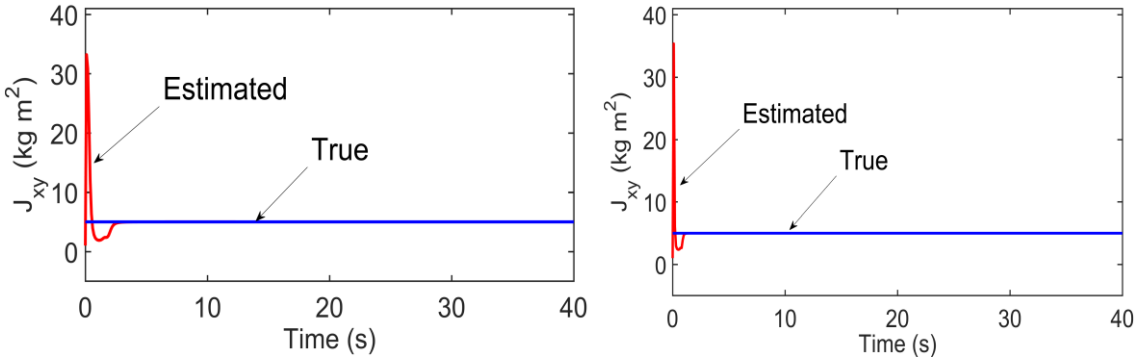

(a) (b)

Figure 5.28 J_{xy} : (a) NMPC and (b) PD controller under unbounded torque

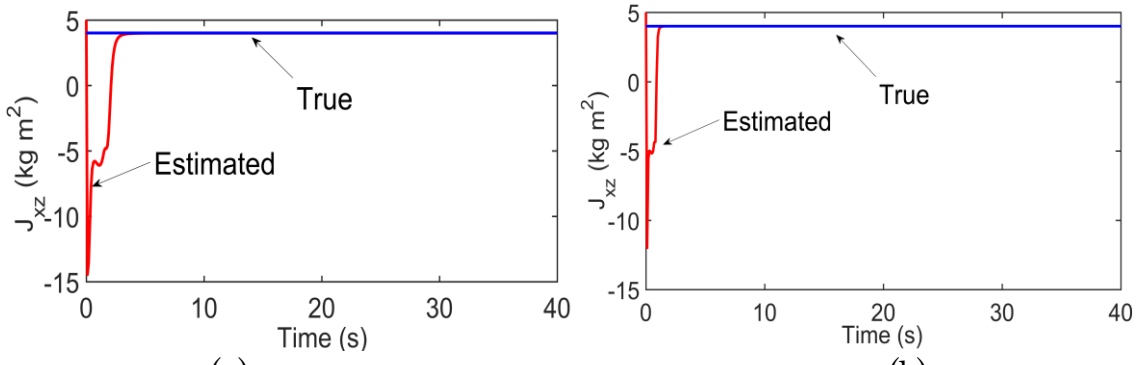

(a) (b)

Figure 5.29 J_{xz} : (a) NMPC and (b) PD controller under unbounded torque

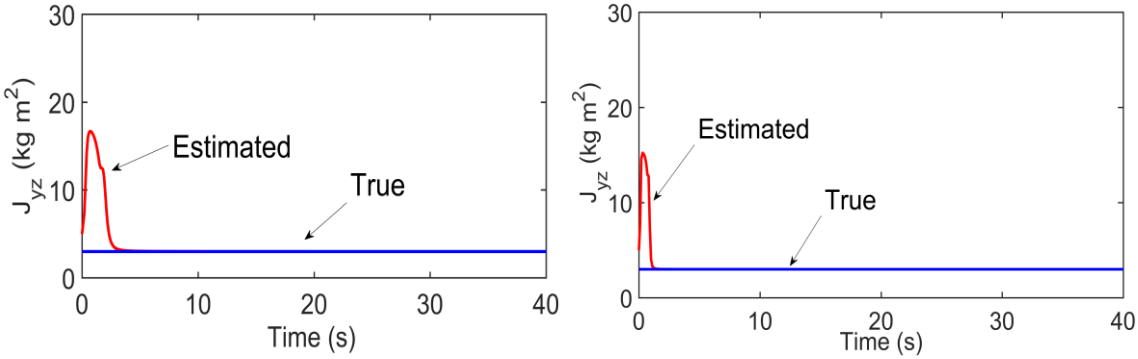

(a) (b)

Figure 5.30 J_{yz} : (a) NMPC and (b) PD controller under unbounded torque

Next, the dynamic responses of the combined spacecraft are shown in the figures below. It shows both methods achieve smooth control of Euler

angles, angular velocities and actuation torques during the attitude maneuver, respectively. The negative torque means the thrusters are working to rotate the combined spacecraft in an opposite direction. It is noted that the Euler angles under the NMPC reach the desired values with almost zero overshoot, however, the Euler angles under the PD controller reach the desired values faster but with a visible overshoot. This generally consumes more unnecessary energy due to the movement of the attitude of spacecraft.

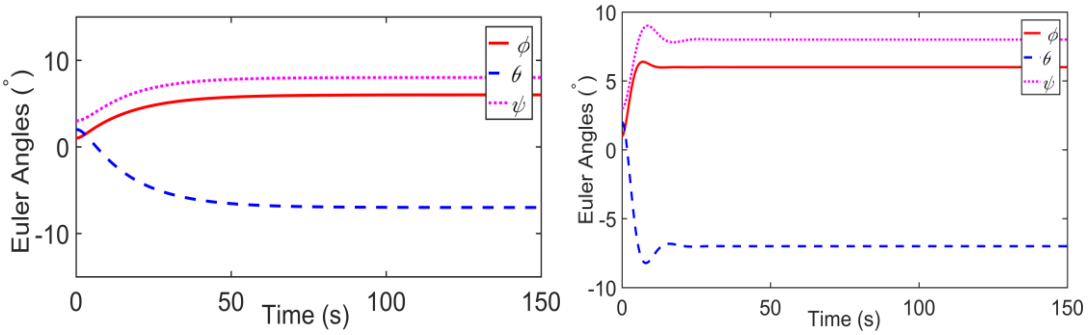

(a) (b)

Figure 5.31 Euler angles: (a) NMPC and (b) PD controller under unbounded torque

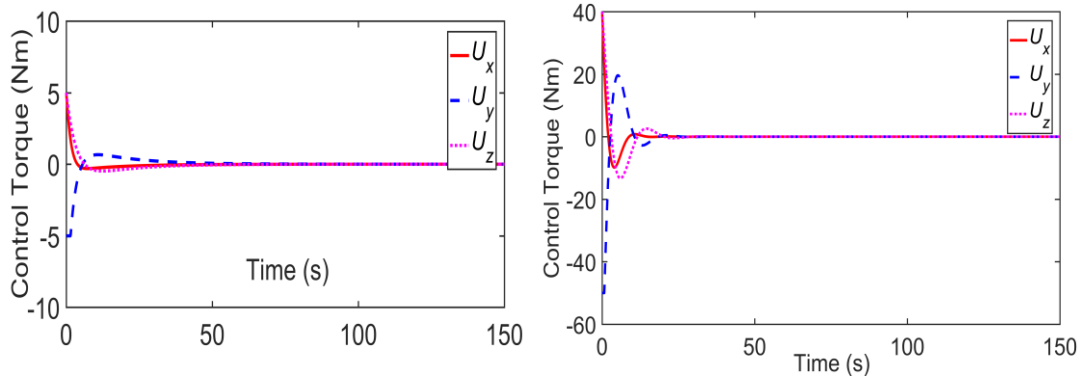

(a) (b)

Figure 5.32 (a) NMPC and (b) PD controller under unbounded torque

The angular velocities of the combined spacecraft and reaction wheels are plotted in the figures below. As expected, the angular velocities of the

combined spacecraft and reaction wheels are equal in magnitudes but with opposite directions during the attitude maneuvering. It is worth noting that although the NMPC requires more computational power and takes longer time to obtain a solution, it consumes less energy compared with PD controller. Thus, the NMPC is relatively advantageous in reducing fuel consumption.

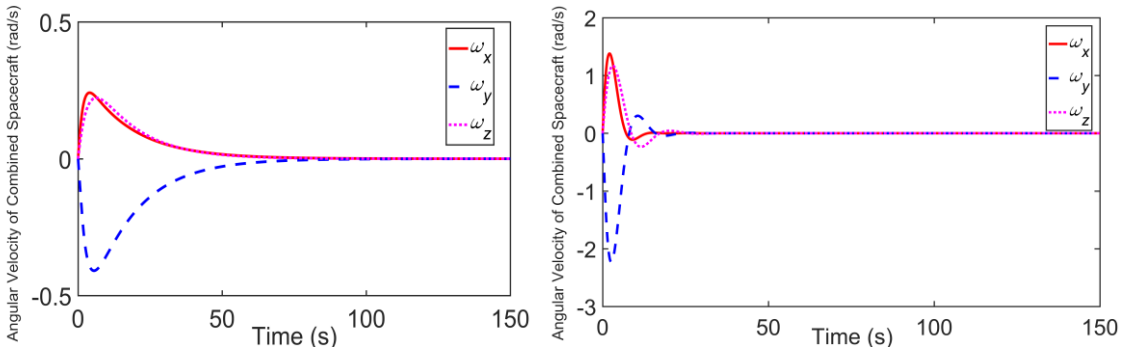

(a) (b)

Figure 5.33 Angular velocities of combined spacecraft: (a) NMPC and (b) PD controller under unbounded torque

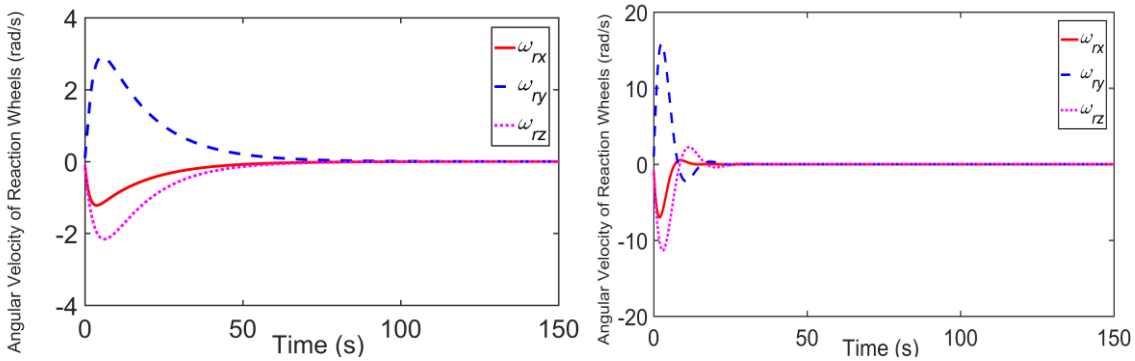

(a) (b)

Figure 5.34 Angular velocities of reaction wheels: (a) NMPC and (b) PD controller under unbounded torque

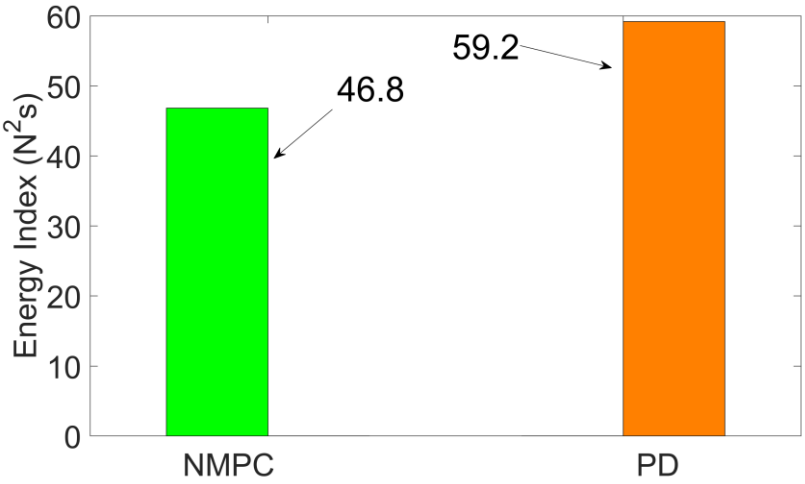

Figure 5.35 Energy consumption under unbounded torque

Under the case of bounded torque, the simulation results of inertial identification of six inertial parameters $\{J_{xx}, J_{yy}, J_{zz}, J_{xy}, J_{xz}, J_{yz}\}$ are shown in the figures below. It is noted that the initial guess of inertial parameters $\hat{\boldsymbol{J}}_0$ converges to the true values $\bar{\boldsymbol{J}}$ in both scenarios, which indicates the recursive least square method is effective and efficient in inertial parameter identification. It is noted that the identification of estimated parameters converge to the actual values with almost the same speed for each case as listed above. Since the control torque is the driving force to maneuver the attitude of the combined spacecraft and the maximum output is capped no more than 5 *Nm*, thus the estimated parameters eventually converge to the actual values almost at the same time. However, since the traditional PD controller is unable to impose constraints on the control increment, thus the output from the PD controller is more volatile than the output from the NMPC.

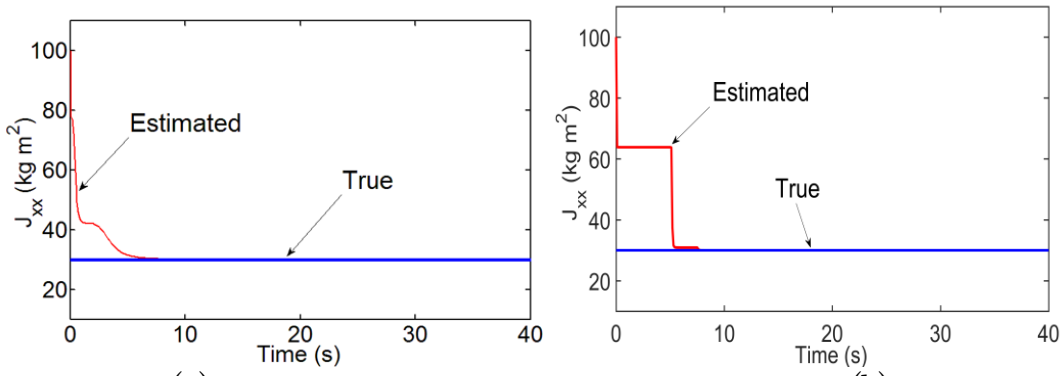

(a) (b)

Figure 5.36 J_{xx} : (a) NMPC and (b) PD controller under bounded torque

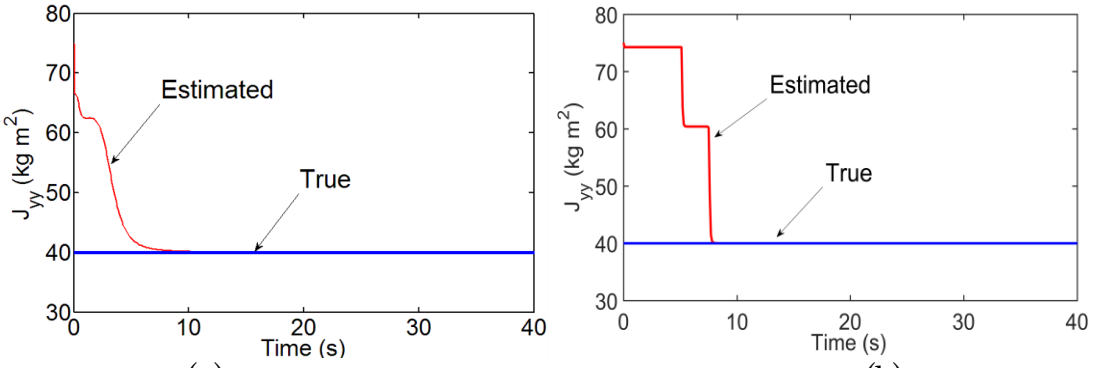

(a) (b)

Figure 5.37 J_{yy} : (a) NMPC and (b) PD controller under bounded torque

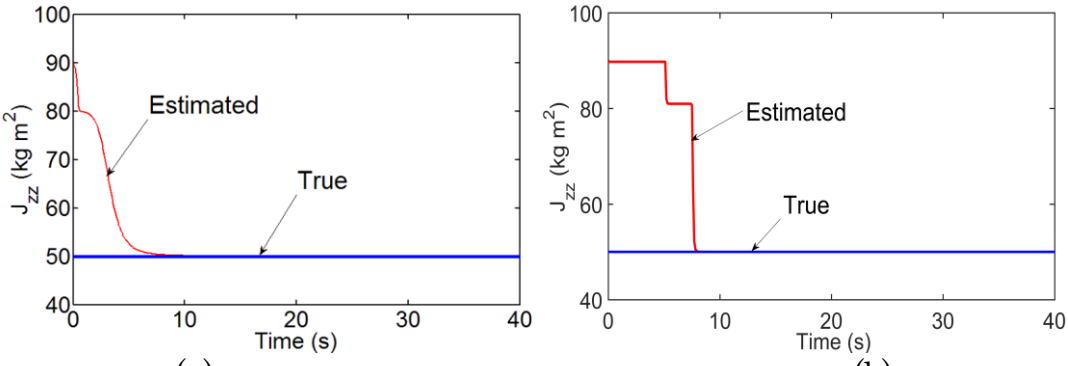

(a) (b)

Figure 5.38 J_{zz} : (a) NMPC and (b) PD controller under bounded torque

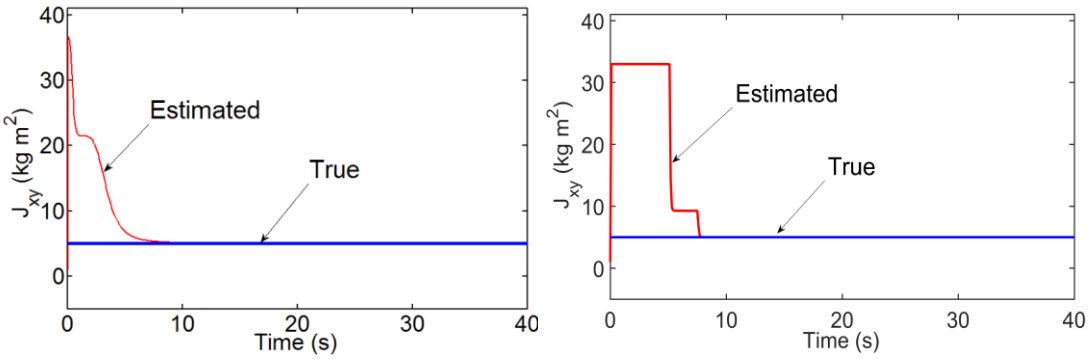

(a) (b)

Figure 5.39 J_{xy} : (a) NMPC and (b) PD controller under bounded torque

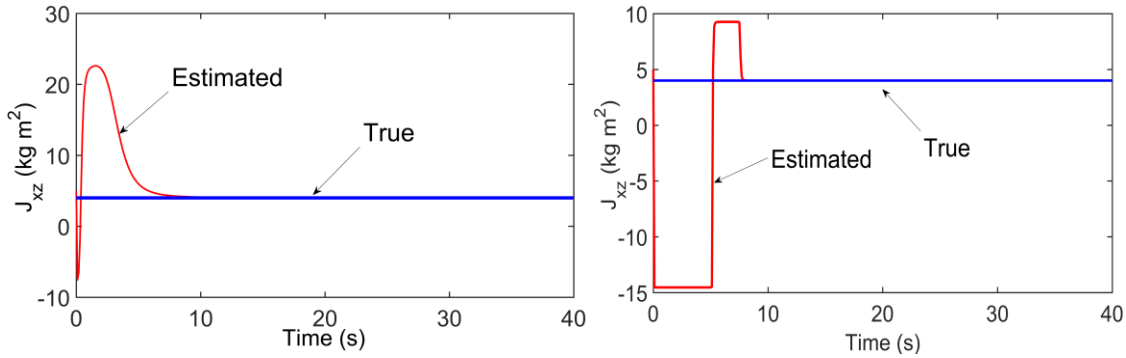

(a) (b)

Figure 5.40 J_{xz} : (a) NMPC and (b) PD controller under bounded torque

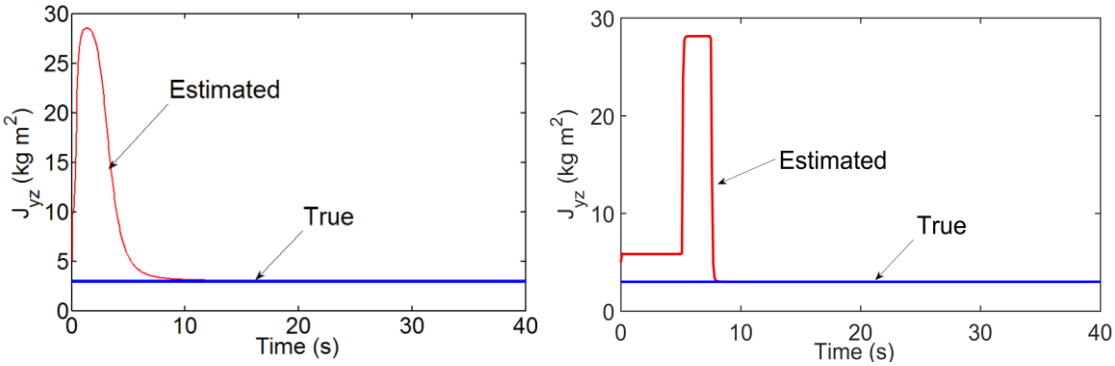

(a) (b)

Figure 5.41 J_{yz} : (a) NMPC and (b) PD controller under bounded torque

Next, the dynamic responses of the combined spacecraft are shown in the figures below. It shows the proposed control scheme successfully achieves

smooth control of Euler angles, angular velocities and actuation torques during the attitude maneuver, respectively. The attitude of the combined spacecraft approaches to the desired state smoothly, respectively for the cases of NMPC and PD control torque as shown. Apparently, the control torque exerted by the reaction wheels decays to zero and successfully achieves the required rest-to-rest attitude maneuver. The attitudes maintain stable afterwards, leading to a high accuracy attitude pointing control. The control torques converge to zero respectively in the two cases after the Euler angles reach their desired values, reflecting the effectiveness of the proposed inertial identification and control scheme. It is noted that the Euler angles curve under the NMPC has almost zero overshoot, however, the Euler angles under the PD controller reach the desired values with an apparent overshoot and this generally consumes more unnecessary energy.

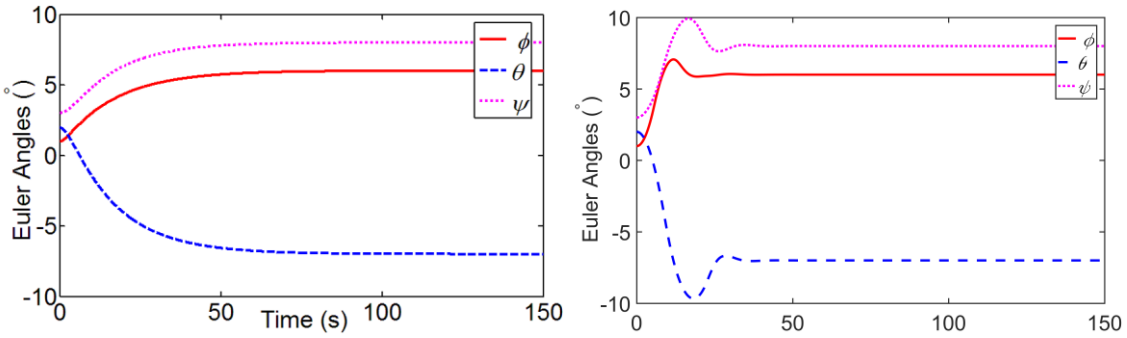

(a) (b)

Figure 5.42 Euler angles: (a) NMPC and (b) PD controller under bounded torque

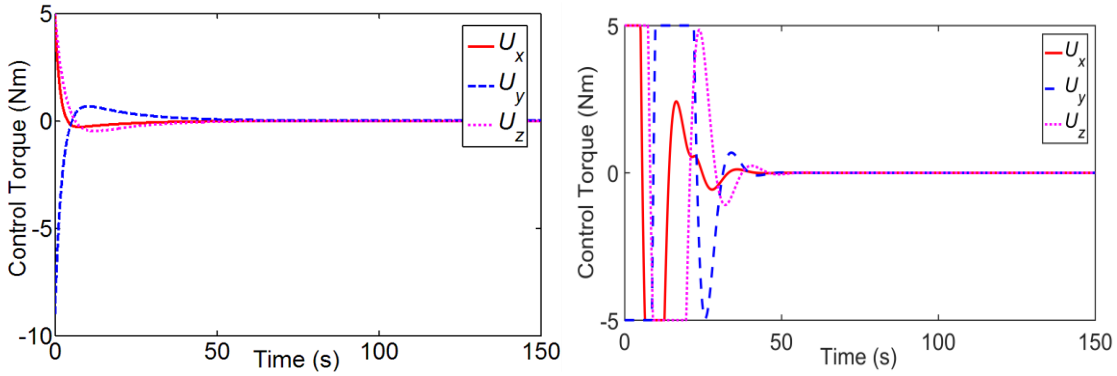

(a) (b)

Figure 5.43 (a) NMPC and (b) PD controller under bounded torque

The angular velocities of the combined spacecraft and reaction wheels are plotted in the figures below. Since there are only two parameters in the PD controller, thus the generation of control command from PD controller is fast and time efficient. Although the NMPC requires more computational power and takes longer time to obtain a solution, it consumes less energy compared with PD controller.

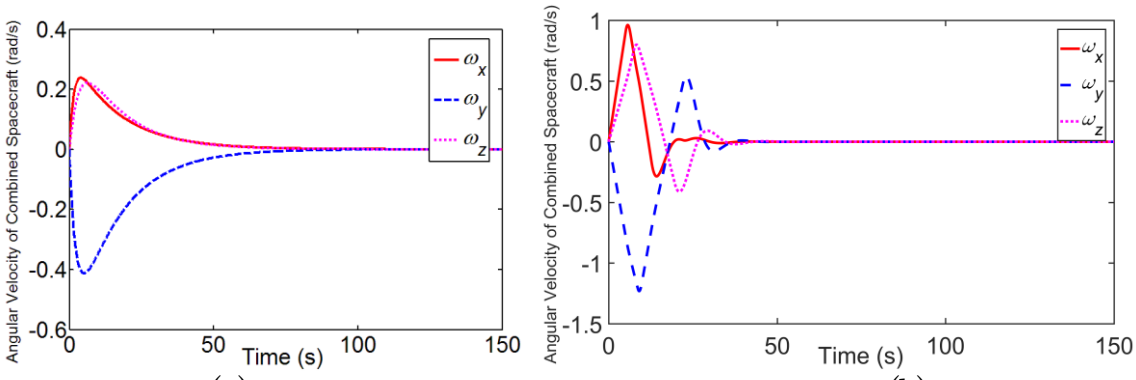

(a) (b)

Figure 5.44 Angular velocities of combined spacecraft: (a) NMPC and (b) PD controller under bounded torque

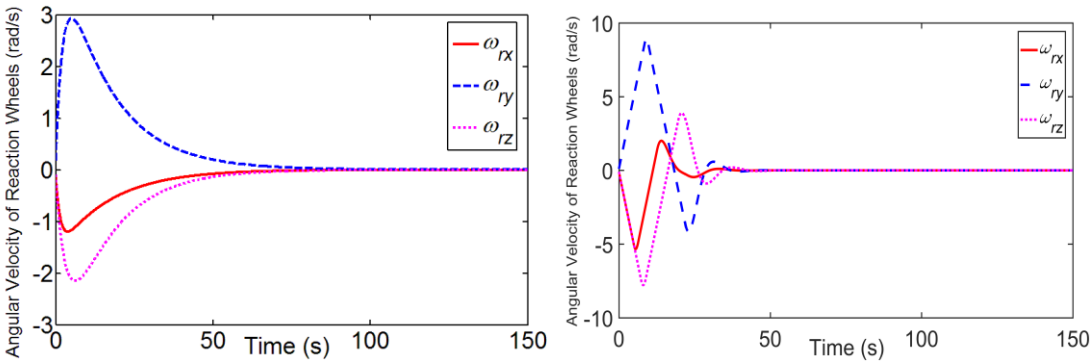

Figure 5.45 Angular velocities of reaction wheels: (a) NMPC and (b) PD controller under bounded torque

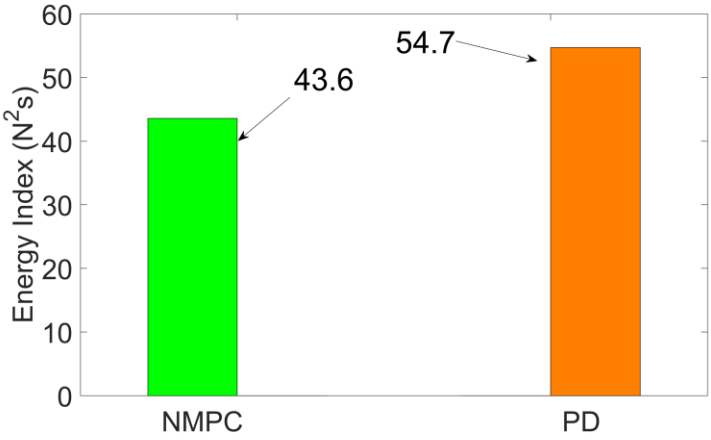

Figure 5.46 Energy consumption under bounded torque

5.4.3 Conclusion

This section develops a new scheme of inertial identification for the post-capture attitude control of a combined spacecraft by integrating the recursive least square inertial identification with the model predictive control. It provides a closed-loop optimization strategy for the attitude maneuver with unknown inertial parameters of the combined spacecraft with or without constraint of control torque magnitude. The control objective is achieved by

minimizing the control error and control increment for a smooth trajectory. As a result, the inertial parameters can be identified effectively and precisely during the attitude maneuver process. Numerical simulations demonstrate the newly proposed scheme is effective and easy to implement. The convergence rate of inertial parameter estimation is affected significantly by the available control torque. With the bounded control torque that is only a few percent of unbounded peak control torque, the proposed scheme can still converge to the true value within reasonable time.

Chapter 6 EXPERIMENTAL SYSTEM

Summary: In order to validate the proposed control algorithm, a 3 Degree-of-Freedom (DoF) spacecraft air bearing testbed system is designed and built to conduct physical experiments on the ground. The supporting hardware is designed to make the testbed system upgradable and expandable for the potential purposes in the future. The software of the simulator control system for the experimental validation is designed from the scratch, MATLAB compiler is embedded into LabVIEW to construct a hybrid programming environment. The detailed descriptions of each subsystem are given in this chapter.

6.1 Air bearing Spacecraft Simulator Testbed

The experimental testbed is composed of two simulators on a granite table with high-accuracy surface. This testbed can be used for ground testing of guidance, control and navigation subsystem for spacecraft proximity operations. The granite table with a size of $2m$ by $4m$ is to support the floating spacecraft simulator with 2 DoF translational motion and 1 DoF single-axis

attitude maneuver. To produce the weightless and frictionless conditions, three air bearings mounted at the bottom of each simulator simultaneously eject high-pressure compressed air to the table to provide floatation.

Seen from the figures below, the web camera on top of the simulator and the LED lights pattern mounted on the ceiling are designed as the star tracking navigation system. In particular, the camera captures the fixed geometric pattern of the LED lights at a certain frequency, the simulator's position and attitude are then determined by comparing these pictures at successive time instants.

It is worth noting that the experimental testbed is assembled and placed by professionals with necessary devices and equipment. Each part in the subsystem is purchased from the particular company in that field, more detailed information regarding every sensor is provided in the following sections respectively. My work on the experiment mainly focuses on the electrical connection of subsystems, i.e., reaction wheel, thruster and air tubes. Moreover, in order to make the experimental run smoothly, troubleshooting, solving the expected and unexpected problems are also key part during the setup of the experiment. Programming of communication software and communication test between the console computer and each subsystem are part of my efforts as well. In addition, design of experimental scenarios, the implementation of each experiment and result analysis are the core of our work

in the experimental validation of the thesis.

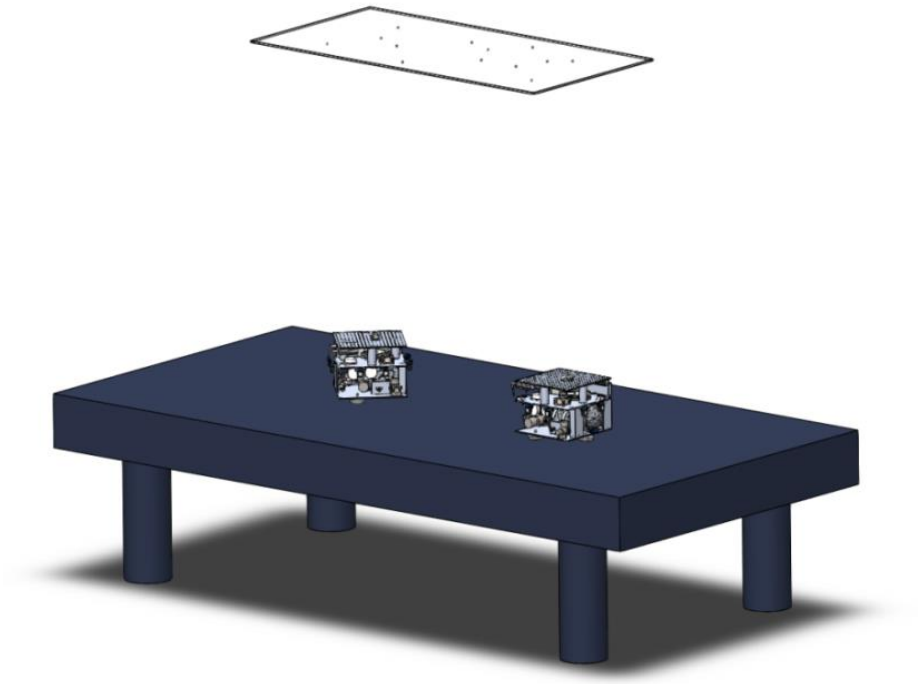

Figure 6.1 CAD model of the simulation system

Figure 6.2 Photograph of the ground testbed

6.2 Simulator Subsystems

The simulator is designed to have a two-layered structure with four key subsystems: air supply subsystem, power supply subsystem, onboard computer subsystem and the payload subsystem, i.e., sensors and actuators. Particularly, two air tanks and the air tubes are placed at the bottom, the battery, onboard computer and the payloads are placed at the upper layer. The structure is upgradable and extendable for additional structures, i.e., flexible appendages and robotic arm. The details are presented in the figures below.

Table 6.1 Characteristics of simulator

	Parameter	Value	Unit
Size	Width	420	mm
	Length	420	mm
	Height	370	mm
	Mass	21	kg
Reaction wheel	Moment of inertia	0.46	$Kg.m^2$
	Max torque	0.025	Nm
	Max Angular Momentum	0.06	Nms

	Propellant	Air	
Jets	Operating pressure	0.4	MPa
	Nominal thrust	0.065	N

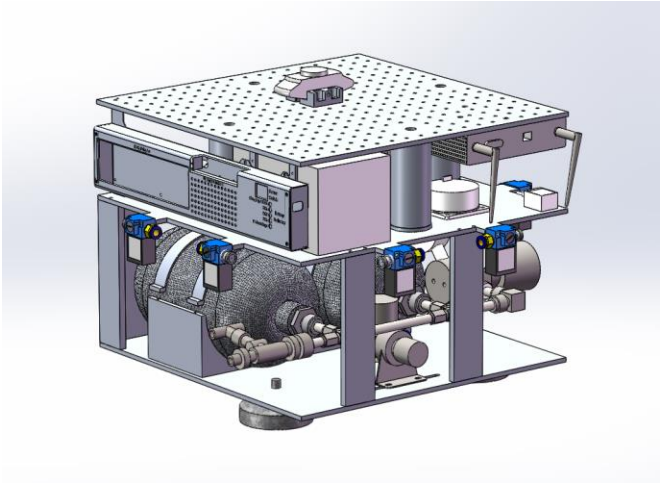

Figure 6.3 CAD model of the satellite simulator

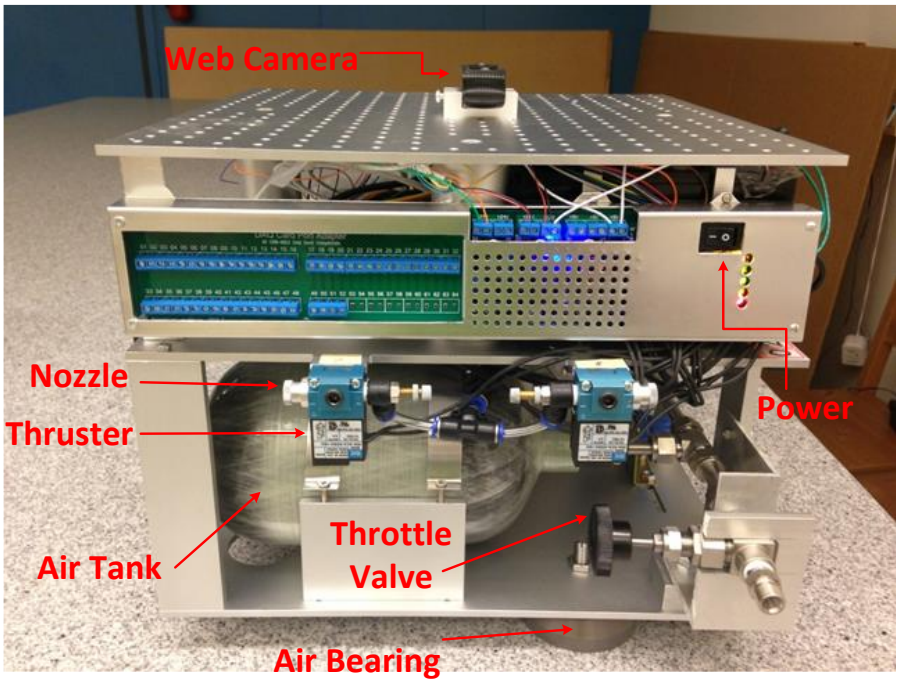

(a)

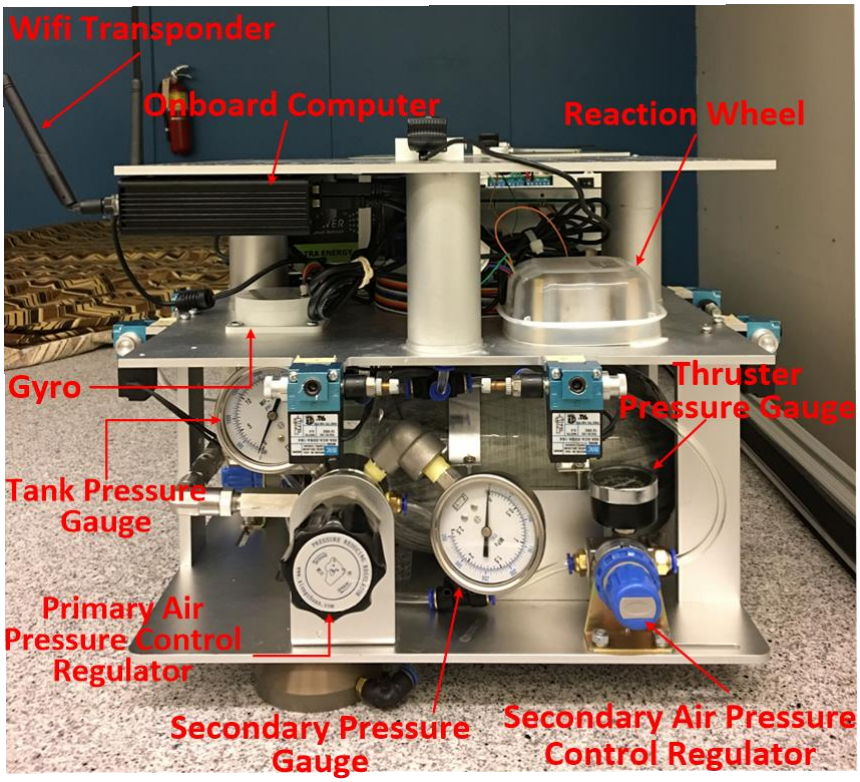

(b)

Figure 6.4 Simulator structure and payloads

In this meantime, the plumb line approach is applied to determine the center of gravity of the irregularly shaped simulator. The principle behind this approach is that the force of gravity passes through the center of gravity in a vertical line by hanging up the simulator from different points. When the simulator is suspended, its center of gravity is along this plumb line from the hanging point. The intersection of the plumb lines is viewed as the center of gravity for the simulator. As seen from the result, the three plumb lines converge to a very narrow region where the center of gravity lies in. The measurement result is very close to the geometric center, less than 1.5 *cm*.

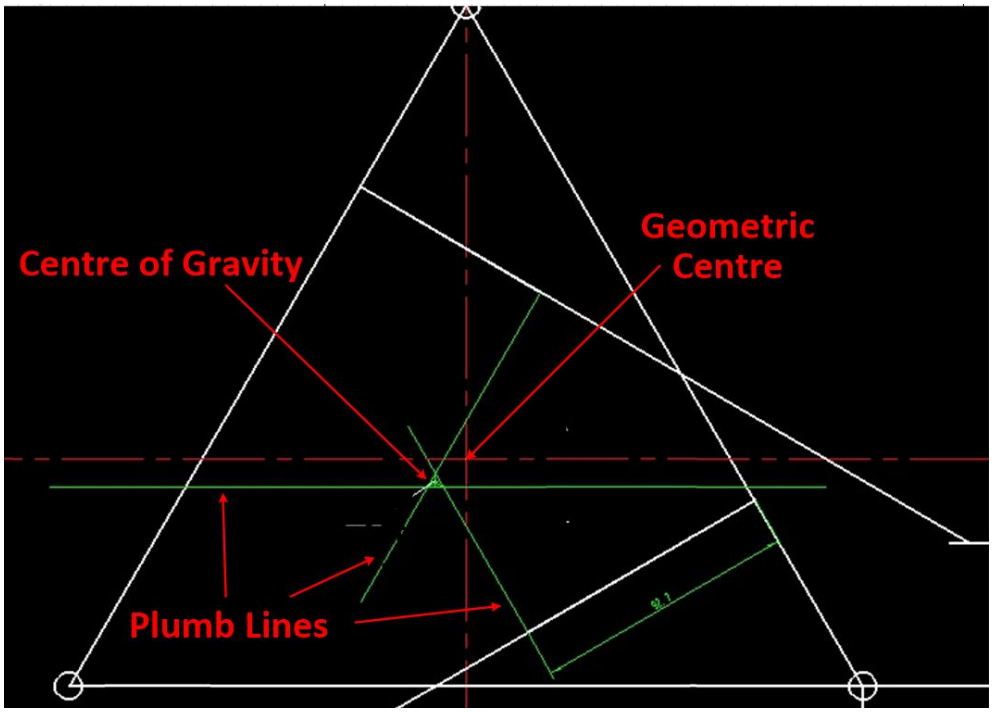

Figure 6.5 Measurement of center of gravity versus geometric center

6.2.1 Onboard Computer

The onboard computer, powered by a 12 Ah Lithium-ion battery, is a mini-PC which includes an Intel Pentium N3510 2GHz processor with 8G random-access memory. Considering the possible chattering caused by the translational and rotational motion of the simulator, a 128G solid state drive is equipped for system stability, running efficiency and data storage. Moreover, cooling fins is embedded into the onboard computer to achieve better cooling performance and wireless Ethernet adapter is integrated to the onboard mini-PC. To setup the experiment, an offboard computer firstly logs into the onboard

mini-PC that generates the accessible wireless internet.

6.2.2 Hardware Connection and Communication

As a mechatronic system, electronic hardware of the spacecraft simulator may have different connection interfaces. In this case, they are all unified to the standard USB interface by a general data acquicition card. The USB-6212 DAQ card by National Instrument is a lightweight mechanical enclosure and a multifunction data acquisition device. It offers analog and digital I/O ports to acquire sensors' data and send commands to actuators. Furthermore, it includes NI-DAQmx driver and configuration utility to simplify the configuration and measurements. It features signal streaming technology that gives DMA-like bidirectional high-speed streaming of data across USB. The unoccupied ports on the USB-6212 DAQ card are reserved for potential electronics upgrade in the future, i.e., provide I/O ports for robotic arm and other new actuators. The device is ideal for test, control, and design applications including portable data logging and data acquisition.

Figure 6.6 USB-6212 DAQ from National Instrument

6.2.3 Air Supply System

The key part of the air supply system is the two air tanks with 2 L volume for each of them. The air is compressed into the tanks by the air compressor from the throttle valve. The high-pressure air in the tanks is then distributed into another two regulators, which are used to regulate the air pressures to predefined values for thrusters and the air bearings, respectively. As a result, the air pressures for the thrusters and the air bearings are regulated separately. In total, 9 electromagnetic valves are used to control the on and off of the air bearings and thrusters. Specifically, one electromagnetic valve is used to control the on and off of the three air bearings while the other 8 are used to control the 8 cold gas thrusters, respectively.

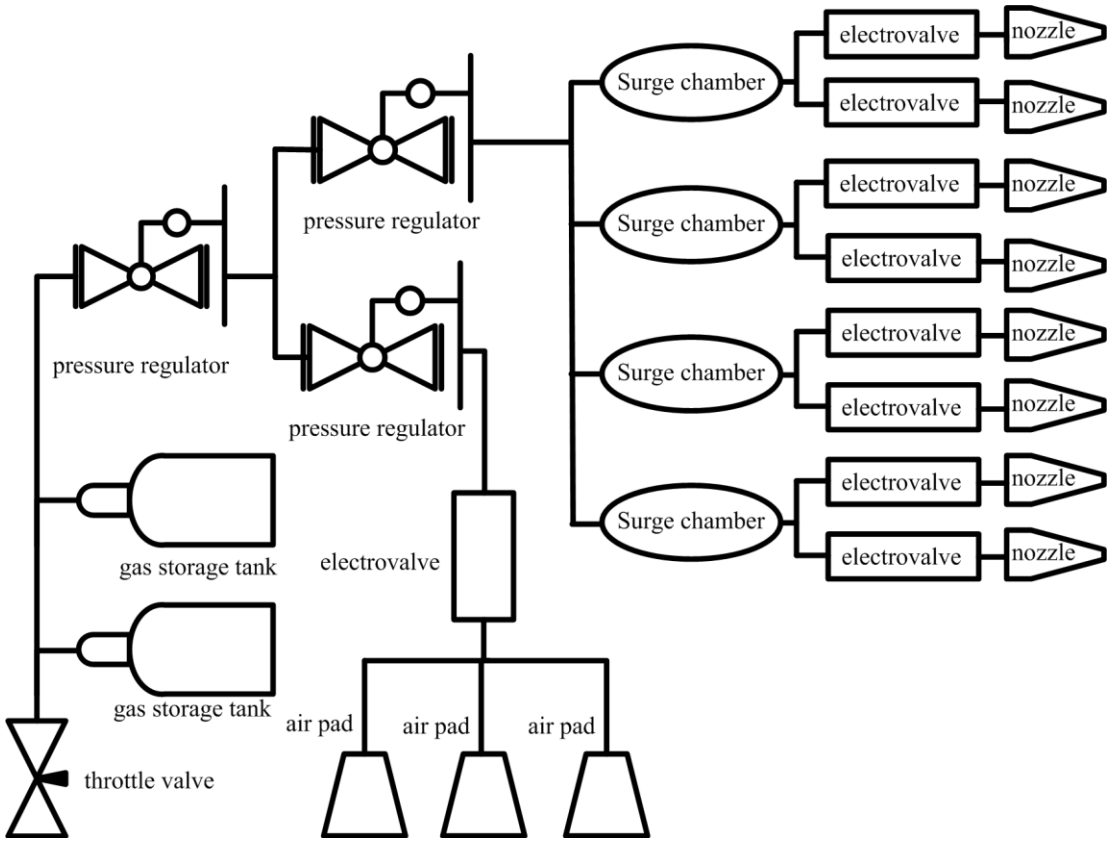

Figure 6.7 Schematic of the air supply system

6.2.4 Reaction Wheel

The reaction wheel used in this experiment is a product from Sinclair Interplanetary, which provides the high reliability vacuum lubricated reaction wheels for microsatellites. The reaction wheel offers the continuous, precise and smooth control torque with high accuracy for attitude maneuver. A digital processor is built in to receive and transmit information between the mini-PC and the reaction wheel. The reaction wheel can be commanded over a serial bus to produce a desired speed, momentum or torque. The detailed datasheet is given as follows.

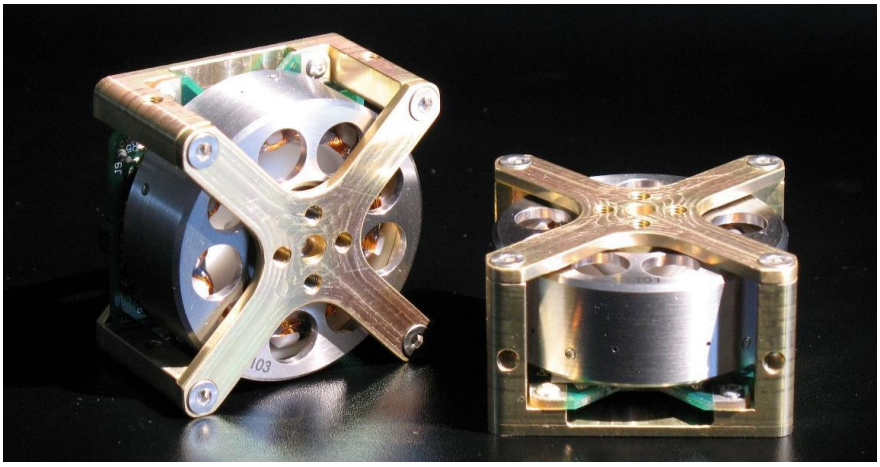

Figure 6.8 Reaction wheel from Sinclair Interplanetary

Table 6.2 Datasheet of the reaction wheel

Nominal Momentum	7 mNm-sec@4460 RPM
Nominal Torque	1 mNm
Control Mode	Speed or Torque, built-in CPU
Command/Telemetry	UART, or SPI
Mechanical	50mm × 40mm × 27mm, 90 g mass
Supply Voltage	3.4 to 6.0 V nominal (8V max)
Supply Power	0.7 W maximum under full torque 0.2 W @ 4460 RPM steady-state 0.1 W @ 2000 RPM steady-state
Environment	-40°C to +70°C operating temperature
Reliability	Diamond coated hybrid ball bearings

6.2.5 Optical Gyro

Optical gyros from Fizoptika are used as embedded or stand-alone sensors to provide measurement and feedback to the control input. The light-weight and flexible product enhances the system performance by significantly reducing the size and weight.

Figure 6.9 Optical gyro VG103PT from Fizoptika

The model VG103PT offers the combination of excellent performance and superb shock/vibration endurance. This fiber optic gyro without any metal part features compact fully plastic design. During the experimental process, the optical gyro is employed to measure the angular velocity of the simulator at every sampling instant. Then, the data is fed into the attitude controller as feedbacks to form a closed-loop control strategy. The details are provided in the table below.

Table 6.3 Datasheet of the optical gyro

ARW (deg/h)	0.02˚
Input Range (deg)	350˚
Bias Stability (deg/h)	1˚
Magnetic Immunity	<0.01
Operating Temperature	-40˚C-70˚C
Power (Watt)	0.5
Shock (g)	750
Vibration (g)	18
Mass (g)	60

Chapter 7 EXPERIMENTAL VALIDATION

Summary: In this chapter, the application of the proposed method on the attitude controller design of the floating spacecraft simulator is studied. The goal is to implement the NMPC method and test its executable efficiency under an experimental setting. To validate the proposed control method, the various sensors are connected and debugged with the spacecraft simulator platform. In the meantime, the software is self-developed by integrating MATLAB into the LabView environment. The control performance is evaluated through a set of simulations in the presence of environmental disturbances. The experimental results and discussion under various scenarios are presented accordingly.

7.1 Problem Formulation

The air bearing based floating simulator provides an ideal testbed to apply the proposed algorithm and demonstrate its effectiveness. Considering the online optimization technique involved in the receding horizon process, the popular concern toward NMPC approach is whether it can be implemented

practically as an on-line control command generator. Compared with the traditional off-line control approach, the optimal control problem is solved in advance, the control commands are stored and implemented at each time step. The on-line control approach solves the constrained optimal control problem at every time instant, and the control command is then directly applied to control the motion of the simulator.

Furthermore, the sensitivity of the proposed NMPC to the environmental disturbance is also worth studying. Because the aerodynamic drag imposing on the spacecraft simulator during the attitude maneuvering process are unavoidable for on-the-ground testbed, and this may deteriorate the control performance to some extent.

For this purpose, the air floatation-based spacecraft simulator is used to emulate the weightlessness and frictionless motion in space. Based on the assumptions of zero residual viscous forces between the high-accuracy granite surface and the air bearing, the attitude dynamics of the floating spacecraft simulator is governed by simplifying the Euler dynamic model into the case of the single-axis rotation.

Due to the restrictions of limited size and weight, small-scaled satellites are not equipped with thrusters. In the meantime, the reaction wheel is able to output continuously smooth torque and guarantees the pointing precision during the attitude maneuver. Therefore, the reaction wheel is selected as the

only actuator that implements the commands from the NMPC controllers.

7.2 Experimental Setup

A real time operating system is running in the simulator's onboard computer and an ad-hoc wireless internal network is established before starting the experiment. The desktop computer is used as control terminal to login to the onboard computer through the wireless network offered by the simulator. Upon taking control of the simulator, the control software built in the LabView environment starts to establish communication of the reaction wheel. Then, the NMPC based attitude controller is executed in the software running onboard.

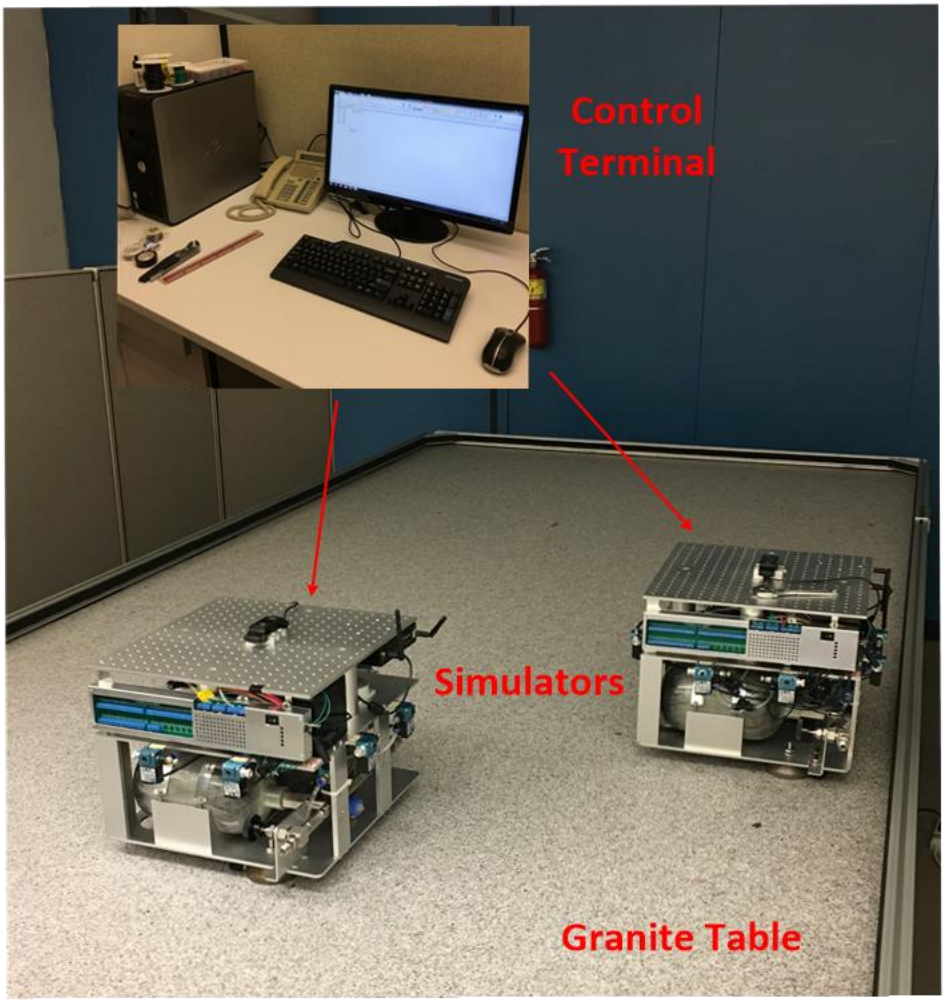

Figure 7.1 Experimental setup

To start the experiment, two air tanks are filled with compressed air by the air compressor. The air pressure on the air bearing is adjusted to appropriate value so that the simulator is lifted up without friction with the table. In the meantime, the pressure on the thrusters is adjusted to provide the thrusters with the calibrated force. The exact values of the pressure on different gauges are listed in the table below.

Table 7.1 Air pressure on the gauges

Gauge	Value (MPa)
Tank Pressure Gauge	15
Secondary Pressure Gauge	1
Thruster Pressure Gauge	0.4

7.3 Experimental Results

In this section, the experimental results are presented in detail. The spacecraft simulator is initially placed at rest in an arbitrary initial attitude, and this initial angle is set to be 0°. The control objective is to drive the body of the simulator to rest at a specified attitude. Therefore, this is a rest-to-rest attitude maneuver with zero angular velocity for both the initial and final states. Two attitude control scenarios are performed in this part, small-angle attitude maneuver and large-angle attitude maneuver, respectively. The control magnitude constraint is added to both scenarios. However, the constraint of the simulator's angular velocity is only added to the large-angle attitude maneuver case to protect the reaction wheel from hardware damage. The predictive horizon and control horizons in the NMPC are defined as N = 30 and Nc = 1, and the values of the weight matrices are $\boldsymbol{P} = 1$ and $\boldsymbol{Q} = diag(1, 1)$.

Once floating up, the environmental disturbance causes the simulator to start rotating on the table and the effect of the external torque accumulates

with the increase of time. Figure 7.2 shows the time histories of attitude angle and angular velocity with zero control torque. This curve indicates the overall external impact from the environment when the simulator is floating over the table. There are multiple sources for the external effects. In particular, the residual viscous friction between the air bearings and the floating surface may generate impacts on the simulator. Moreover, due to the transportation and daily use, the scratched surface at the bottom of the air bearings produces uneven airflow underneath the simulator, and the uneven ground subsidence caused by the 6-ton granite table sitting on the floor makes the granite table further tilted as time goes on. All these factors together generate a disturbance torque, which is acting as a perturbation to the attitude of the simulator during attitude maneuvering.

The high-speed airflow coming out of the air bearing actually goes to the surface of the table along all directions, any scratch on the air bearing may deviate the airflow from its original path, and further produces a perturbation to the simulator's attitude and stability.

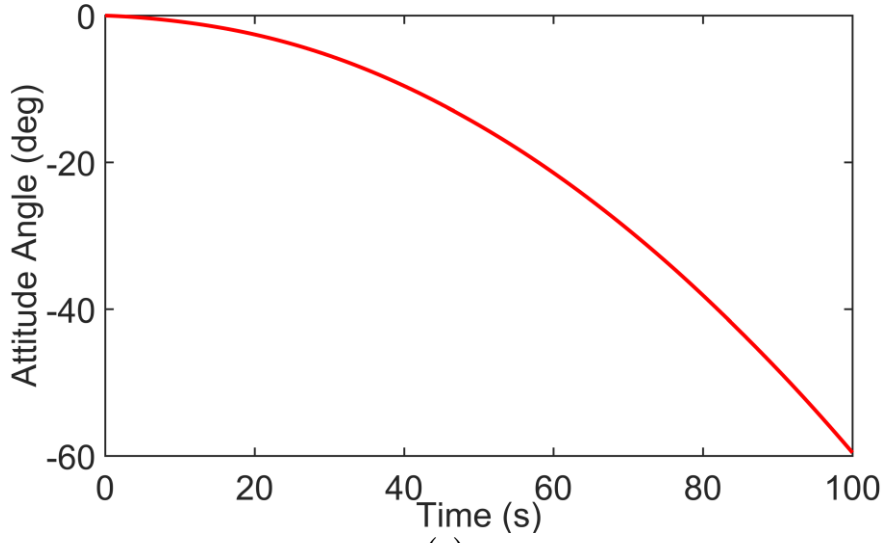

(a)

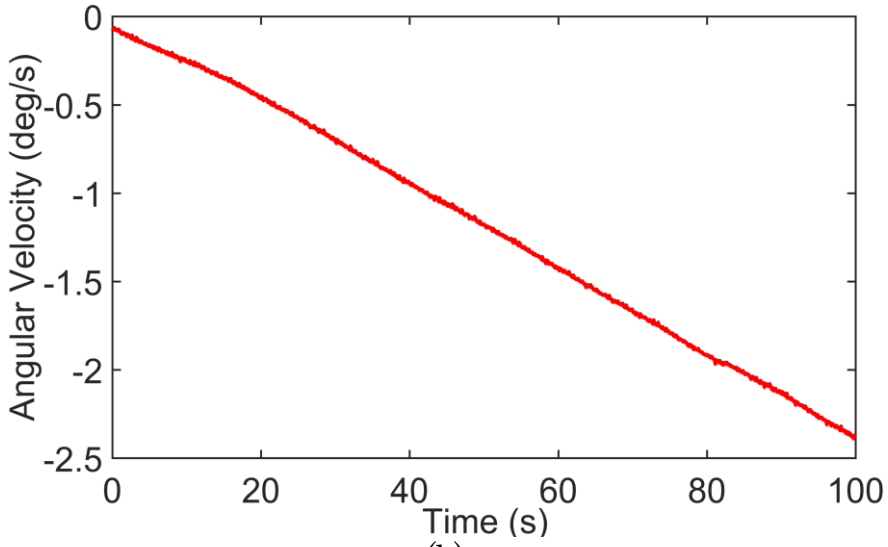

(b)

Figure 7.2 Zero control case: (a) attitude angle and (b) angular velocity

7.3.1 Small-angle Attitude Maneuver with Reaction Wheel

In this case, the attitude control of the simulator is studied through small-angle attitude maneuver with the control magnitude constraint. The desired angle is set to be 8° in the small-angle attitude maneuver case after repetitive tests. The maximum control torque from the reaction wheel is

limited to 0.001 *Nm*, which is the nominal torque. It is worth noting that the onboard reaction wheel is designed as attitude control actuator for a picosatellite, which is generally considered with a mass of no more than 1 *kg*. Therefore, the reaction wheel is relatively less capable to drive the attitude of the simulator with a mass of 21 *kg*. Finally, the simulation time is set to 90 *s* and the sampling time step is 0.1 *s*. The block diagram of small-angle attitude maneuver is given as follows.

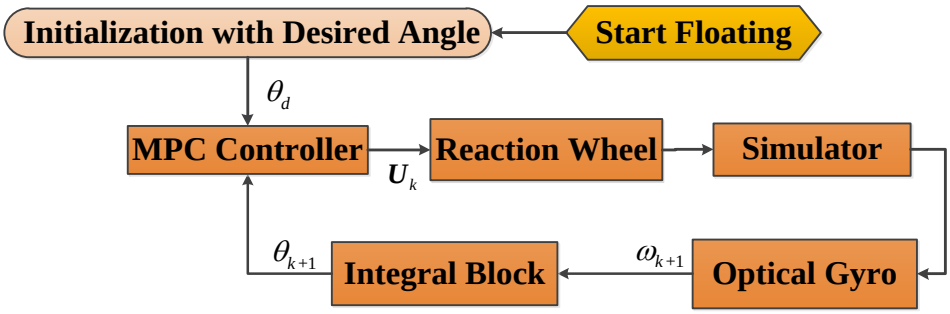

Figure 7.3 Block diagram of small-angle attitude maneuver

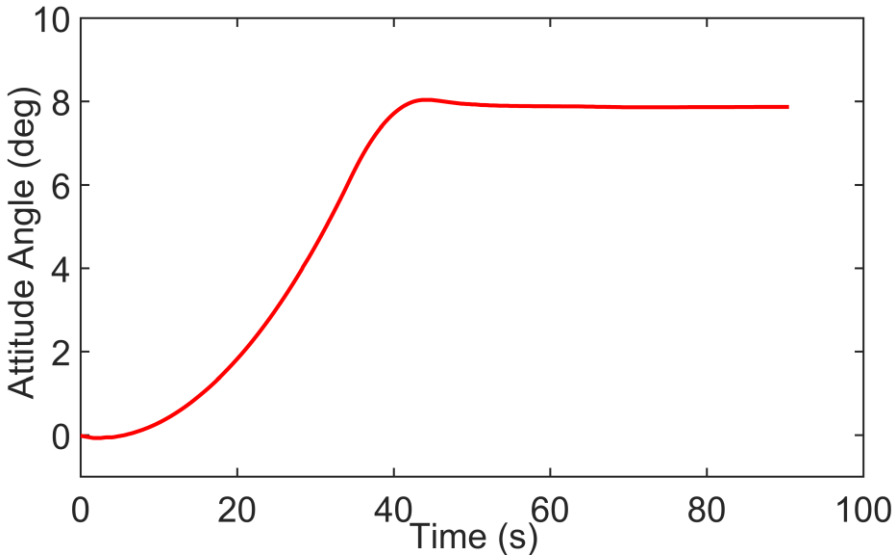

Figure 7.4 Small-angle case: attitude angle

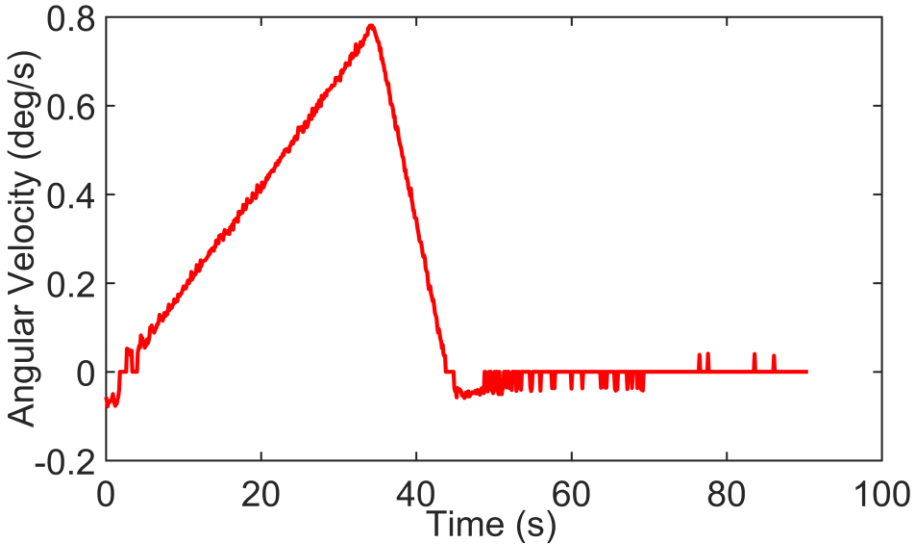

Figure 7.5 Small-angle case: measured angular velocity

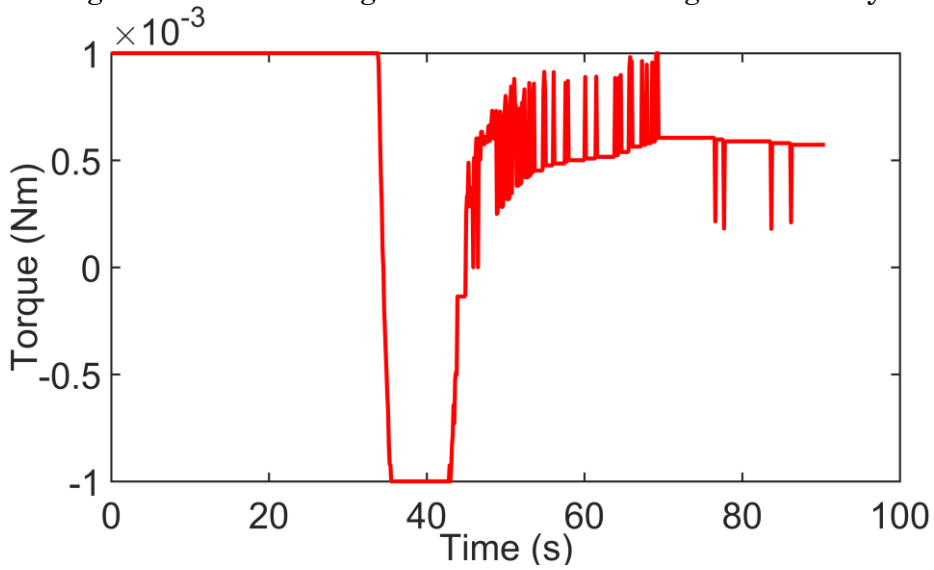

Figure 7.6 Small-angle case: control command from NMPC controller

Figures 7.4-7.6 show the simulation results using NMPC attitude controller for a small-angle attitude maneuver. As indicated from the curves, the attitude angle reaches the desired value at around 50 *s*. The attitude angle curve is smooth and there is almost no overshoot during the maneuvering process. With a constant control torque of 0.001 *Nm* in the first 30 *s*, the

simulator starts rotating with an increasing speed. In the meantime, the angular velocity of the simulator starts dropping after reaching close to $0.8^{\circ}/s$, and the control torque turns to -0.001 Nm from around 36 s to 42 s to slow down the rotation of the simulator. The glitches on the curves of angular velocity and control torque indicate the environmental disturbance during the attitude maneuvering process. As seen, the simulator is generating torque still to offset the negative effect from the environment after reaching the desired angle. Obviously, there is no air in space but the aerodynamic drag does exist during the ground experiment.

In this section, the NMPC is applied to maneuver the attitude of the simulator in a small-angle scale using reaction wheel with limited output. The attitude angle of the simulator successfully reaches the predefined target value. During the atittude maneuvering process, the existence of external torque proves the robustness of the NMPC attitude controller that is capable to maneuver the simulator's attitude to desired value despite of the perturbation. It is worth noting that a larger reaction wheel with a bigger torque output would be capable to maneuver the attitude of the simulator in a larger scale, even when the external disturbance exists. In this experiment, the small-angle attitude maneuver case is mainly restricted by the capacity of the current reaction wheel and the influence of the external torque disturbance from the environment.

7.3.2 Large-angle Attitude Maneuver with Reaction Wheel

In this case, the attitude control of the simulator is studied through large-angle attitude maneuver. As stated, the nominal torque of the current reaction wheel is relatively small versus the mass of the simulator, and simply using nominal torque leads to a relatively longer time to reach a large desired angle. The reaction wheel needs to be continuously working to offset the negative disturbance from the environment and the limitations of the testbed. As a result, the reaction wheel with an increasing speed may reach its saturation zone before reaching the desired angle. Therefore, it is very difficult to implement a large-angle maneuver using the given nominal torque.

An ad-hoc control scheme is proposed to effectively maneuver the attitude of the simulator in a large-angle scale and protect the reaction wheel from exceeding its inherent maximum rotating speed. Specifically, the control scheme consists of two constraints: the internal control magnitude constraint and the external constraint on the angular velocity of the simulator. The internal constraint is an inequality constraint embedded in the NMPC attitude controller, while the external constraint is to cut the control torque to zero when the angular velocity of the simulator reaches the defined maximum value. This external constraint effectively stops the reaction wheel entering its saturation zone and protects the hardware from damage. This is because by selecting the reaction wheel as the only attitude maneuvering actuator, the

angular momentum of the simulator is equal to the angular momentum of the reaction wheel, i.e., $\boldsymbol{J\omega} = \boldsymbol{J}_r\boldsymbol{\omega}_r$, at every time instant. The moment of inertia of both the simulator and reaction wheel can be viewed as constant during the attitude maneuvering. Therefore, the angular velocity of the reaction wheel can be capped by limiting the angular velocity of the simulator. The block diagram of large-angle attitude maneuver is shown as follows.

Finally, the desired angle for this scenario is set to be 30°, the maximum control torque from the reaction wheel and maximum angular velocity of the simulator is chosen to be 0.012 Nm and 3°/s, respectively. The simulation time is set to 75 s and the sampling time step is 0.1 s.

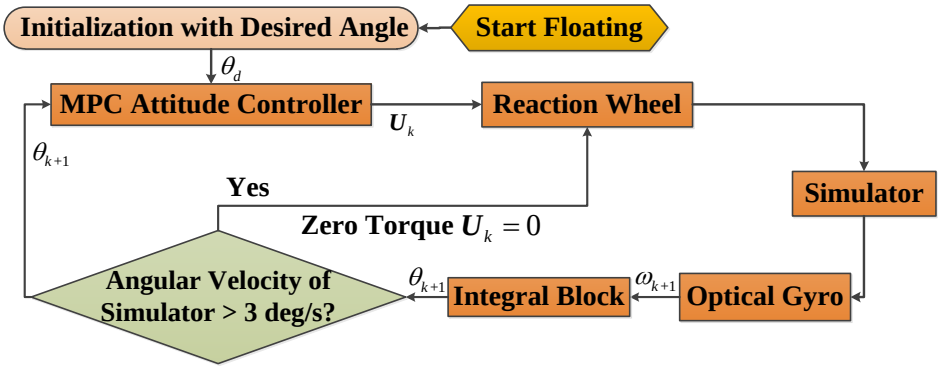

Figure 7.7 Block diagram of large-angle attitude maneuver

Figures 7.8-7.10 show the time histories of attitude angle, angular velocity of the simulator, and control torque from the reaction wheel, respectively. As seen, the attitude angle reaches its desired value at 30 s, the curve is smooth and there is nearly no overshoot during the attitude maneuvering process. At the very beginning, the control torque reaches the

given maximum value of 0.0012 Nm. The reaction wheel implements the control torque calculated by the NMPC attitude controller, which drives the simulator to start rotating at the maximum acceleration in the first couple of seconds. In the meantime, the simulator with continuous torque is rotating at an increasing speed and this makes it reach the predefined maximum angular velocity, i.e., $3^{\circ}/s$, quickly. At the time instant of reaching the maximum angular velocity, the control torque is cut to zero, but the simulator continues rotating simply by inertia after eliminating the torque output. The angular velocity of the simulator exceeds the maximum value but starts dropping soon under the influence of environmental disturbance. Since there is still a difference between the current and the desired attitude angles, the attitude controller outputs the maximum control torque and drives the angular velocity of the simulator increase again when the angular velocity falls below $3^{\circ}/s$. The process of exceeding and dropping the maximum angular velocity, as seen between 5 to 20 seconds, repeats for a couple of times while the attitude angle is increasing. In a real space environment where the environmental torque is negligible, the angular velocity of the spacecraft would remain at the value when the torque is cut to zero until the attitude controller outputs a negative torque.

When the attitude angle is about to reach the desired value, 30° in this case, the NMPC attitude controller outputs a negative torque that brakes the

angular velocity and slows down the existing rotation. Then, the negative torque gradually decays to zero as time goes on until the attitude angle eventually reaches the desired value. Moreover, the control torque glitches indicate the effects of the environmental disturbance on the simulator. The reaction wheel is working still to resist the negative environmental torque and maintain the simulator's attitude.

In this section, an ad-hoc control scheme is implemented to maneuver the attitude of the simulator in a large-angle scale while protecting the reaction wheel from exceeding its maximum rotating speed. The maneuvering process is smooth and there is nearly no overshoot during the attitude maneuvering process. As seen during the attitude maneuvering process, this control scheme successfully maneuvers the simulator using a limited output reaction wheel. The experimental results demonstrate the effectiveness of the NMPC attitude controller and the proposed control scheme in spite of the external disturbance.

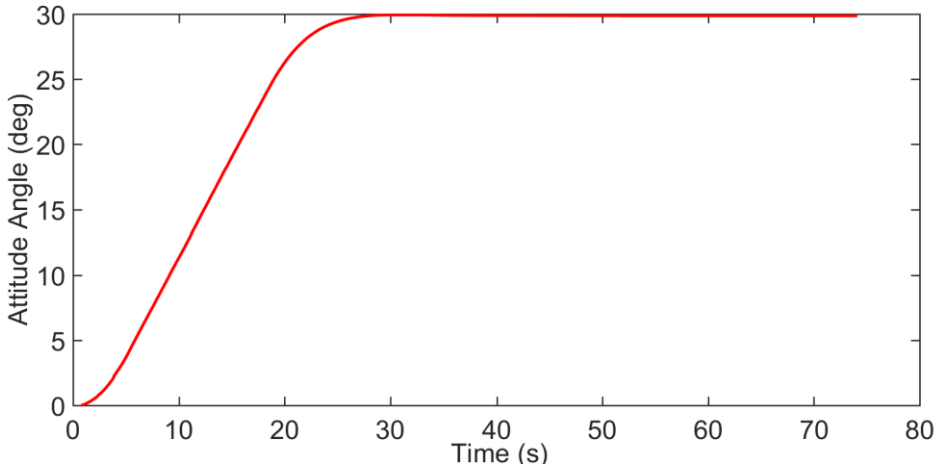

Figure 7.8 Large-angle case: attitude angle

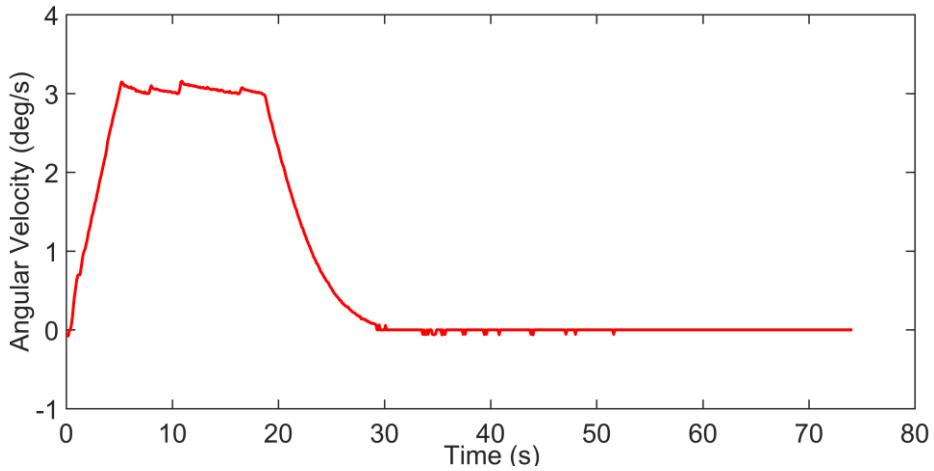

Figure 7.9 Large-angle case: measured angular velocity

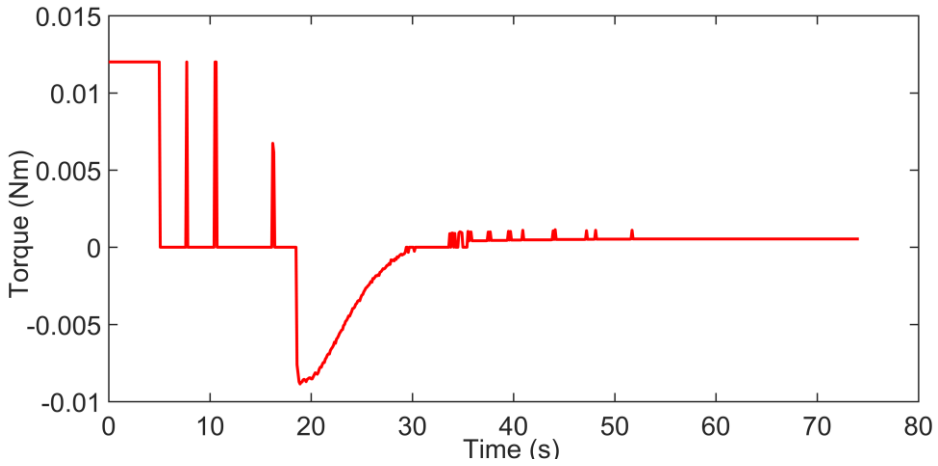

Figure 7.10 Large-angle case: control command from NMPC controller

7.3.3 Large-angle Attitude Maneuver with PWPF Thrusters

In this case, the large-angle attitude maneuver of the simulator is studied using the discontinuous thruster propulsion system. As shown in the diagram below, the PWPF modulator that controls the thruster firing frequency and duration is added into the control scheme. As shown in the diagram below, the on-off control pulses are generated by feeding the PWPF modulator with continuous commands from the controller. As a result, a

sequence of on-off signals is generated at each time instant to control the thrusters' firing with constant magnitude, and the simulator is driven to maneuver until the desired angle is finally reached.

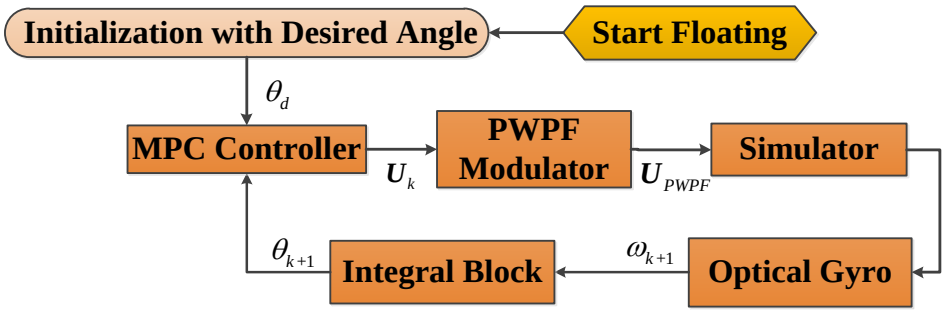

Figure 7.11 Block diagram of PWPF modulated large-angle attitude maneuver

The figure below is a bird view of the simulator, there are eight thrusters in total with two mounted on each side, these thrusters are labelled from 1 to 8 in a counter clockwise order. In particular, thrusters 2 and 6, 4 and 8 are paired up to rotate the simulator clockwise, thrusters 1 and 5, 3 and 7 are paired up to implement the counter clockwise rotation. In this experiment, the force of the thruster's pulse is calibrated to be 0.065 N under a pressure of 0.4 MPa. The length of the level arm between the thrusters mounted at the opposite two sides is 0.42 m. Therefore, when a pair of thrusters are firing, the torque imposing on a simulator is $0.027 Nm$.

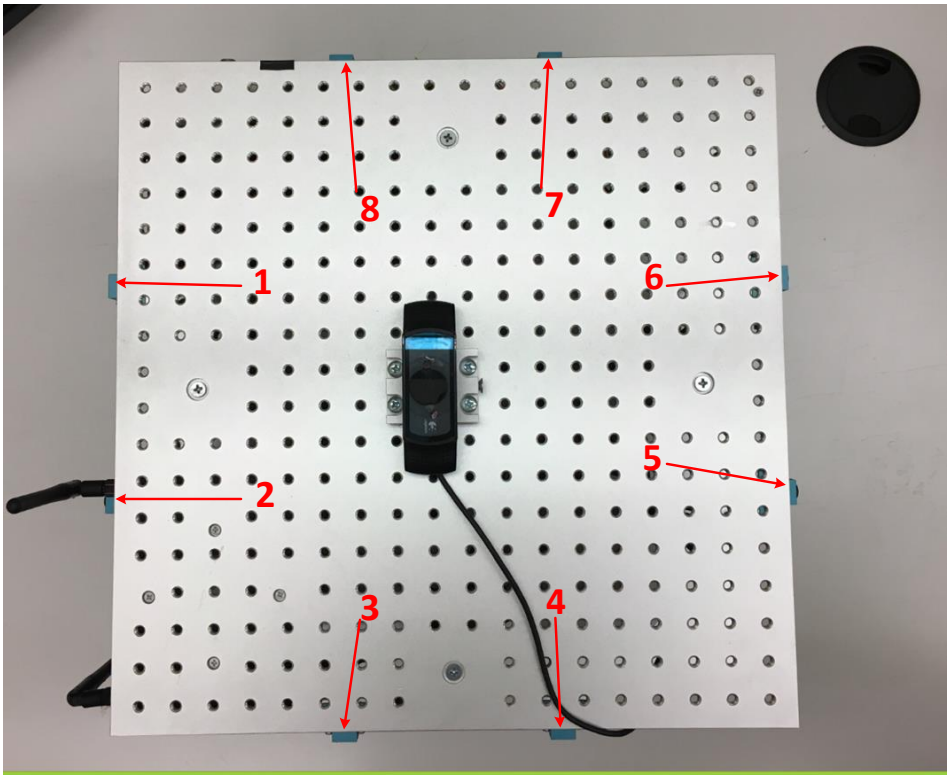

Figure 7.12 PWPF modulated large-angle case: measured angular velocity

Furthermore, it is worth noting that each thruster has a maximum working frequency of 20 *Hz* and this means the thruster is able to switch between on and off up to 20 times per second. In this experiment, the modulation frequency of the PWPF modulator is set to 10 *Hz*. Accordingly, the maximum number that the thruster is modulated to switch is 10 times per second, and the minimum lasting time interval for a firing of the thruster is 0.1 second. Finally, the desired angle for this scenario is set to be 30°.

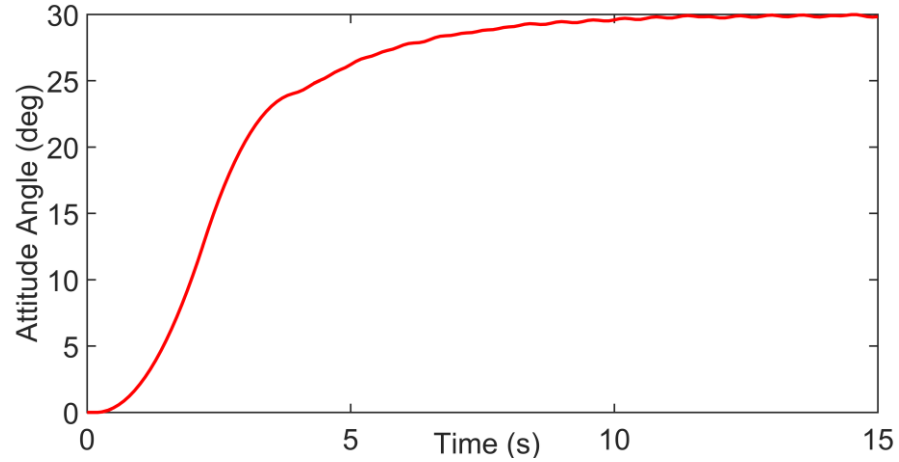

Figure 7.13 PWPF modulated large-angle case: attitude angle

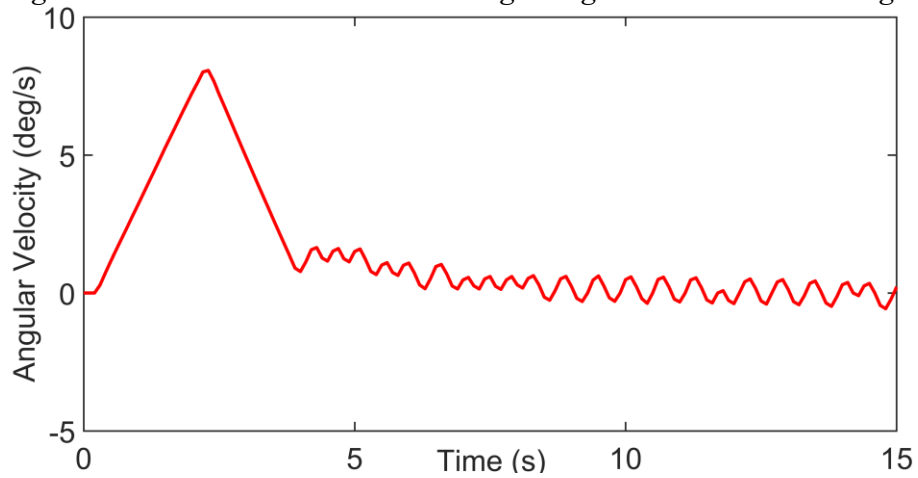

Figure 7.14 PWPF modulated large-angle case: measured angular velocity

Figures 7.13 and 7.14 show the time histories of attitude angle and angular velocity of the simulator, and Figs. 7.15 and 7.16 show the time histories of control torque command from the NMPC controller and the generated pulses from the thrusters, respectively. As seen, the attitude angle reaches the desired value at around 15 *s*, the curve is smooth and there is no overshoot during this maneuvering process. In the meantime, the control command from the NMPC controller gradually decays to below 0.02 *Nm* by the end of the attitude maneuvering process.

In particular, the thrusters are turned on as a pair at the very beginning to rotate the simulator at the maximum acceleration. Seen from the attitude angle and angular velocity curves, the firing of thrusters drives the simulator to reach the desired angle at an increasing speed. As a result, the angular velocity soars up quickly from 0 *m/s* to around 8 *m/s* in the first 3 seconds.

When the angular velocity increases to around 8°*/s*, the control torque commands produced by the NMPC attitude controller fall to negative so as to brake the simulator and slow down its rotation. The negative control torque commands are fed into the PWPF modulator and the previously firing thrusters are shut off. Instead, the thrusters that drive the simulator to rotate counter clockwise are turned on to eject the high-pressure air to produce the negative torque. Then, the negative torque gradually decays as time goes on until the attitude angle gets closer to the desired value.

Before the attitude angle reaches around 25°, the attitude angle curve is smooth and has almost no glitches. This is because the control effects from the thrusters is much larger than the effects from the environmental disturbance. Thus, the attitude maneuvering is mainly dominated by the firings of thrusters during this period. In contrast, the glitches on the attitude angle curve and the angular velocity curve after 8 *s* till the end indicate the effects of the environmental disturbance on the simulator.

In this section, the large-angle attitude maneuver of the simulator is

implemented using the PWPF modulator. The PWPF modulator that controls the thruster firing frequency and duration is added into the control scheme. During this attitude maneuvering, the thrusters are switching frequently between on and off states to drive the simulator's attitude get close but not to exceed the desired angle. In the meantime, the thrusters need to be continuously working to offset the negative disturbance from the environment and the limitations of the testbed. The experimental results demonstrate the effectiveness of the PWPF modulator and the NMPC attitude controller.

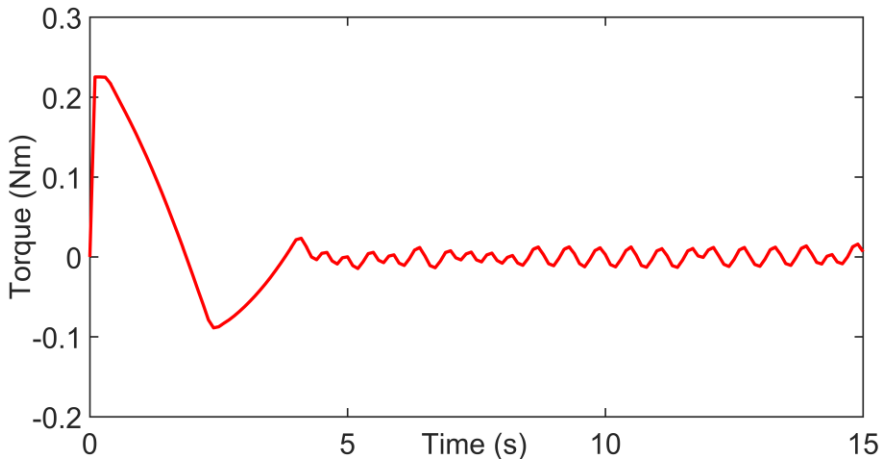

Figure 7.15 PWPF modulated large-angle case: control command from NMPC controller

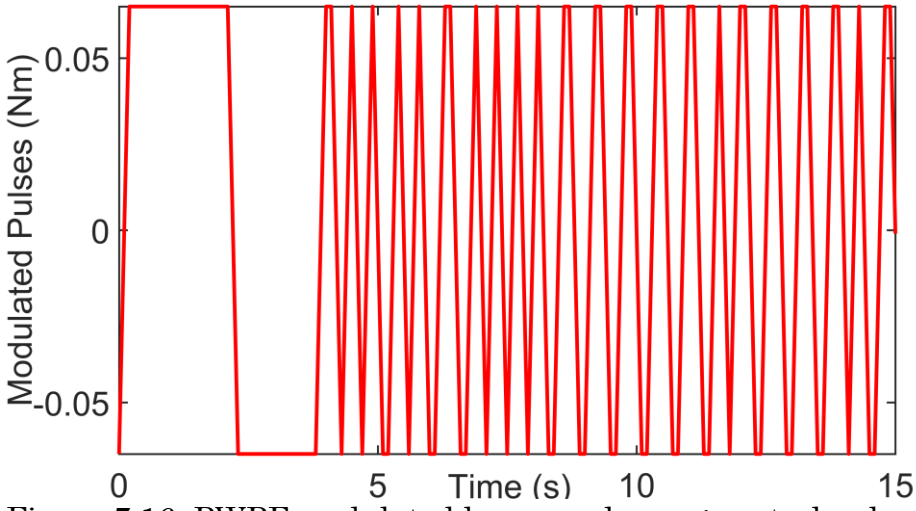

Figure 7.16 PWPF modulated large-angle case: control pulses

Chapter 8 CONCLUSIONS AND FUTURE WORK

Summary: This chapter summarizes the contributions and future research directions for the continuation of the current work.

8.1 Contributions

This work in this dissertation is focused on the development of control schemes for autonomous rendezvous and proximity operations of non-cooperative tumbling target. The contributions are summarized as follows.

8.1.1 Line-of-Sight based Rendezvous with Tumbling Target

Space debris may not necessarily be an attitude stable target. In a more general case, the target is spinning around its axisymmetric axis in space. This poses a safety concern for the chaser spacecraft to approach and thus the tumbling motion is supposed to be modeled. The rendezvous model with a tumbling target is developed based on the linearized TH equations by mathematically introducing the tumbling plane where the spinning axis is rotating. The spinning angular velocity of the target spacecraft is assumed unknown but measurable to the sensors mounted on the chaser spacecraft. The

tumbling plane is assumed perpendicular to the spinning axis that is constantly rotating within this plane. To the best of our knowledge, this tumbling model is proposed for the first time.

In addition, the spacecraft autonomous rendezvous with a passive non-cooperative target with the LOS dynamic model is studied. The constrained optimal control problem is formulated in terms of LOS azimuth angles with respect to the target. The data acquired by the navigation system needs to be converted from the LOS frame to the LVLH frame, and this extra transformation between the LVLH and LOS frames complicates the guidance control and adds extra computational complexity for the onboard CPU. To reduce the computational requirement for the limit onboard computational power, LOS based autonomous rendezvous were developed to directly employ the navigation information. To the best of our knowledge, no attempt has been made to combine the LOS model with the NMPC in ARPO. The numerical results show that the newly proposed line-of-sight NMPC is able to effectively generate optimized approach trajectories with satisfactory control accuracy and the proposed method is insensitive to the measurement uncertainties.

8.1.2 PWPF based Schemes of Autonomous Rendezvous

Due to the differing scenarios in autonomous rendezvous, the NMPC is applied to various dynamic models together with different techniques to construct different control schemes. In particular, the NMPC is applied to TH

model, LOS model and the newly developed rendezvous model with a tumbling target and the rigid-body attitude model, respectively. The PWPF modulator is integrated into the NMPC to generate the on/off control forces from its continuous form. To maneuver the compound spacecraft's attitude and identify the unknown inertial parameters at the same time, the control scheme is constructed by integrating the NMPC and RLS approach in the post-capturing phase. The detailed numerical simulations indicate the effectiveness of these control schemes.

8.1.3 Air Bearing Experimental Validation

A 3 DoF spacecraft air bearing testbed system is designed and built to conduct the real experiments on the high-accuracy granite table. The hardware is assembled and integrated to make the testbed system upgradable for future use. The software system is programmed based on the LabVIEW environment with a user friendly interface to operate various sensors on the simulator platform. The motion control system is integrated into the whole system to control the reaction wheel and thrusters under the NMPC controller. The experiment of applying the proposed control approach to the attitude maneuvering of the floating simulator is conducted. The executable efficiency of the control system under an experimental setting is examined. In the meantime, a set of simulations are implemented to evaluate the control performance in the presence of environmental disturbances.

8.2 Conclusions

The operational restrictions in practical space missions inevitably lead to an optimal control problem subject to a variety of constraints. The NMPC generates the feedback control commands online by solving a constrained QP problem at each sampling instant. The receding horizon process is repeated by shifting the time one-step forward each time. These characteristics make NMPC an attractive candidate for controller design in the ARPO. The challenge of applying the proposed algorithm lies in the parameter selections of control horizon and predictive horizon. So far, there is not a generic formula or equation to compute the exact values of horizon parameters, thus the selection of the horizon parameters is currently experience-based and achieved by trial and error through numerical simulations. Additionally, the constrained optimization problem is solved by dividing the entire time horizon into subintervals, this may lead to a suboptimal solution instead of the optimal solution which is obtained by solving the constrained optimization problem as a whole.

The scheme of integrating the PWPF into the NMPC to minimize the control error and control roughness for a safe approaching trajectory is proposed. The results show that this scheme is able to achieve control objective, less fuel consumption and acceptable control time and accuracy. After that, the

LOS based NMPC is proposed for coplanar autonomous rendezvous in an elliptical orbit with non-cooperative targets. The effectiveness is demonstrated through two different scenarios: rendezvous with a stable target and a spinning target, respectively. Furthermore, the RLS based NMPC scheme is proposed to identify the inertial parameters of a combined spacecraft in the post-capture attitude maneuver phase. The estimated values can converge to the true values within reasonable time. Finally, the executable efficiency of the NMPC is validated through a set of experiments using the air-bearing simulator on the ground testbed. The algorithm is proved to be effective and robust in the presence of environmental disturbances.

8.3 Future Work

The following research is summarized as follows to continue and expand the current work.

(i) Both thrusters and reaction wheels can be used to generate the control torque, thus the development of an allocation scheme to distribute the required torque to the thrusters and reaction wheel is worth further studying.

(ii) The gyro is used now to measure the angular velocity to determine the attitude of the simulator. The following attitude determination technique can focus on using the web camera on top of the simulator and

the fixed LED lights pattern on the ceiling. This involves the applications of computer vision and image processing algorithms.

(iii) Vision-based image processing techniques to recognize the target and multiple obstacles, autonomous trajectory planning algorithms to bypass the obstacles and ensure a safe approach.

(iv) Connect a pair of simulators with tether, the testbed can be used to validate the techniques in tethered system, i.e., stabilize the attitude of a rotating simulator using the tether connected on the other one.

Bibliography

[1] D. Rising, "Satellite hits Atlantic—but what about next one?," *Seattle Times*, November 11, 2013.

[2] "Union of concerned scientists, satellite database," Accessed on May 01, 2016; http://ucsusa.org/satellites.

[3] B. Sullivan, "DARPA phoenix payload orbital delivery system (PODs): 'FedEx to GEO' ", 2013.

[4] E. Gill, O. Montenbruck, and S. Amico, "Autonomous formation flying for the prisma mission," *Journal of Spacecraft and Rockets*, vol. 44, no. 3, pp. 671-681, 2007.

[5] M. H. Shan, J. Guo, and E. Gill, "Review and comparison of active space debris capturing and removal methods," *Progress in Aerospace Sciences,* vol. 80, pp. 18-32, Jan, 2016.

[6] A. Aaron, and G. David, "Dynamic modeling and control of an active debris removal small satellite," *AIAA Guidance, Navigation, and Control Conference and Colocated Conferences*, 2013.

[7] K. Wormnes, R. Letty, L. Summerer, R. Schonenborg, O. Dubois and J. Delaval, "ESA technologies for space debris remediation," pp. 3-4, 2013.

[8] J. L. Goodman, "History of space shuttle rendezvous and proximity operations," *Journal of Spacecraft and Rockets*, vol. 43, no. 5, pp. 944-959, 2006.

[9] J. C. Liou, "Active debris removal – a grand engineering challenge for the twenty-first century," *Advances in the Astronautical Sciences*, vol. 140, pp. 2185-2190, 2011.

[10] S. Lemmens, "Conceptual design of an active debris removal strategy for sunsynchrounous low earth orbit," *International Astronautical Congress*, 2010.

[11] S. Abiko, and G. Hirzinger, "On-line parameter adaptation for a momentum control in the post-grasping of a tumbling target with model uncertainty," *Proceedings of the IEEE/RSJ International Conference on Intelligent Robots and Systems*, 2007.

[12] J. Liang, and O. Ma, "Angular velocity tracking for satellite rendezvous and docking," *Acta Astronautica*, vol. 69, no. 11, pp. 1019-1028, 2011.

[13] T. Davis, and D. Melanson, "XSS-10 micro-satellite flight demonstration program," *Proceedings of the 17th Annual AIAA/USU Conference on Small Satellites*, Logan, UT, pp. 99–99, Aug. 2003.

[14] R. B. Friend, "Orbital express program summary and mission overview," Proceedings of SPIE: *International Society for Optical Engineering*, vol.

6958, pp. 695803, 2008.

[15] A. B. Bosse, W. J. Barnds, M. A. Brown, and N. G. Feerst, "SUMO: spacecraft for the universal modification of orbits," *Proceedings of SPIE*: *International Society for Optical Engineering*, vol. 5419, pp. 36-46, April 2004.

[16] F. A. Angel, W. Zheng, and M. Ou, "Optimal control of space robots for capturing a tumbling object with uncertainties," *Journal of Guidance Control and Dynamics*, vol. 37, no. 6, pp. 2014-2017, 2014.

[17] H. W. Wen, X. K. Yue, and J. P. Yuan, "Dynamic-scaling-based non-certainty-equivalent adaptive spacecraft attitude tracking control," *Journal of Aerospace Engineering*, vol. 31, no. 2, pp. 04017098, 2017.

[18] A. M. Miele, W. Weeks, and M. Circia, "Optimal trajectories for spacecraft rendezvous," *Journal of Optimization Theory and Application*, vol. 132, no. 3, pp. 353-376, 2007.

[19] K. Subbarao, and S. J. Welsh, "Nonlinear control of motion synchronization for satellite proximity operations," *Journal of Guidance Control and Dynamics,* vol. 31, no. 5, pp. 1284-1294, 2008.

[20] C. A. Lembeck, and J. E. Prussing, "Optimal impulsive intercept with low-thrust rendezvous return," *Journal of Guidance Control and Dynamics*, vol. 16, no. 3, pp. 426-433, 1993.

[21] J. C. Liou, N. L. Johnson, and N. M. Hill, "Suboptimal power-limited rendezvous with fixed docking direction and collision avoidance," *Journal of Guidance Control and Dynamics*, vol. 36, no. 1, pp. 648-653, 2010.

[22] H. Bang, and C. S. Oh, "Predictive control for the attitude maneuver of a flexible spacecraft," *Aerospace Science and Technology*, vol. 8, no. 5, pp. 443-452, 2004.

[23] P. Lu, "Optimal predictive control of continuous nonlinear systems," *International Journal of Control*, vol. 62, no. 3, pp. 633-649, 1995.

[24] H. Wen, Z. H. Zhu, D. Jin, and H. Hu, "Model predictive control with output feedback for a deorbiting electrodynamic tether system," *Journal of Guidance Control and Dynamics*, vol. 39, no. 10, pp. 2455-2460, 2016.

[25] Ø. Hegrenæs, J. T. Gravdahl, and P. Tøndel, "Spacecraft attitude control using explicit model predictive control," *Automatica*, vol. 41, no. 12, pp. 2107-2114, 2005.

[26] J. L. Schwartz, M. A. Peck, and C. D. Hall, "Historical review of air-bearing spacecraft simulators," *Journal of Guidance Control and Dynamics*, vol. 26, no. 4, pp. 513-522, 2003.

[27] M. Ciarcià, R. Cristi, and M. M. Romano, , "Emulating scaled clohessy–wiltshire dynamics on an air-bearing spacecraft simulation

testbed," *Journal of Guidance Control and Dynamics*, vol. 40, no. 10, pp. 1-15, 2017.

[28] J. C. Liou, and N. L. Johnson, "A sensitivity study of the effectiveness of active debris removal in leo," *Acta Astronautica*, vol. 64, pp. 236-243, 2009.

[29] S. H. Yu, "Autonomous rendezvous in elliptical orbits," *Acta Astronautica*, vol. 41, no. 2, pp. 95-101, 1997.

[30] S. H. Yu, "Range-rate control algorithms and space rendezvous schemes," *Journal of Guidance Control and Dynamics*, vol. 20, no. 1, pp. 206-208, 1997.

[31] G. Gaias, and S. D'Amico, "Impulsive maneuvers for formation reconfiguration using relative orbital elements," *Journal of Guidance Control and Dynamics*, vol. 38, no. 6, pp. 1036-1049, 2015.

[32] T. E. Carter, "New form for the optimal rendezvous equations near a keplerian orbit," *Journal of Guidance Control and Dynamics*, vol. 13, no. 1, pp. 183-186, 1990.

[33] T. E. Carter, "State transition matrices for terminal rendezvous studies," *Journal of Guidance Control and Dynamics*, vol. 21, no. 1, pp. 148-155, 1998.

[34] W. H. Clohessy, and R. S. Wiltshire, "Terminal guidance system for

satellite rendezvous," *Journal of Aerospace Science*, vol. 27, no. 9, pp.653-658, 1960.

[35] J. Van der Ha, and R. Mugellesi, "Analytical models for relative motion under constant thrust," *Journal of Guidance Control and Dynamics*, vol. 13, no. 4, pp. 644-650, 2002.

[36] S. S. Vaddi, S. R. Vadali, and K. T. Alfriend, "Formation flying: accommodating nonlinearity and eccentricity perturbations," *Journal of Guidance Control and Dynamics*, vol. 26, no. 2, pp. 214-223, 2003.

[37] G. Inalhan, M. Tillerson, and J. P. How, "Relative dynamics and control of spacecraft formations in eccentric orbits," *Journal of Guidance Control and Dynamics*, vol. 25, no. 1, pp. 48-59, 2002.

[38] P. Li, and Z. H. Zhu, "State dependent model predictive control for orbital rendezvous using pulse width pulse frequency modulated thrusters," *Advanecs in Space Research*, vol. 58, pp. 64-73, 2015.

[39] P. Li, and Z. H. Zhu, "Line-of-sight nonlinear model predictive control for autonomous rendezvous in elliptical orbit," *Aerospace Science and Technology*, vol. 69, pp. 236-243, 2017.

[40] P. Li, and Z. H. Zhu, "Model predictive control for spacecraft rendezvous in elliptical orbit," *Acta Astronautica*, vol. 146, np. 7, pp. 339-348, 2018.

[41] J. J. Luo, B. C. Gong, and J. P. Yuan, "Angles-only relative navigation

and closed-loop guidance for spacecraft proximity operations, " *Acta Astronautica*, vol. 128, pp. 91-106, 2016.

[42] D. Y. Zhang, J. J. Luo, D. W. Gao, and J. P. Yuan, "A novel nonlinear control for tracking and rendezvous with a rotating non-cooperative target with translational maneuver," *Acta Astronautica*, vol. 138, pp. 276-289, 2017.

[43] C. A. Lembeck, and J. E. Prussing, "Optimal impulsive intercept with low-thrust rendezvous return," *Journal of Guidance Control and Dynamics*, vol. 16, no. 3, pp. 426–433, 1993.

[44] M. Guelman, and M. Aleshin, "Optimal bounded low-thrust rendezvous with fixed terminal-approach direction," *Journal of Guidance Control and Dynamics*, vol. 24, no. 2, pp. 378–385, 2001.

[45] L. Breger, and J. P. How, "Gauss's variational equation-based dynamics and control for formation flying spacecraft," *Journal of Guidance Control and Dynamics*, vol. 30, no. 2, pp. 437-448, 2007.

[46] L. Breger, and J. P. How, "Safe trajectories for autonomous rendezvous of spacecraft, " *Journal of Guidance Control and Dynamics*, vol. 31, no. 5, pp. 1478-1489, 2008.

[47] S. Matsumoto, "Approach planning and guidance for uncontrolled rotating satellite capture considering collision avoidance," *Proceeding of*

the 7th International Symposium on Artificial Intelligence, Robotics and Automation in Space, 2003.

[48] A. Richards, T. Schouwenaars, J. P. How, and E. Feron, "Spacecraft trajectory planning with avoidance constraints using mixed-integer linear programming," *Journal of Guidance Control and Dynamics*, vol. 25, no. 4, pp. 755-764, 2002.

[49] R. Epenoy, "Fuel optimization for continuous thrust orbital rendezvous with collision avoidance constraint," *Journal of Guidance Control and Dynamics*, vol. 34, no. 2, pp. 493-503, 2011.

[50] P. Lu, and X. Liu, "Autonomous trajectory planning for rendezvous and proximity operations by conic optimization," *Journal of Guidance Control and Dynamics*, vol. 36, no. 2, pp. 375-389, 2013.

[51] Z. Ma, O. Ma, and N. Shashikanth, "Optimal approach to and alignment with a rotating rigid body for capture," *Journal of the Astronautical Sciences*, vol. 55, no. 4, pp. 407-409, 2007.

[52] M. Xin, and H. Pan, "Nonlinear optimal control of spacecraft approaching a tumbling target," *Aerospace Science and Technology*, vol. 15, no. 2, pp. 79-89, 2011.

[53] G. Boyarko, O. Yakimenko, and M. Romano, "Optimal rendezvous trajectories of a controlled spacecraft and a tumbling object," *Journal of*

Guidance Control and Dynamics, vol. 34, no. 4, pp. 1239-1252, 2011.

[54] J. B. Rawlings, and D. Q. Mayne, Model predictive control: theory and design, Nob Hill Publishing, Madison, Wisconsin, 2015.

[55] J. Cloutier, C. D'Souza, and C. Mracek, "Nonlinear regulation and nonlinear h-infite control via the state-dependent riccati equatoin technique," *Proc. 1st International Conference on Nonlinear Problems in Aviatoin and Aerospace,* vol. 1, pp. 117-123, 1996.

[56] L. Grune, and J. Pannek, *Nonlinear model predictive control: theory and algorithms*, Springer, 2011.

[57] L. P. Wang, *Model predictive control system design and implementation using matlab*, Springer, 2nd Printing, pp. 7-12, Chap. 1, 2009.

[58] A. Weiss, M. Baldwin, S. R. Erwin, and I. Kolmanovsky, "Model predictive control for spacecraft rendezvous and docking: strategies for handling constraints and case studies," *IEEE Transactions on Control Systems Technology*, vol. 23, no. 4, pp. 1638-1647, 2015.

[59] S. Payman, and O. Andrezej, "Nonlinear model predictive control approach in design of adaptive cruise control with automated switching to cruise control," *Control Engineering Practice*, vol. 26, pp. 160-177, 2014.

[60] Q. Li, J. P. Yuan, and C. Gao, "Model predictive control for autonomous

rendezvous and docking with a tumbling target," *Aerospace Science and Technology*, vol. 69, pp. 700-711, 2017.

[61] H. Wen, Z. H. Zhu, D. Jing, and H. Hu, "Tension control of space tether via online quasi-linearization iterations," *Advances in Space Research*, vol. 57, no. 3, pp. 754-763, 2016.

[62] H. Li, W. Yan, and Y. Shi, "Continuous-time model predictive control of under-actuated spacecraft with bounded control torques," *Automatica*, vol. 75, pp.144-153, 2017.

[63] C. D. Petersen, F. Leve, and I. Kolmanovsky, "Model predictive control of an underactuated spacecraft with two reaction wheels," *Journal of Guidance Control and Dynamics*, vol. 40, no. 2, pp. 320-332, 2016.

[64] U. Lee, and M. Mesbahi, "Constrained autonomous precision landing via dual quaternions and model predictive control," *Journal of Guidance Control and Dynamics*, vol. 40, no. 2, pp. 292-308, 2016.

[65] J. A. Starek, and I. Kolmanovsky, "Nonlinear model predictive control strategy for low thrust spacecraft missions," *Optimal Control Applications and Methods*, vol. *35*, no. 1, pp. 1-20, 2014.

[66] F. Gavilan, R. Vazquez, and E. F. Camacho, "Chance-constrained model predictive control for spacecraft rendezvous with disturbance estimation," *Control Engineering Practice*, vol. 20, no. 2, pp. 111-122,

2012.

[67] M. Leomanni, E. Rogers, and S. B. Gabriel, "Explicit model predictive control approach for low-thrust spacecraft proximity operations," *Journal of Guidance Control and Dynamics*, vol. 37, no. 6, pp. 1780-1790, 2014.

[68] E. N. Hartley, P. A. Trodden, A. G. Richards, and J. M. Maciejowski, "Model predictive control system design and implementation for spacecraft rendezvous," *Control Engineering Practice*, vol. 20, no. 7, pp. 695-713, 2012.

[69] E. N. Hartley, M. Gallieri, and J. M. Maciejowski, "Terminal spacecraft rendezvous and capture with LASSO model predictive control," *International Journal of Control*, vol. 86, no. 11, pp. 2104-2113, 2013.

[70] E. N. Hartley, and J. M. Maciejowski, "Field programmable gate array based predictive control system for spacecraft rendezvous in elliptical orbits," *Optimal Control Applications and Methods*, vol. 36, no. 5, pp. 585-607, 2015.

[71] Y. Lian, and G. Tang, "Libration point orbit rendezvous using pwpf modulated terminal sliding mode control," *Advances in Space Research*, vol. 52, no. 12, pp. 2156-2167, 2013.

[72] G. Song, Buck, N. V., and B. N. Agrawal, "Spacecraft vibration reduction using pulse width pulse frequency modulated input shaper," *Journal of Guidance Control and Dynamics*, vol. 22, no. 3, pp. 433-440, 1999.

[73] Q. Hu, "Robust integral variable strucure controller and pulse width pulse frequency modulated input shaper design for flexible spacecraft with mismatched unvertainty/disturbance," *ISA Transactions*, vol. 28, no. 2, pp. 505-518, 2007.

[74] Q. Hu, and Ma., G, "Vibration suppression of flexible spacecraft during attitude maneuvers," *Journal of Guidance Control and Dynamics*, vol. 28, no. 2, pp. 377-380, 2005.

[75] G. Song, and B. N. Agrawal, "Vibration suppression of flexible spacecraft during attitude control," *Acta Astronautica*, vol. 49, no. 2, pp. 71-83, 2001.

[76] H. C. Gui, L. Jin, and S. J. Xu, "Small-time local controllability of spacecraft attitude using control moment gyros," *Automatica*, vol. 53, pp. 141-148, 2015.

[77] Y. Murotsu, K. Senda, M. Ozaki, and S. Tsujio, "Parameter identification of unknown object handled by free-flying space robot," *Journal of Guidance Control and Dynamics*, vol. 17, no. 3, pp. 488-494, 1994.

[78] F. Aghili, "Time-optimal detumbling control of spacecraft," *Journal of Guidance Control and Dynamics*, vol. 32, no. 5, pp. 1671-1675, 2009.

[79] X. F. Liu, H. Q. Li, , Y. J. Chen, and X. Wang, "Dynamics and control of capture of a floating rigid body by a spacecraft robotic arm," *Multibody System Dynamics*, vol. 33, no. 3, pp. 315-332, 2015.

[80] N. Chau., and I. Sharf, "Adaptive reactionless motion and parameter identification in postcapture of space debris," *Journal of Guidance Control and Dynamics*, vol. 36, no. 2, pp. 404-414, 2013.

[81] P. F. Huang, M. Wang, and F. Zhang, "Reconfigurable spacecraft attitude takeover control in post-capture of target by space manipulators," *Journal of the Franklin Institute*, vol. 353, no. 9, pp. 1985-2008, 2016.

[82] P. F. Huang., M. Wang, and F. Zhang, "Attitude takeover control for post-capture of target spacecraft using space robot," *Aerospace Science and Technology*, vol. 51, pp. 171-180, 2016.

[83] Q. Hu, Y. Jia, and S. Xu, "Recursive dynamics algorithm for multibody systems with variable-speed control moment gyroscopes," *Journal of Guidance Control and Dynamics*, vol. 36, no. 5, pp. 1388-1398, 2013.

[84] Z. Xu, N. Qi, and Y. Chen, "Parameter estimation of a three-axis spacecraft simulator using recursive least-squares approach with

tracking differentiator and extended kalman filter," *Acta Astronautica*, vol. 117, pp. 254-262, 2015.

[85] T. Zhang, X. K. Yue, and J. P. Yuan, "Stabilization and parameter identification of tumbling spacecraft debris with bounded torque in postcapture," *Acta Astronautica*, vol. 123, pp. 301-309, 2016.

[86] Z. Ni, R. Mu, G. Xun, and Z. Wu, "Time-varying modal parameters identification of a spacecraft with rotating flexible appendage by recursive algorithm," *Acta Astronautica*, vol. 118, pp. 49-61, 2016.

[87] O. Ma, H. Dang, and K. Pham, "On-orbit identification of inertia properties of spacecraft using a robotic arm," *Journal of Guidance Control and Dynamics*, vol. 31, no. 6, pp. 1761-1771, 2008.

[88] M. Wang, J. J. Luo, and U. Walter, "Novel synthesis method for minimizing attitude disturbance of the free-floating space robots," *Journal of Guidance Control and Dynamics*, vol. 38, no. 11, pp. 695-704, 2016.

[89] G. T. Haupt, "Optimal recursive iterative algorithm for discrete nonlinear least-squares estimation," *Jounrnal of Guidance Control and Dynamics*, vol. 19, no. 3, pp. 643-649, 1996.

[90] F. Zhang, and P. F. Huang, "On-line estimation of inertia parameters of space debris for its tether-assisted removal," *Acta Astronautica*, vol. 107,

pp.150-162, 2015.

[91] R. Zappulla, J. Zagaris, C. Park, and M. Romano, "Dynamic air-bearing hardware-in-the-loop testbed to experimentally evaluate autonomous spacecraft proximity maneuvers," *Journal of Spacecraft and Rockets*, pp. 1-15, 2017.

[92] W. R. Wilson, L. L. Jones, and M. A. Peck, "A multimodule planar air bearing testbed for cubesat-scale spacecraft," *Journal of Dynamic Systems Measurement and Control*, vol. 135, no. 4, pp. 045001, 2013.

[93] J. J. Kim, and B. N. Agrawal, "Automatic mass balancing of air-bearing-based three-axis rotational spacecraft simulator," *Journal of Guidance Control and Dynamics*, vol. *32*, no. 3, pp.1005-1017, 2009.

[94] R. Bevilacqua, J. Hall, J. Horning, and M. Romano, "Ad-hoc wireless networking and shared computation based upon linux for autonomous multi-robot systems," *Journal of Aerospace Computing Information and Communication*, vol. 6, no. 5, pp. 328-353, 2009.

[95] M. Ciarcià, A. Grompone, and M. Romano, "A near-optimal guidance for cooperative docking maneuvers," *Acta Astronautica*, vol. 102, pp. 367-377, 2014.

[96] D. P. Scharf, J. A. Keim, and F. Y. Hadaegh, "Flight-like ground demonstrations of precision maneuvers for spacecraft formations-Part

I," *IEEE Systems Journal*, vol. 4, no. 1, pp. 84-95, 2010.

[97] C. C. Bettanini, A. Aboudan, A. Francesconi, and F. Angrilli, "Improving the free-floater space robot simulator for intervention missions," Proceedings of the 7th International Symposium on Artificial Intelligence, Robotics and Automation in Space, Nara, Japan, 2003.

[98] T. Liu, and J. Zhao, *Spacecraft dynamics*, Harbin Institute of Technology Press, Harbin, China. pp. 86-87, 2003. (in Chinese)

[99] P. C. Hughes, *Spacecraft attitude dynamics*, Chapter 3, Courier Corporation, pp. 70-83, 2012.

[100] D. Q. Mayne, J. B. Rawlings, C. V. Rao, and P. O. Scokaert, "Constrained model predictive control: stability and optimality," *Automatica*, vol. 36, 2000, pp. 798-814.

[101] A. Richards, and J. P. How, "Model predictive control of vehicle maneuvers with guaranteed completion time and robust feasibility," *Proceedings of the 2003 American Control Conference*, IEEE, Denver, CO, pp. 4034-4040, 2003.

[102] J. B. Rawlings, and K. R. Muske, "The stability of constrained receding horizon control," *IEEE Transactions on Automatic Control*, vol. 3, pp. 2837-2841, 1994.

[103] D. Mayne, J. Rawlings, C. Rao, and P. Scokaert, "Constrained model

predictive control: stability and optimality," *Automatica*, vol. 36, no. 6, pp. 789-814, 2000.